

Near-field Spectral Imaging of Crystal-phase Heterostructures in GaAs Nanowires

Dissertation

zur Erlangung des Doktorgrades der Naturwissenschaften
(Dr. rer. nat.)

der

Naturwissenschaftlichen Fakultät II
Chemie, Physik und Mathematik

der Martin-Luther-Universität
Halle-Wittenberg

vorgelegt von

Herrn Alexander Senichev
geb. am 04 Januar 1986 in Kirowsk, Russland

verteidigt am 21.10.2016

Gutachter:

1. Jun.-Prof. Dr. Jörg Schilling, Martin-Luther-Universität Halle-Wittenberg
2. Prof. Dr. Ralf B. Wehrspohn, Martin-Luther-Universität Halle-Wittenberg
3. Dr. Heike E. Riel, IBM Fellow, IBM Research Zürich

Abstract

The thesis work is primarily focused on imaging and understanding of optoelectronic properties of semiconductor materials at the nanometer length scale as a function of their local morphology, crystal structure and elemental composition. The main objects of the study are self-catalysed GaAs–AlGaAs core-shell nanowires fabricated by a bottom-up vapour-liquid-solid growth technique using molecular beam epitaxy. The practical interest to nanowires stems from their one-dimensional nature paving the way for the fabrication of advanced optical and electronic devices based thereon. A special focus is given to properties originating from the occurrence of the wurtzite crystal phase in GaAs nanowires, which is not existent in bulk and thin film GaAs crystals. The understanding of the energy band structure of wurtzite GaAs as well as the coexistence of zinc blende and wurtzite crystal phases in such wires has both high fundamental and practical importance. In this thesis, local optoelectronic properties of GaAs nanowires with a mixture of zinc blende and wurtzite crystal phases are studied by means of near-field scanning optical microscopy. To this end, a home-build near-field scanning optical microscope operating at cryogenic temperatures is installed and applied. The microscope allows to image the local charge carrier recombination in GaAs nanowires with a spatial resolution at the nanometer length scale.

The electronic properties of crystal-phase heterostructures formed by the alternation of zinc blende and wurtzite segments along GaAs nanowires are studied by correlated near-field spectral imaging and structural analysis performed on the same individual wires. The collected spectroscopic information reflects the pronounced variation of local optoelectronic properties of these wires as a function of a mixture of zinc blende and wurtzite crystal phases. The results of this study allow to resolve and assign observed emission peaks to individual zinc blende and wurtzite disks, which structural parameters are known with a lattice-resolved accuracy. The obtained quantitative information is essential to derive such material parameters as the band gap energy and the effective electron mass of wurtzite GaAs. In addition to the effects of crystal structure inhomogeneity, the influence of beryllium dopants incorporation on optoelectronic properties of heavily beryllium doped GaAs nanowires is investigated. The particular interest is put on the studying of a twinning superlattice observed in such *p*-doped GaAs nanowires.

The experimental approach of this study allows to address issues related to the localisation of carriers on crystal structure defects, electronic properties of individual crystal-phase heterostructures and effects of dopants on optical properties of GaAs nanowires. The results of the thesis provide direct and quantitative insights into correlations between the crystal structure and optics of single GaAs nanowires. The findings present an important step forward to the band gap engineering of nanowires by the controlled crystal phase formation.

Keywords: Nanowires, wurtzite GaAs, crystal-phase heterostructures, doping, near-field scanning optical microscopy, carrier recombination profiling, subwavelength imaging, nanoscale structure-property correlation.

Zusammenfassung

Die vorliegende Doktorarbeit befasst sich mit der Analyse der optoelektronischen Eigenschaften von Halbleiter-Nanostrukturen als Funktion ihrer Morphologie, kristallinen Struktur und ihrer chemischen Zusammensetzung im Nanometer-Bereich. Als Hauptobjekt dieser Studie dienen GaAs–AlGaAs-“core-shell”-Nanodrähte, die mittels Molekularstrahlepitaxie im selbst-katalysierten VLS-Verfahren (der sogen. “vapor-liquid-solid” Methode) hergestellt wurden. Das praktische Interesse an diesen Nanodrähten liegt auf deren eindimensionale Struktur, die eine einzigartige Plattform für die Entwicklung auf dem Gebiet der Optoelektronik bietet. Im Speziellen ist diese Arbeit auf die besonderen Eigenschaften der Nanodrähte konzentriert, die sich auf Grund ihrer speziellen Wachstumsstrukturen ergeben. Als besonderes Phänomen tritt hier z.B. ein segmentierter Wechsel der Wurtzit- und Sphalerit-Kristallgitterstruktur auf. Es ist sowohl von praktischem, als auch von fundamentalem Interesse, die bislang nur kontrovers diskutierte Bandstruktur der Wurtzit-Phase sowie die der Zinkblende-Wurtzit-Heterostrukturen in GaAs zu untersuchen.

In der vorliegenden Studie wurden GaAs-Nanodrähte untersucht, die aus einer Mischung von Wurtzit- und Zinkblende-Struktur-Segmenten bestanden. Zu diesem Zweck wurde ein eigens dafür entwickeltes, bei Tieftemperaturen arbeitendes Rasternahfeldmikroskop eingesetzt, um die lokale Ladungsträger-Rekombination mit einer Auflösung im Nanometer-Bereich 2-dimensional abzubilden. Die ausschlaggebende Innovation hierbei war die Kombination von den Verfahren der korrelierten Nahfeld- und Struktur-Analyse, bei der optische und struktur-mikroskopische Messungen an ein und denselben Nanodrähten vorgenommen wurden, um optische und strukturelle Eigenschaften eindeutig korrelieren zu können. Die optische Auflösung im Nanometer-Bereich und die atomare Analyse der kristallinen Struktur erlaubten es, die beobachteten Fluoreszenz-Piks den geometrischen Parametern einzelner Scheiben mit Wurtzit- oder Zinkblende-Struktur (bzw. deren Abfolge) zuzuordnen. Die quantitative Analyse, die nur im korrelierten Nahfeld-Struktur-Analyse-Verfahren durchgeführt werden können, ist Voraussetzung, um wichtige Eigenschaften der Wurtzit-GaAs-Strukturen zu bestimmen. Dies betrifft z.B. die Ermittlung der Energie der Bandlücke oder der effektiven Elektronenmasse. Zusätzlich zu diesen Struktur-Eigenschaftsbeziehungen wird im Anschluss der Einfluss einer Beryllium-Dotierung auf die optoelektronischen Eigenschaften der GaAs Nanodrähte untersucht. Besondere Aufmerksamkeit wurde hierbei den in p -dotierten Nanodrähten auftretenden Zwillings-Übergittern gewidmet.

Die experimentelle Methode dieser Studie ermöglicht es, Fragen zur Lokalisierung der Ladungsträger an den Defekten der Kristallstruktur, zu elektronischen Eigenschaften einzelner Kristall-Heterostrukturen und zum Einfluss der Dotanden auf die optischen Eigenschaften der GaAs Nanodrähte zu beantworten. Die in dieser Doktorarbeit aufgeführten Ergebnisse liefern einen quantitativen Einblick in die Korrelation zwischen der kristallinen Struktur einzelner GaAs Nanodrähte und deren optischen Eigenschaften und stellen damit einen wichtigen Schritt in Richtung einer gezielten Beeinflussung der optischen Eigenschaften der Nanodrähte mittels kontrollierter Phasen-Bildung während des Wachstums dar.

Schlüsselwörter: Nanodrähte, Wurtzit-GaAs, kristalline Phasen-Heterostruktur, Dotierung, optische Rasternahfeldmikroskopie, Ladungsträger-Rekombination, Sub-Wellenlängen-Abbildung, Struktur-Eigenschaft-Korrelation.

Preface

The work presented in this thesis was performed during the years 2011-2015 at the Max Planck Institute of Microstructure Physics in Halle, Germany, and supported by the International Max Planck Research School for Science and Technology of Nanostructures (Nano-IMPRS). Scientific interests of the Research School focus on the synthesis, the characterisation and the theoretical description of nanoscale materials in order to improve the fundamental understanding of their unique structural and physical properties and fabrication processes. My research is conducted on near-field spectral imaging of semiconductor nanostructures, mainly GaAs nanowires, under the supervision of Dr. Peter Werner at the Experimental Department II. Various experimental facilities of our department, such as advanced high-resolution and analytical electron microscopy and optical spectroscopy systems, were further complemented by the home-build near-field scanning optical microscope (NSOM) installed and applied during the time of my research work.

This doctoral study is my one of the most significant academic experience. The writing of this thesis has been an interesting and at the same time challenging journey for me. I would like to reflect on the following people who have helped me during these years and made this thesis possible. Without their support and guidance this study would not have been completed.

I would like to express my sincere gratitude to my supervisor Dr. Peter Werner for his patience and motivation. He created a nice atmosphere for doing research and always encouraged me to think independently. I would like to thank Dr. Werner for teaching me about transmission electron microscopy and providing an accurate structural characterisation of my samples. His guidance, careful reading and commenting on my manuscript helped me to complete this thesis. I am grateful for all the support I have received from him during these years.

I would like to thank my mentor Jun.-Prof. Dr. Jörg Schilling at the Martin Luther University Halle-Wittenberg for always finding the time to provide his relevant input on my research and manuscripts. I am grateful for fruitful discussions about my research projects that helped me to emphasise the main results of my work. I would also like to thank him for the great experience that I have got as a teaching assistant of his lecture course at the university.

I am deeply grateful to Prof. Dr. Christoph Lienau from the Carl von Ossietzky University of Oldenburg and members of his Ultrafast Nano-Optics group for introducing me into the field of near-field optics. I highly value their support during the installation of the NSOM setup and first measurements. The discussions with Prof. Lienau have always been very interesting and stimulating. His insightful comments and questions helped me to focus this study and enrich my ideas. I would also like to thank Prof. Lienau for his advice on the writing of scientific papers.

I would like to acknowledge Dr. Vadim Talalaev, who invited me to Max Planck Institute

of Microstructure Physics, for his guidance inside our optics laboratory as well as outside it. He taught me about optical spectroscopy techniques and gave me a lot of practical tips. I thank Ms. Kornelia Sklarek and Dr. Wilfried Erfurth for the preparation of substrates for my samples and Mr. Horst Blumtritt for the help with the focused ion beam preparation of nanowires for structural analysis. Ms. Sigrid Hopfe and Ms. Claudia Münx are acknowledged for their kind assistance in the chemical laboratory. I am grateful to Frank Syrowatka from the Interdisciplinary Centre of Materials Science for numerous inspections of my near-field probes.

I have had a pleasure to collaborate during my study with wonderful people from various research groups and countries. They provided samples for my research, shared interesting ideas and gave constructive criticism to improve the quality of our work. I would like to thank them for their contributions to this research. The GaAs-AlGaAs core-shell nanowires were grown in the group of Dr. Lutz Geelhaar at the Paul Drude Institute for Solid State Electronics. The beryllium-doped GaAs-AlGaAs core-shell nanowires were kindly provided by the group of Prof. Dr. George Cirlin working at the St. Petersburg Academic University. The samples with site-selected InAs quantum dots were grown at the Ruhr-Universität Bochum in the department of Dr. Prof. Andreas D. Wieck and provided by Dr. Yu-Ying Hu. In addition, I have had a pleasure to collaborate with Dr. Richard Nötzel, Pavel Aseev, and Paul E. D. S. Rodriguez from the Institute of Optoelectronic Systems and Microtechnology (ISOM) of the Technical University of Madrid. The project involved the investigation of near-infrared emitting In-rich InGaN layers grown directly on silicon and InN surface quantum dots by our custom-made low-temperature near-field scanning optical microscope. The results of our study of these novel and high quality materials have not been included to the thesis, though they have been recently published in peer-reviewed journals.

Many friends have cheered me up, helped me to overcome difficult periods and supported me during these years. I greatly value their friendship. Special thanks to Oleg Brovko who was always willing to help and give his best suggestions. I would like to single out María Santo, a former coordinator of the Nano-IMPRS program, for her continuous encouragement and support during my first year in Halle. And, of course, I am very grateful for the support and help I have received from all my friends and colleagues, although I have not explicitly mentioned you here.

Last but not the least, I would like to thank my family. My parents were always supporting me during this journey and my life in general. I will always be grateful to them for the doors of opportunity that they have opened for me. I especially thank Olga — my closest friend and wife. Thank you for keeping me sane through these years and being a constant source of love and support. This thesis would not have been possible without you.

Publications (Veröffentlichungen)

- i **A. V. Senichev**, V. G. Talalaev, I. V. Shtrom, H. Blumtritt, G. E. Cirlin, J. Schilling, C. Lienau, and P. Werner. *Nanospectroscopic Imaging of Twinning Superlattices in an Individual GaAs–AlGaAs Core-Shell Nanowire*. ACS Photonics, **1**, 1099 (2014). **Included in a cross-journal virtual issue “Probing the Fundamentals of Light-Matter Interactions”**.
- ii **A. V. Senichev**, O. Brandt, P. Corfdir, S. Breuer, J. Schilling, L. Geelhaar, and P. Werner. *Electronic Properties of Crystal-Phase Heterostructures in GaAs Nanowires Studied by Near-Field Spectral Imaging*. In preparation, (2016).

Papers not included in the thesis

- iii P. E. D. S. Rodriguez, P. Aseev, V. J. Gómez, P. Kumar, N. ul H. Alvi, E. Calleja, J. M. Manuel, F. M. Morales, J. J. Jiménez, R. García, **A. Senichev**, C. Lienau, and R. Nötzel. *Stranski–Krastanov InN/InGaN quantum dots grown directly on Si (111)*. Appl. Phys. Lett., **106**, 023105 (2015).
- iv P. Aseev, P. E. D. S. Rodriguez, V. J. Gómez, N. ul H. Alvi, J. M. Manuel, F. M. Morales, J. J. Jiménez, R. García, **A. Senichev**, C. Lienau, E. Calleja and R. Nötzel. *Near-infrared Emitting In-rich InGaN Layers Grown Directly on Si: Towards the Whole Composition Range*. Appl. Phys. Lett., **106**, 072102 (2015).

Conference presentations (selected)

1. **A. V. Senichev** and P. Werner. *Near-Field Spectral Imaging of Crystal-Phase Heterostructures in GaAs Nanowires*. Max Planck Institute of Microstructure Physics Evaluation, Meeting of the scientific Advisory Board, November 24–25 (2015). Oral presentation.
2. **A. V. Senichev**, S. Breuer, H. Blumtritt, L. Geelhaar, and P. Werner. *Local Photoluminescence of GaAs Nanowires Consisting of Wurtzite and Zinc-blende Segments*. 8th Nanowire Growth Workshop and Nanowires 2014, Eindhoven, Netherlands, August 25–29 (2014). Oral presentation.
3. **A. V. Senichev**, I. Shtrom, V. Talalaev, G. Cirlin, C. Lienau, J. Schilling, and P. Werner. *Nanospectroscopic Imaging of Twinning Superlattices in Individual Beryllium-doped GaAs–AlGaAs Core-Shell Nanowires*. German Physical Society Spring Meeting of the Condensed Matter Section, Dresden, Germany, March 30–April 4 (2014). Oral presentation.

4. **A. V. Senichev**, P. Werner, I. V. Shtrom, V. G. Talalaev, G. E. Cirlin, and J. Schilling. *Near-Field Scanning Optical Microscopy and Structural Analysis of Single p-GaAs/AlGaAs Core-Shell Nanowires*. Materials Research Society Fall Meeting, Boston, Massachusetts, USA, December 1–6 (2013). Oral presentation.
5. **A. V. Senichev**, V. G. Talalaev, G. E. Cirlin, J. Schilling, and P. Werner. *Near-field Scanning Optical Microscopy and Structural Analysis of Single p-GaAs/AlGaAs Core-Shell Nanowires*. Joint IMPRS/SFB Workshop on Nanoscience and -technology, Halle/Saale, Germany, September 30–October 2 (2013). Oral presentation.
6. **A. V. Senichev**, V. G. Talalaev, I. V. Shtrom, J. Schilling, G. E. Cirlin, and P. Werner. *Correlated Optical and Structural Analysis of Individual p-GaAs–AlGaAs Core-Shell Nanowires*. Workshop “Light at the Nanotip: Scanning Near-field Optical Microscopy and Spectroscopy”, 538. WE-Heraeus-Seminar, Bad Honnef, Germany, August 4–8 (2013). Poster. **Best Poster Award**.
7. **A. V. Senichev**, V. G. Talalaev, I. V. Shtrom, J. Schilling, G. E. Cirlin, and P. Werner. *Correlated Optical and Structural Analysis of Individual p-GaAs–AlGaAs Core-Shell Nanowires*, European Material Research Society Spring Meeting, Strasbourg, France, May 27–31 (2013). Poster. **Best Poster Award**.
8. **A. V. Senichev**, V. G. Talalaev, J. Schilling, G. E. Cirlin, and P. Werner. *Single Core-Shell GaAs/AlGaAs Nanowires: A Close Look by Near-field Optical Spectroscopy*. German Physical Society Spring Meeting of the Condensed Matter Section, Regensburg, Germany, March 10–15 (2013). Oral presentation.
9. **A. V. Senichev**, V. G. Talalaev, J. Schilling, G. E. Cirlin, and P. Werner. *Study of Excitonic States in Single InAs Quantum Dots by Low-temperature SNOM*. German Physical Society Spring Meeting of the Condensed Matter Section, Regensburg, Germany, March 10–15 (2013). Poster.
10. **A. V. Senichev**. *Near-field Scanning Optical Microscopy of Infrared Emitting Semiconductor Nanostructures*. IBM Research, Nanoscale Electronics Group, Zurich, Switzerland, September 28 (2012). Group seminar. Oral presentation.
11. **A. V. Senichev**. *Near-field Scanning Optical Microscopy of Infrared Emitting Semiconductor Nanostructures*. Ruhr-Universität Bochum, Bochum, Germany, June 28 (2012). Group seminar. Oral presentation.

Contents

Abstract	iii
1 Introduction	3
1.1 On properties of III–V semiconductors	4
1.1.1 Crystal structure	5
1.1.2 Band structure and energy gap	7
1.1.3 Heterostructures and band engineering	8
1.2 From bulk GaAs to nanowire structures	10
1.2.1 Fabrication of nanowires	10
1.2.2 Wurtzite GaAs and polytypic nanowires	12
1.2.3 Results of previous studies	15
1.3 Scope and main aims of the study	17
2 Experimental methods	19
2.1 Spatially resolved photoluminescence spectroscopy	20
2.1.1 Photoluminescence spectroscopy	20
2.1.2 Spectral imaging and diffraction limit	21
2.2 Introducing the near-field optics	22
2.2.1 Evanescent waves	22
2.2.2 Spatial resolution	23
2.2.3 Near-field scanning optical microscopy	24
2.3 Installation of the microscope	26
2.3.1 Microscope layout	27
2.3.2 Near-field fiber probes	30
2.3.3 Distance control setup	32
2.4 Test measurements of single nano-objects	34
2.4.1 InAs quantum dots grown in nanoholes on GaAs surface	34
2.4.2 Spectral imaging of single quantum dots	35
2.4.3 Conclusion	40
3 Experimental protocol for the nanoscale study of single nanowires	41
3.1 Introduction	41
3.2 Overview of the protocol	42
3.3 Procedure	43
3.3.1 Sample preparation for the single-nanowire measurements	43
3.3.2 Spectral imaging by near-field scanning optical microscope	45
3.3.3 Extraction of nanowires for the structural characterisation	45
3.3.4 Characterisation of nanowires by electron microscopy	47

3.4	Anticipated results	50
3.5	Summary	52
4	Electronic properties of crystal-phase heterostructures in GaAs nanowires studied by near-field spectral imaging	53
4.1	Introduction	53
4.2	GaAs–AlGaAs core-shell nanowires grown on Si	55
4.2.1	Growth parameters	55
4.2.2	Morphology and crystal structure	55
4.3	Experimental details	56
4.4	Near-field spectral imaging of individual nanowires	58
4.4.1	Outcome of the single-nanowire experiment	58
4.4.2	Near-field map of the local carrier recombination	60
4.5	Imaging of the crystal structure of nanowires	62
4.6	Structure-property relationships at the nanoscale	65
4.6.1	Correlation of spectral imaging and structural analysis	65
4.6.2	Emission at energy above the band gap of zinc blende GaAs	66
4.6.3	Carrier confinement in individual crystal-phase nanodomains	72
4.7	Summary	79
5	Effects of beryllium doping on local optical properties of GaAs nanowires	81
5.1	Introduction	81
5.1.1	Doping of III–V semiconductor nanowires	81
5.1.2	Impact of doping on nanowire properties	82
5.2	Be-doped GaAs–AlGaAs core-shell nanowires	83
5.2.1	Growth and <i>in situ</i> beryllium doping	83
5.2.2	Morphology	83
5.3	Experimental details	84
5.4	Near-field spectral imaging and structural analysis	84
5.5	Be-doping induced band gap reduction	89
5.5.1	Photoluminescence spectra of Be-doped zinc blende GaAs	89
5.5.2	Evaluation of the hole concentration	90
5.6	Twinning superlattice in Be-doped GaAs nanowires	93
5.7	Summary	96
6	Conclusion	99
	References	101
	Curriculum vitae (Lebenslauf)	115

Abbreviations

ADF	– Annular dark-field
AFM	– Atomic force microscopy
CCD	– Charge-coupled device
CL	– Cathodoluminescence
EDXS	– Energy-dispersive X-ray spectroscopy
EELS	– Electron energy loss spectroscopy
fcc	– Face-centered cubic lattice
FIB	– Focused ion beam
FWHM	– Full width at half maximum
HAADF	– High-angle annular dark-field
hcp	– Hexagonal close-packed lattice
HF	– Hydrofluoric acid
HRTEM	– High-resolution transmission electron microscopy
LED	– Light-emitting diode
MBE	– Molecular beam epitaxy
ML	– Monolayer
MOCVD	– Metal organic chemical vapour deposition
NA	– Numerical aperture
NSOM	– Near-field scanning optical microscopy
NW	– Nanowire
PID	– Proportional-integral-derivative controller
PL	– Photoluminescence
QD	– Quantum dot
QW	– Quantum well
RT	– Room temperature
SEM	– Scanning electron microscopy
SK	– Stranski – Krastanov
SNOM	– Scanning near-field optical microscopy
STEM	– Scanning transmission electron microscopy
TEM	– Transmission electron microscopy
TSL	– Twinning superlattice
VLS	– Vapour-liquid-solid
WZ	– Wurtzite phase
ZB	– Zinc blende phase

Chapter 1

Introduction

The emergence of novel semiconductor materials with predefined properties and functionality is associated with great achievements in fabrication methods and has a direct impact on the rapid development of a semiconductor-device field. The ability to precisely control structural and composition parameters of semiconductors at the nanometer length scale has been successfully demonstrated over the last decade. This provides possibilities to improve and tailor their optoelectronic properties for applications in advanced light-harvesting and light-emitting devices such as effective solar-cells [1], single-photon quantum emitters [2], on-chip optical interconnects [3], and many others. Technological potentials that appear with the progress in nano-fabrication of semiconductor materials are accompanied with new fundamental challenges. In order to predict and evaluate the performance of new materials, an understanding of physical phenomena at the nanometer length scale and how mechanical, optical and electronic properties of a matter are modified when reaching this scale, is essential. For instance, the large surface to volume ratio of typical nanostructures makes their properties particularly sensitive to the quality of surfaces and interfaces. The dimension of nanostructures, when it is comparable with the wavelength of the electron, requires to take into consideration such quantum phenomena as quantised energy states. Importantly, the full understanding of optoelectronic properties and structure-property relationships at the nanometer length scale can be obtained if we are able to probe and resolve these properties at the same scale.

The main objects studied in this work are gallium arsenide (GaAs) semiconductor nanowires fabricated by the bottom-up epitaxial growth technique. Semiconductor nanowires are one-dimensional structures, which can be characterised by a diameter in the range from a few to 100 nm and a length of about several micrometers. The radial dimension of nanowires may result in a quantum confinement regime of different strength, whereas the one-dimensional nature can influence their optical properties or carrier transport characteristics [4]. Various important parameters of nanowires such as a diameter, a length and an chemical composition can be well-controlled during the fabrication process. A small footprint of free-standing nanowires on the surface allows to combine different materials with a large lattice constant mismatch due to the efficient strain relaxation [5]. This provides a promising approach for a direct integration of the superior properties of III–V semiconductors, e.g. a direct band gap, with silicon technology, which is a long-standing goal of the semiconductor electronics industry [6]. The one-dimensional nature of nanowires leads also to the large surface to volume ratio that makes them promising for applications as a sensing nanomaterials or active elements in e.g. a photocatalytic water splitting [7, 8]. On the contrary, a passivation

of the nanowire surfaces with the wide-band gap materials effectively suppresses surface states, substantially improves optical quality of nanowires [9], and also provides a routine for fabrication of novel radial heterostructures. To summarise, a large amount of contributions and reviews on semiconductor nanowires reveals an upsurge of interest in their fundamental properties as well as possibilities for technological applications [10–14]. As a result, various nanowire-based functional building blocks for electronic and photonic devices have been already demonstrated. For instance, light-emitting diodes [15], solar cells [4], transistors [16], or room-temperature lasers [17]. The rapid development of the field of nanowires may also result in various successful technological spin-offs, e.g. CRAYONANO [18], and have an effect on some important aspects of our life such as an effective and sustainable energy conversion.

In this work, of particular interest is the study of nanoscale phenomena and properties of GaAs semiconductor nanowires, which arise from their unique crystalline structure. Whereas bulk and thin film GaAs have a zinc blende equilibrium crystal structure, nanowires made of GaAs may also exhibit regions with a wurtzite type crystal phase. Since the symmetry of the crystal structure defines the major material properties of semiconductors, the wurtzite phase is expected to have a band gap, band offsets and effective masses that are different from those of the zinc blende phase of the same material. For GaAs nanowires, there is an ongoing debate about the exact values of the band gap of wurtzite GaAs and band offsets between zinc blende and wurtzite GaAs [19–25]. In addition, nanowires typically exhibit a mixture of zinc blende and wurtzite phases along the growth direction. Due to the different band gap energies of these phases, alternation of zinc blende and wurtzite segments produces crystal-phase heterostructures. Optical and electronic properties of such nanowires depend on the lateral extend and order of crystal-phase nanodomains, which have a typical length scale from one to a few tens of nanometers. Therefore, nanowires are considered as important model structures for fundamental studying optical and electronic properties of wurtzite type GaAs and zinc blende–wurtzite crystal-phase heterostructures. The experimental challenge of this study is to probe and resolve optical and electronic properties of GaAs nanowires with a mixture of zinc blende and wurtzite crystal phases alternating at the nanometer length scale.

The physics of nanowires is primarily defined by the physics of corresponding semiconductor materials they compound from. Therefore, a concise overview of selected topics of semiconductor physics relevant for the discussion of experimental results and nanoscale phenomena in nanowires is provided in this chapter. Herein, an introduction is given with a special emphasis on properties of bulk GaAs semiconductor material, which was intensively studied in the past. The discussion of the properties of semiconductors is based on textbooks by M. Grundman [26], J.H. Davies [27], and S.M. Sze [28], unless otherwise specified. The experimental approach applied in this research for investigation of crystal-phase heterostructures in GaAs nanowires will be discussed in *Chapter 2* and *Chapter 3*.

1.1 On properties of III–V semiconductors

The fundamental properties of such common semiconductors as GaAs, InAs, InP, AlGaAs and many others provide a basis for understanding characteristics of novel devices and hybrid functional elements based thereon. In order to discuss properties of crystal-phase heterostructures in GaAs nanowires, a brief survey on a crystal and energy band structure of bulk GaAs, energy band alignment in conventional heterostructures, and other subjects related to this work is given. At the end of this chapter, the state of knowledge and important

issues in the field of III–V semiconductor nanowires are outlined.

1.1.1 Crystal structure

The important characteristic of semiconductor materials is the arrangement of atoms, which is typically well structured and periodic, forming highly symmetric crystals. The crystal structure and the symmetry define essential material parameters of semiconductors. The entire crystal can be reconstructed by multiple repetition of the smallest assembly of atoms, which is called the unit cell, in all three directions. The fixed dimension of the unit cell defines the lattice parameter a of the crystal. Most of III–V semiconductors crystallise in the cubic zinc blende (ZB) crystal phase. On one hand, the ZB structure can be represented by two interpenetrating face-centred cubic (fcc) sublattices, which are displaced with respect to each other by one fourth of the unit cell. The one sublattice consists of group III atoms of the periodic table and the another one is formed by atoms of group V (Fig. 1.1a). Alternatively, the zinc blende lattice structure can be also considered in a way that it belongs to the tetrahedral phases. That is four nearest equidistant atoms of one fcc sublattice lie at the corners of a tetrahedron, while one atom of another sublattice is placed at the centre of this tetrahedron. The central atom can form four bounds with atoms at the corners. The repetition of such structure in all three direction will reconstruct the entire crystal (Fig. 1.1b). The bulk GaAs has a zinc blende equilibrium lattice structure, which is shown in Figure 1.1a. The gallium (Ga) atoms occupy the original sites of the fcc sublattice, while the arsenic (As) atoms occupy the tetrahedral sites, as shown in Figure 1.1b. For the cubic zinc blende unit cell, the length of each site is equal and gives only one lattice constant a , which is about 5.6533 \AA in bulk GaAs at 300 K. The thermal expansion coefficient of GaAs crystal $\alpha_{th} = 6.03 \times 10^{-6} K^{-1}$ describes the change of the lattice constant with a temperature. For comparison, the arrangement of atoms in silicon (Si) crystal is the same as in the zinc blende lattice, but with one species in both fcc sublattices that gives a so-called diamond lattice. However, a considerably different lattice constant $a = 5.4310 \text{ \AA}$ and a thermal expansion coefficient $\alpha_{th} = 2.616 \times 10^{-6} K^{-1}$ of the Si crystal in contrast to those parameters of GaAs make their defect-free integration difficult.

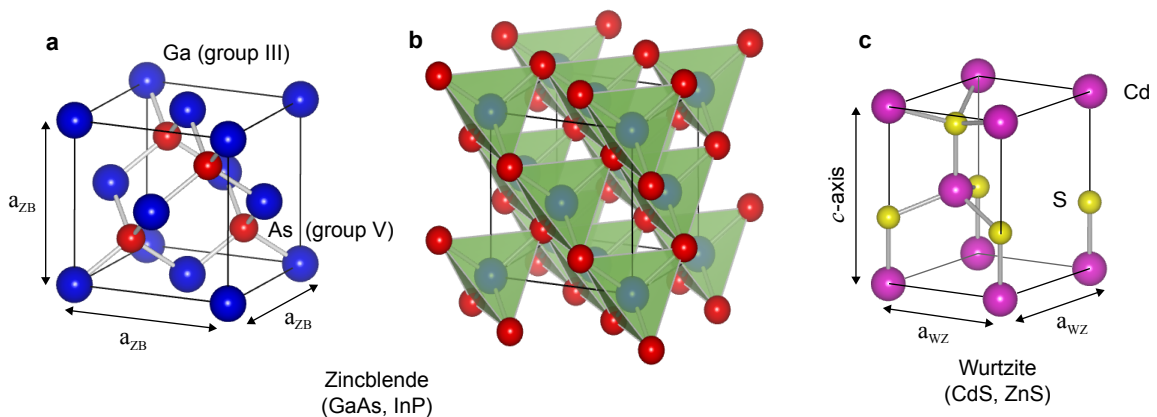


Figure 1.1: (a) Zinc blende structure: blue spheres represent group III elements, red spheres — group V. (b) Tetrahedral representation of a zinc blende structure. (c) Wurtzite structure: group II elements are shown as magenta spheres, group VI — yellow. Adapted from [28].

Whereas most of III–V compounds have the zinc blende lattice structure, group III–nitrides and some of II–VI bulk semiconductors crystallise in the wurtzite structure, which is shown in Figure 1.1c. The wurtzite structure can be defined as two interpenetrating hexagonal closed-packed (hcp) sublattices of different species, e.g. cadmium (Cd) and sulfur (S). The wurtzite structure has also a tetrahedral coordination of neighbouring atoms, similar to a zinc blende lattice. The hexagonal unit cell is not symmetric and thus there are two lattice constants, a and c , to describe it in all three directions (Fig. 1.1c).

For the discussion of properties of semiconductor materials, especially nanostructures, the orientations and properties of their lattice planes have to be introduced. To describe various planes and directions in a crystal, a notation scheme based on Miller indices is used [26]. Lattice planes are indicated with three integer numbers hkl enclosed in parentheses as (hkl) , whereas a set of equivalent planes is denoted as $\{hkl\}$. Similarly, the notations with square brackets $[hkl]$ and $\langle hkl \rangle$ are used for the directions of a crystal and a full set of equivalent directions, respectively. In Figure 1.2a-c, some important lattice planes and directions in bulk zinc blende GaAs are shown.

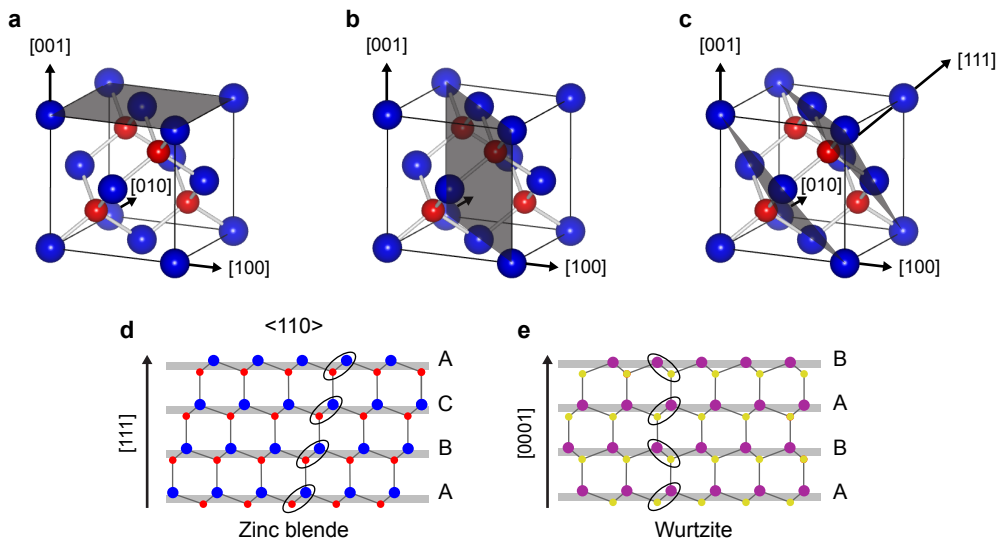


Figure 1.2: Directions and important planes in zinc blende GaAs: (a) (001), (b) (110), (c) (111). Adapted from [27]. d) Model of a zinc blende crystal structure viewed in the $\langle 110 \rangle$ crystallographic orientation. e) Model of a wurtzite crystal structure viewed in the equivalent to $\langle 110 \rangle$ crystallographic orientation. Colour codes correspond to those in Fig. 1.1.

The difference between the zinc blende and wurtzite structures can be revealed by observing their projections along $\langle 110 \rangle$ direction (Fig. 1.2d,e). In the wurtzite structure the Miller indices are introduced by using four integer numbers as $[hk\ell m]$ [26]. The direction in the wurtzite lattice, which is equivalent to $[111]$ in the zinc blende structure, is denoted as $[0001]$ or c -axis (Fig. 1.1c). Along $[111]$ and $[0001]$ directions, both zinc blende and wurtzite structures appear as stacked hexagonal layers, respectively [21]. The $\{111\}$ lattice planes are formed by diatomic layers. They alternate between the anion and the cation [21]. By considering the stacking sequence of lattice planes along $[111]$ direction, the differences between zinc blende and wurtzite structures can be distinguished. The zinc blende (fcc) stacking order is $\dots ABCABC\dots$, where only every third layer is identical to A. In contrast, the wurtzite (hcp) stacking order repeats every second layer and is denoted as $\dots ABABAB\dots$ [26].

1.1.2 Band structure and energy gap

Band structures of the most important semiconductors have been intensively studied theoretically using different approaches [29–31] and verified experimentally [32]. The energy band structure of zinc blende GaAs is well-known and its energy-momentum relationship (E - k) is shown in Figure 1.3. Semiconductors are characterised by the presence of a forbidden energy range where allowed electron states cannot exist. The bands above and below the fundamental energy gap are called the conduction and valence bands, respectively. In Figure 1.3, the bottom of the conduction band is indicated as E_C and separated from the highest valence-band E_V by the energy gap denoted as E_g . The band gap E_g is one of the most important parameters of semiconductors. The GaAs compound semiconductor is a direct band gap E_g material, where both the bottom of the conduction band and the top of the valence band are at the same position $k = 0$ (Fig. 1.3, Γ point). In some semiconductors, the minimum of the conduction band does not coincide in k -space with the valence band maximum resulting in the indirect band gap, as for example in the case of Si.

The band gap energy E_g of bulk zinc blende GaAs at room temperature and under normal atmospheric pressure is 1.424 eV, whereas at a temperature close to 0 K it approaches 1.519 eV. The band gap of most semiconductors decreases with increasing temperature. The variation of the band gap energy with temperature can generally be approximated with the empirical formula [33]:

$$E_g(T) \approx E_g(0) - \frac{\alpha T^2}{T + \beta} \quad (1.1.1)$$

where $E_g = 1.519$ eV, $\alpha = 5.4 \times 10^{-4}$ eV/K, and $\beta = 204$ K for bulk GaAs.

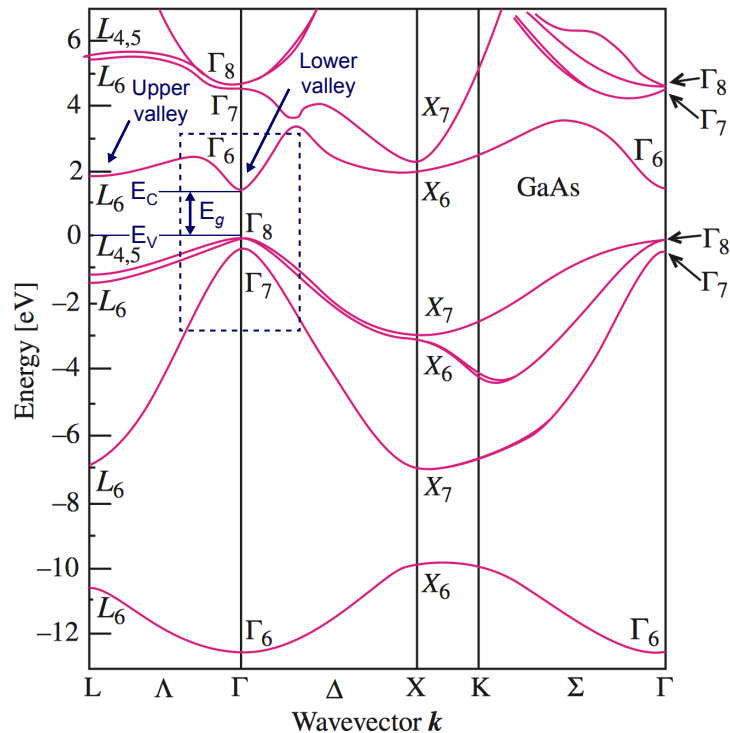


Figure 1.3: Calculated band structure of bulk zinc blende GaAs by the pseudopotential method [34]. From [35].

1.1.3 Heterostructures and band engineering

Heterostructure materials are generally formed by a combination of two semiconductors with similar lattice constants a , but different energy gaps E_g . The main idea of growing semiconductor heterostructures is the opportunity they provide to manipulate the behaviour of charge carriers by tailoring the energy band structure, e.g. utilising quantum confinement effects such as quantised energy levels. A classical example is the AlGaAs–GaAs–AlGaAs quantum well, where a layer with a smaller band gap (GaAs) is placed between two larger band gap slabs (AlGaAs). To produce the defect-free heterointerfaces between two different semiconductors, the matching of lattice constants is essential. The change of lattice constant from GaAs to $\text{Al}_x\text{Ga}_{1-x}\text{As}$ is less than 0.15 % over the whole range of x . This facilitates producing a defect-free GaAs–AlGaAs heterojunction without significant strain. The heterostructures are typically fabricated by epitaxial layer-by-layer growth of lattice-matched semiconductor materials on top of each other. The combination of semiconductors with a slight lattice constant mismatch is also possible, but limited by the thickness of the defect-free epitaxial layer. This thickness is defined by the maximum strain that this layer can accommodate to match the lattice constant of the host material prior to the formation of dislocations at their interface. The growth of such strained heterostructures allows a larger variety of semiconductor materials to be included for the band engineering.

In heterostructures, alignment of conduction bands and valence bands at the heterointerface between two materials is determined through electron affinities, also known as *Anderson's rule* [26,27]. The electron affinity χ defines the energy required to promote an electron from the bottom of the conduction band E_C to the vacuum level. According to *Anderson's rule*, the vacuum levels of two materials of a heterostructure should be aligned with each other, that can lead to different types of heterostructures. This rule allows to define a type of the resulting band alignment, while it is less accurate in predicting actual band offsets (ΔE_C , ΔE_V). In Figure 1.4, two types of heterojunctions between two materials A and B with $E_g^A < E_g^B$ are shown.

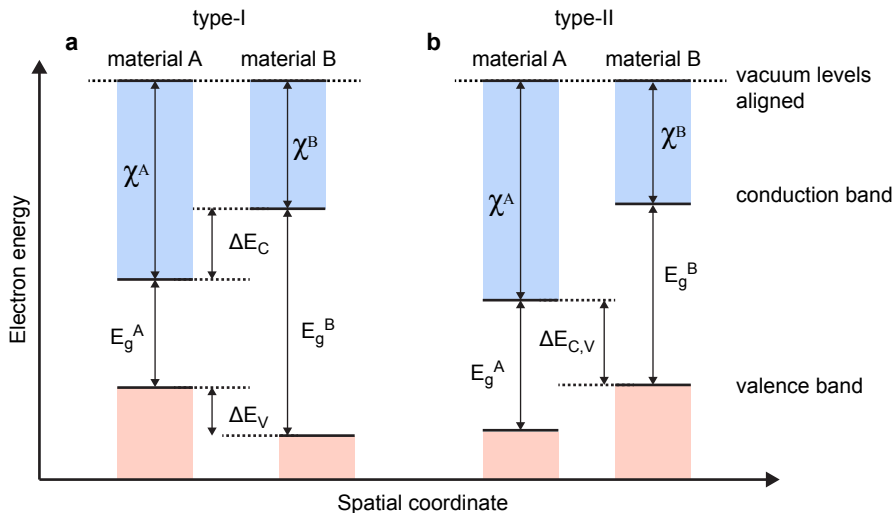


Figure 1.4: Anderson's rule for the alignment of the bands in heterostructures. Position of band edges: (a) type-I heterostructure, (b) type-II heterostructure. Adapted from [26,27].

In a type-I or straddling alignment (Fig. 1.4a), the material A has the lower conduction

band E_C edge and the higher valence band E_V edge in comparison to the larger band gap material B. If the narrow band gap material A is placed into the wider band gap matrix B, both electrons and holes tend to trap in the material A. Such band alignment is characteristic for GaAs–AlGaAs heterostructures. In a type-II or staggered alignment (Fig. 1.4b), the material B has a positive offset for both E_C and E_V edges. The electrons and holes will occupy the lowest states in the conduction (material A) and valence (material B) bands of the heterostructure, respectively. Therefore, the charge carriers will be spatially separated across the heterojunction between two materials. This can lead, for instance, to longer carrier life time in the type-II heterostructures in comparison to the regular material.

The position of the conduction and valence band edges can be tailored in heterostructures to produce barriers for electron and holes that control their motion. The discussed above GaAs quantum well enclosed between thick layers of AlGaAs confines carriers in a two-dimensional system. Their energy becomes quantised in subbands in the direction of growth of the heterostructure. The energy of these states depends on the depth and the width of the quantum well and can be controlled during the growth by changing the elemental composition and the thickness of layers, respectively. In Figure 1.5, some important examples of heterostructures are shown. In case of a wide barrier layer between two adjacent quantum wells, so that their wavefunctions do not overlap, they can be considered as uncoupled quantum wells and treated individually (Fig. 1.5b). Whereas, when the barrier is thin enough that wavefunctions of neighbouring quantum wells overlap, the tunnelling of carriers from one quantum well to another has to be considered. A series of quantum wells with thin barriers forms a heterostructure superlattice, which creates a periodic potential (Fig. 1.5c). Discrete levels of individual quantum wells are transformed into wider bands (“minibands”) in the superlattice. Moreover, these bands are delocalised in a space across the barriers.

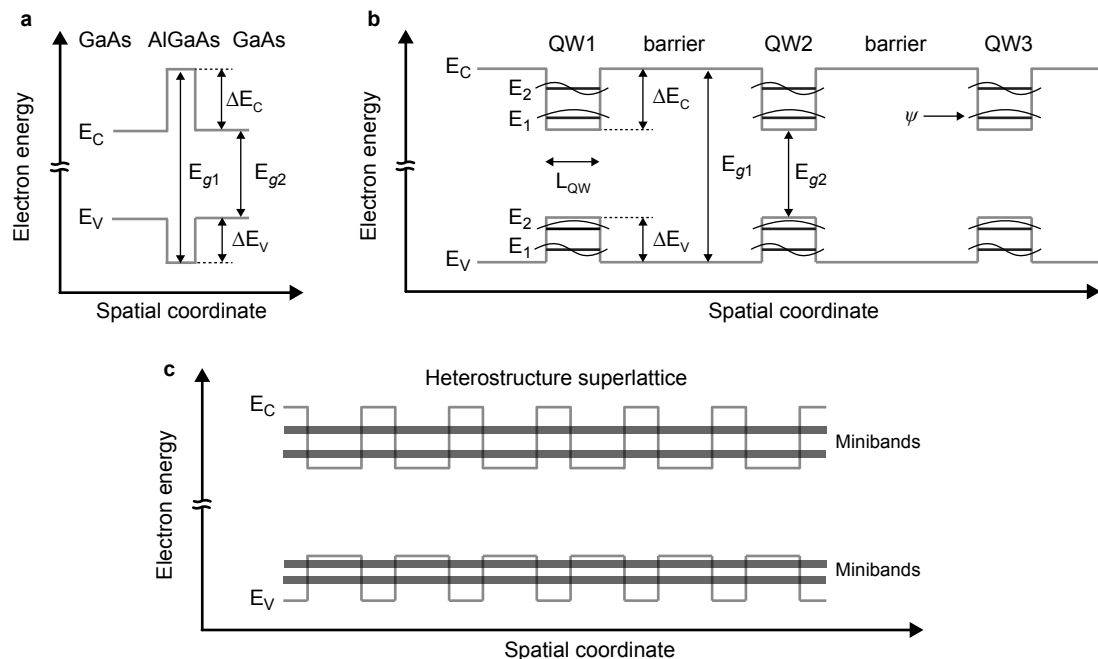


Figure 1.5: Profiles of energy bands of layered heterostructures: (a) Single-barrier tunnelling structure. (b) Uncoupled quantum wells separated by thick barriers. (c) Periodic potential of the heterostructure superlattice and the miniband structure (grey). Adapted from [28].

1.2 From bulk GaAs to nanowire structures

Having summarised important properties of GaAs semiconductor material and heterostructures based thereon, the current state of knowledge and challenges related to III–V compound nanowires, and GaAs nanowires in particular, are discussed. Herein, the emergence of important physical phenomena and properties of nanowires due to reducing dimensions of GaAs from bulk material to one-dimensional nanostructures is reviewed. To explore the physics in reduced dimensions, the fabrication of nanowires with precise control of the structure, chemical composition, and crystal structure purity is desired. Therefore, the discussion is started with the nanowire growth methods.

1.2.1 Fabrication of nanowires

The emergence of nanowires with well-controlled structural parameters has become possible due to the immense progress in the fabrication technology and understanding fundamentals of growth processes. Different approaches can be applied for the one-dimensional nanowire fabrication, whose principles are discussed in [11, 13, 36]. Fabrication methods are generally divided into the top-down and bottom-up approaches. The former involves the formation of nanowires from the bulk material by the lithographic patterning of a surface and selective etching [37]. The latter one relies on the chemical synthesis of nanowires via deposition of chemical elements on a substrate. The important advantage of the bottom-up approach is a better control on parameters of nanowires during the growth [13]. The formation of one-dimensional nanowires occurs due to the different growth rates of a material in different directions. The growth starts at a single point defined by a catalyst nanoparticle. Then, nanowires become elongated in the direction, which has the highest growth rate [11].

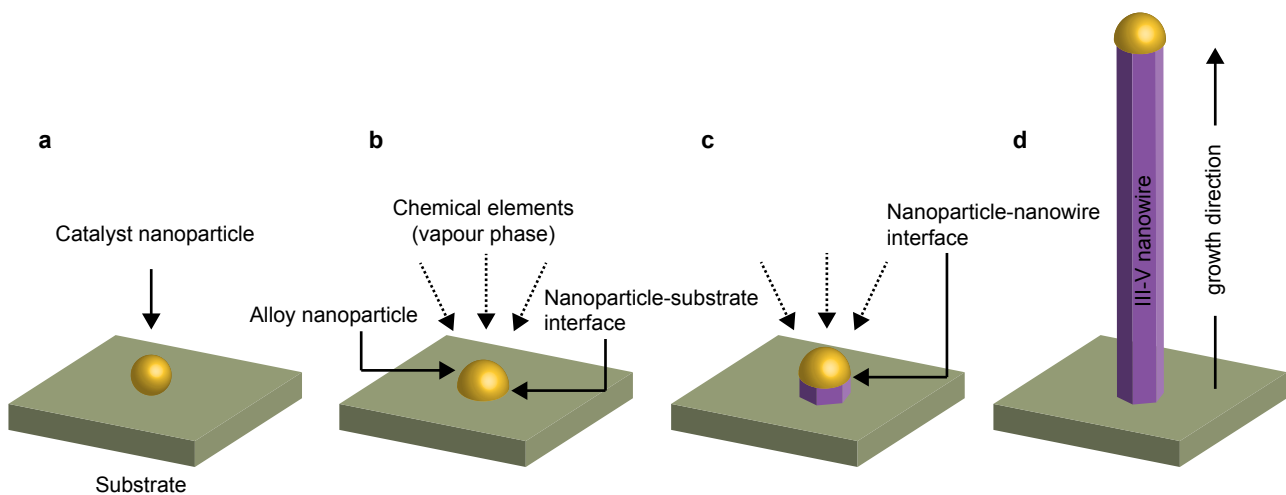


Figure 1.6: Schematic representation of the nanowire growth process: (a) Catalyst nanoparticles (Au or Ga) are deposited on the growth substrate. (b) Chemical elements (Ga, As) are introduced in the vapour phase to the growth chamber. They form an alloy with nanoparticles. Nucleation occurs at the interface between the supersaturated catalyst nanoparticle and the substrate. (c, d) Growth continues predominantly at the interface between the nanoparticle and the nanowire. Adapted from [11].

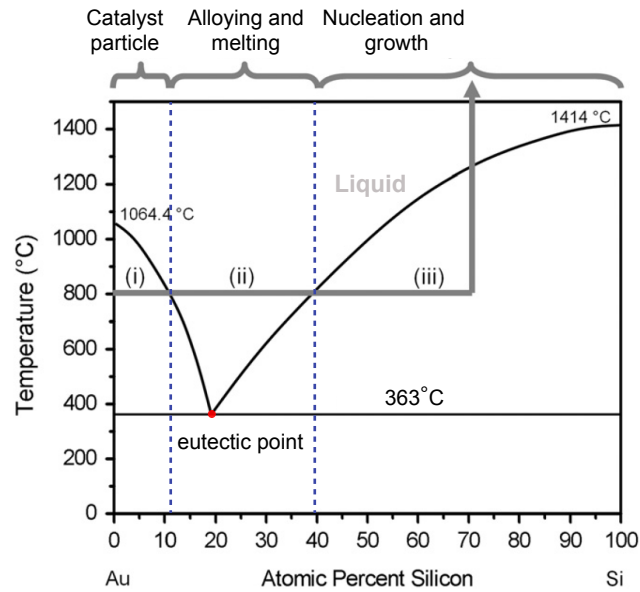


Figure 1.7: The phase diagram shows various phases of the Au-Si mixture at different temperature and composition ranges. The eutectic point of the Au-Si alloy is at a temperature of 363°C. The different stages of the nanowire growth at a given surface temperature of 800°C are separated by the dashed lines. Adapted from [11].

The vapour-liquid-solid (VLS) growth mechanism is one of the most widely used methods for bottom-up fabrication of free-standing nanowires [13]. The VLS method was originally developed by Wagner and co-workers in 1964 to produce Si nanowires [38] and was later adapted to grow III–V compound nanowires [39]. The growth of nanowires by VLS method involves vapour, liquid and solid phases of the material and occurs in three general steps: alloying, nucleation, and growth. The schematic of this mechanism is shown in Figure 1.6 and can be qualitatively described as follows: First, metallic particles are formed on the surface of a growth substrate (e.g. Au particles on a Si substrate [38]). Then, chemical elements are supplied in the vapour phase into the growth chamber and adsorbed by a metallic droplet. The adsorbed elements form a liquid eutectic alloy with the droplet of a catalyst reducing the melting temperature of the alloy in comparison to its constituents. For instance, a phase diagram for the binary Au-Si mixture indicating its various phases as a function of different temperatures and compositions is shown in Figure 1.7. The further supply of chemical elements changes the alloy composition, and the alloy becomes supersaturated at the selected growth temperature. As a result, the source material precipitates at the droplet-substrate interface forming a solid phase that initiates the nucleation and lateral extension of 2D islands [40]. This leads to a vertical layer-by-layer growth of the nanowire under the catalyst. The liquid droplets on the substrate serve as a preferred adsorption area for the vapour phase, promoting the nanowire growth predominantly at the droplet-nanowire interface. Therefore, there is the direction with the highest growth rate, and the diameter of the wire is guided largely by the diameter of the initial droplet.

The III–V nanowires are typically grown using a VLS-like mechanism as described above. For GaAs nanowires, the growth can be initiated by Au or Ga nanoparticles known as Au- or Ga-assisted [41] growth processes, respectively. The VLS growth of nanowires is typically performed by applying standard growth systems, such as molecular beam epitaxy (MBE) [42]

or metal organic chemical vapour deposition (MOCVD) [43]. The nanowires studied in this thesis are grown applying MBE growth techniques. The detailed information about the growth mechanisms of nanowires and underlying physical processes can be found in the following reviews [11, 36, 40, 44].

1.2.2 Wurtzite GaAs and polytypic nanowires

From the fundamental point of view, many exciting phenomena and properties of nanowires are expected to arise from their unique crystalline structure. As previously discussed, most of III–V bulk semiconductors have a zinc blende stable crystal structure. However, III–V compound nanowires may exhibit both cubic zinc blende (ZB) and hexagonal wurtzite (WZ) crystal phases, which are often accompanied by twin planes and stacking faults. This means, that the formation of the WZ crystal phase, which is not existent in a bulk analog of the same material, is observed in the nanowire. In the work done by F. Glas *et al.* [45], the existence of the wurtzite phase in nanowires of III–V zinc blende semiconductors is explained applying a nucleation-based model. It was suggested that the nucleation during the nanowire growth occurs predominantly at the vapour-liquid-solid triple phase line, where zinc blende and wurtzite nuclei exhibit major differences. Importantly, the wurtzite formation at this line is preferential for particular ranges of the interface energies [45]. Moreover, it was found that the wurtzite phase formation is favoured, when the supersaturation of the liquid alloy is high [45]. Experimentally, the formation of zinc blende or wurtzite phases shows a dependence on such growth parameters as V/III compounds ratio, growth temperature and the wire diameter [46, 47].

Since the crystal structure defines important material properties of semiconductors, the formation of WZ phase is expected to modify the energy band structure in comparison to that of ZB phase in the same material. Thus, the structural difference between ZB and WZ phases and their coexistence in GaAs nanowires is first considered. The crystal structure of ZB GaAs was discussed in detail in previous sections and is shown in Figure 1.1a. As it was previously mentioned, the difference between ZB and WZ phases (Fig. 1.2d,e), twin planes, and stacking faults can be distinguished by observing their crystal structure in the $\langle 110 \rangle$ crystallographic orientation. The typical nanowire growth direction $[111]$ goes along the diagonal of the ZB unit cell (Fig. 1.1a), whereas in the WZ unit cell along the c -axis (Fig. 1.1c). In the nanowire with a mixture of two phases, both ZB and WZ structures along the $[111]$ growth direction are viewed like stacked hexagonal bilayers, composed of a pair of one Ga (group III) and one As (group V) atom (Fig. 1.8a) [21]. The difference between close-packed ZB and WZ structures lies in the stacking order of these bilayers [11]. To identify the ZB and WZ phases and determine twin planes and stacking faults, the ABC notation system of lattice planes stacking is applied as illustrated in Figure 1.8a. The stacking sequence of ZB lattices in GaAs is $\dots ABCABC\dots$ and WZ lattices is $\dots ABABAB\dots$, where each letter represents a Ga-As bilayer. As shown, in the ZB stacking every third bilayer is repeated, whereas in the WZ stacking every second bilayer is repeated. The difference between the ABC and the ABA stacking is that the third bilayer in the WZ phase is rotated by 60° around the $[111]$ growth axis in comparison to the third bilayer in the ZB phase (Fig. 1.8b).

The mentioned above planar defects, such as twin planes and stacking faults, often appear in GaAs nanowires. The emergence of twin planes in ZB crystals corresponds to a wrongly stacked single bilayer, which alters the stacking sequence from $\dots ABCABC\dots$ to $\dots CBACBA\dots$. Thus, ZB regions with $\dots ABCABC\dots$ stacking sequence are followed by

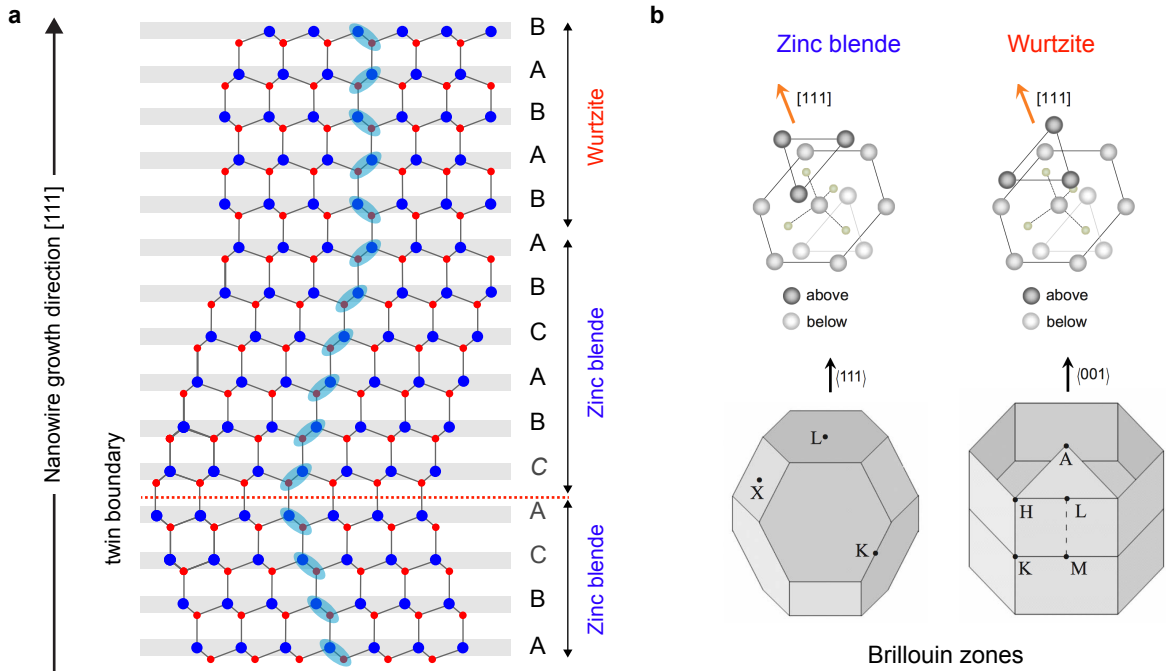


Figure 1.8: (a) Crystal structure model of the GaAs nanowire viewed in the $\langle 110 \rangle$ crystallographic orientation. The blue spheres indicate Ga atoms, the red spheres – As, respectively. The red dashed line indicates the twin boundary between two ZB segments. The inclusion of a single unit of WZ structure at the twin boundary is highlighted by the grey CAC letters. The WZ stacking sequence ... ABABAB... is shown in the upper part of (a). (b) Top panel: configuration of atoms viewed along [111] direction for ZB and WZ crystal structures. Note the difference between atoms arrangements in the third layer of ZB and WZ lattice. Bottom panel: Brillouin zones for ZB and WZ phases. From [21].

segments with the same ZB structure, but with its atomic arrangement rotated by 180° at the twin boundary¹ around the [111] growth axis, as illustrated in the lower portion of Figure 1.8a. The misplacement of a single bilayer in zinc blende crystal changes the structure, which is referred to as rotational twinning. Importantly, the rotational twinning forms an ... ABCACBA... stacking sequence, where *C* is the misplaced bilayer and the CAC stacking at the twin boundary can be considered as an inclusion of a single unit of a WZ structure in a ZB matrix. Therefore, the interface between two twins is interpreted as a very short segment with wurtzite symmetry, which has to be taken into consideration while discussing corresponding optical properties of such structures [48]. Note that the WZ crystal structure can be considered as a ZB structure where twin plane occurs at every bilayer (Fig. 1.8a, upper part). Similar to rotational twinning, stacking faults in WZ structures corresponds to a faulty stacked single bilayer that generates the sequence ... ABABCBCB... containing a stacking fault at the bilayer *C* [47]. The misplacement of a single bilayer in wurtzite structure creates a single unit of ZB structure with the corresponding ABC stacking [47].

The alternation of ZB and WZ crystal phases within a single nanowire, including the varying density of planar crystallographic defects, can be considered as an undesired structure full

¹Note that the 180° -turn of atoms arrangement at the twin boundary observed in $\langle 110 \rangle$ projection corresponds to the actual 60° rotation of the lattice planes in a crystal.

of defects in comparison to pure stacking-faults-free ZB and WZ nanowires. However, if the controlled formation of alternating regions of different phases in the same nanowire could be achieved, the fabrication of novel axial heterostructures with tailored own optical and electronic properties would be possible. Importantly, the precise modulation of the crystal structure in nanowires provides opportunities for the band gap engineering without changing the crystal material. The formation of nanowires with a pure crystal structure or polytypic nanowires with a different order and lateral extend of ZB/WZ crystal phases is determined by the growth parameters. The growth of ZB and WZ segments in nanowires can be guided by the flux ratio of V/III elements [49, 50], the diameter of nanowires and the growth temperature [11, 47], using impurity dopants [51] and the controlled interruption of the growth process [52], or by various combinations of these parameters. A significant effort has been made over the last decade to grow nanowires with a controlled crystal structure [50, 52–54]. For instance, under certain growth conditions twin planes can have a constant spacing, forming a new class of so-called twinning superlattices [51, 55] and opening opportunities for the electronic band structure engineering [56]. The transmission electron microscopy images of InP nanowires with twinning superlattices are shown in Figure 1.9. The ability to control periodic arrangements of twinning superlattices was also reported for other III–V compound nanowires [47, 51, 55, 57]. Even though the ability to produce nanowires with thin and extended ZB and WZ segments without unintentional stacking defects [53] or defect-free ZB nanowires [58] were demonstrated, the growth of nanowires with precisely controlled structural parameters remains a challenging task.

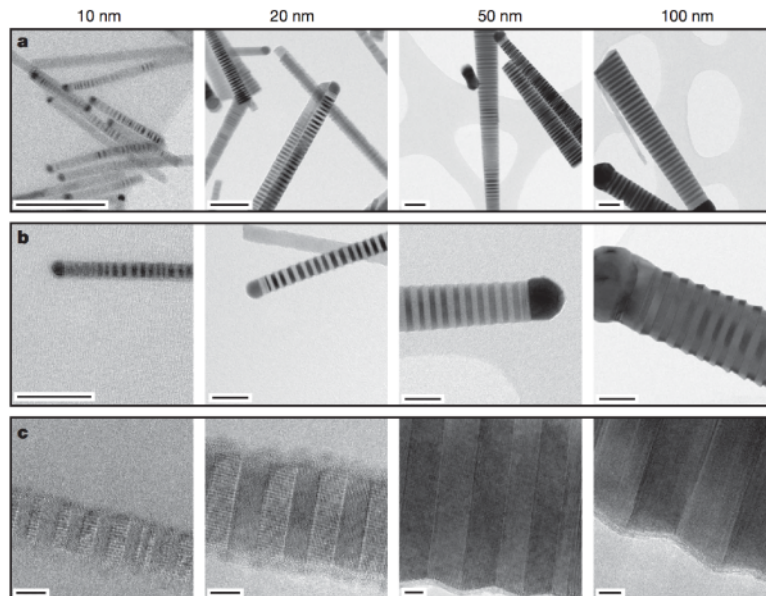


Figure 1.9: Transmission electron microscopy images of InP nanowires with twinning superlattices: (a,b) overview, (c) high resolution. Scale bars: (a) 100 nm, (b) 50 nm, (c) 5 nm. The periodic dark and bright areas correspond to rotationally twinned zinc blende segments, which produce different electron diffraction conditions. From [51].

Indeed, further comprehensive investigations and technological applications evidently require nanowires with a predefined and reproducible length and sequence of WZ/ZB phases. Moreover, it is of fundamental importance to understand better the correlation between

In addition, owing to the fact that the unit cell of a WZ phase along c -axis is twice the length of the unit cell of a ZB phase along the equivalent $[111]$ direction [23], the L point in ZB is zone-folded to the Γ point in WZ [21]. As a result, the zone folding leads to the appearance of an additional conduction band Γ_{8C} close to the Γ_{7C} ZB-like conduction band (Fig. 1.10a) [21]. However, the symmetry of the lowest conduction band in WZ GaAs is discussed controversially [19, 21, 59, 60]. The Γ_{8C} conduction band is expected to exhibit substantially larger electron effective mass than the Γ_{7C} one, which will necessarily influence the properties of WZ GaAs [21]. Thus, the understanding of the minimum of the conduction band in WZ GaAs is also important for its device applications. In the recent theoretical work of A. De and C. E. Pryor [21], the energy band structure of WZ GaAs is suggested to have the lowest conduction band of Γ_{8C} symmetry, which has to be verified experimentally.

One of the most controversially discussed question is the band gap energy E_g^{WZ} of the WZ GaAs. The theoretical calculations predict the band gap energy of WZ GaAs to be different from that of the ZB structure. However, the exact values of the band gap energy show an apparent lack of consistency [19, 21]. Moreover, the experimental findings on WZ GaAs nanowires show a large variety of the E_g^{WZ} values. From the recent results on luminescent spectroscopy measurements, the values for the band gap and free-exciton energy of WZ GaAs of 1.517 [23], 1.521 [23, 61], 1.50 [22], and 1.519 [62] eV have been suggested.

Properties of crystal-phase heterostructures

A particular interest lies in possibilities to tune optical and electronic properties of GaAs nanowires by controlled crystal phases formation. Similarly to heterostructures formed by the alloy composition ordering (Fig. 1.5), the alternation of ZB and WZ segments in GaAs nanowires would produce so-called crystal-phase heterostructures [63], since the electron confinement is achieved only by the change in the crystal phase of the same material. In the work of N. Akopian *et al.*, the occurrence of crystal-phase quantum dots in a InP nanowire was shown using such types of experiments as transmission electron microscopy, photoluminescence spectroscopy, lifetime, and photon correlation measurements [63]. Due to the atomically sharp interfaces, one may expect that such crystal-phase nanostructures exhibit a higher optical quality, than it can be obtained with semiconductor heterostructures of different composition.

Clearly, the complete picture of the energy band structure of both ZB and WZ GaAs is essential to predict the optical and electronic properties of crystal-phase heterostructures. As it was shown above, there is the inconsistency between results on the exact value of the WZ band gap and the band gap offset between WZ and ZB GaAs. However, it is commonly accepted that the interfaces between both phases produce the type-II band alignment with positive WZ conduction and valence band offsets (Fig. 1.10b) [22, 25, 64]. Electronic properties of such crystal-phase heterostructures can be studied optically by various luminescence spectroscopy techniques. Importantly, a direct correlation of spectral characteristics of individual crystal-phase nanodomains to their structural parameters is required in order to derive corresponding electronic structure. Even though such correlation was previously demonstrated by several authors [22, 60, 64], there is still uncertainty in extracted experimental parameters. For instance, the assignment of the emission energy to a certain order and lateral extent of crystal-phase domains in individual nanowires is hindered by the alternation of ZB and WZ phases on the nanometer length scale and the limited spatial resolution of experimental techniques.

Doping of nanowires

As it was mentioned above, the small footprint of nanowires enables the efficient strain relaxation, which allows the integration of materials with the high lattice constant mismatch. This is particularly important for a combination of III–V semiconductor materials with the Si technology for various device applications. In addition, the control of the conductivity of the nanowires is essential for the most nanowire-based electronic devices. The impurities are typically introduced during the epitaxial growth providing *in situ* doping of nanowires. The controlled doping of semiconductor nanowires enables the fabrication of the broad range of optoelectronic devices such as single quantum dot nanowire LEDs [65] or *p-i-n* nanowire photovoltaic devices [66].

In situ doping has effects on optoelectronic properties of nanowires, but can also influence their growth rate and crystal structure. For instance, Algra *et al.* reported in their work [51] that the crystal structure of InP nanowires can be controlled using dopants incorporation. It was found that zinc introduced during the growth stimulates crystallisation of InP nanowires in the zinc-blende crystal structure instead of the wurtzite one [51]. The impurity doping provides hence an additional tool for the crystal phase engineering, although affects optical and electronic properties of nanowires. Therefore, it is of the high interest to study the joint contribution of dopants and crystal structure on optoelectronic properties of semiconductor nanowires. This includes understanding of mechanisms of dopant incorporation in such one-dimensional nanostructures, their spatial distribution and evaluation of carrier concentrations. Even though various devices were designed using *in situ* doping of nanowires, the fundamental understanding of nanowire doping requires experimental techniques capable of providing simple and quantitative doping measurements [67].

1.3 Scope and main aims of the study

In order to improve GaAs nanowires comprising crystal-phase heterostructures for applications in novel optoelectronic devices, the understanding of the wurtzite GaAs energy band structure and coexistence of zinc blende and wurtzite crystal phases in such wires is essential. Within the scope of this thesis, the main focus is the experimental probing of local optoelectronic properties of GaAs nanowires by means of near-field scanning optical microscopy. From a fundamental point of view, the present study is aimed to provide a better insight into the structure-property relationships in crystal-phase heterostructures of GaAs nanowires resolved at the length scale that has been not fully achieved in previous studies.

Therefore, the first part of the thesis work is dedicated to installation and revealing experimental capabilities of a near-field scanning optical microscope for imaging local charge carrier recombination in semiconductor nanostructures. For the purpose of providing a direct nanoscale structure-property correlation in individual nanowires, an experimental protocol combining near-field spectral imaging and structural analysis by transmission electron microscopy of one and the same nanowire is set up. In the next part of the thesis research, the characterisation of single GaAs nanowires by this technique is aimed to assign individual emission bands to the particular crystal-phase heterostructures with a lattice-resolved structural information. This facilitates the main objective of the study, which is focused on providing accurate quantitative parameters required for a theoretical modelling of the energy band structure of GaAs nanowires comprising ZB and WZ crystal-phase nanodomains. In order to address the effect of doping on optoelectronic properties of nanowires, the joint

contribution of the crystal structure inhomogeneity and doping to local photoluminescence spectra of beryllium doped GaAs nanowires is resolved in the last part of this study.

The thesis consists of six chapters and is organised in the following way. In *Chapter 2*, the advanced experimental technique to probe local optical properties of individual nanostructures with a high spatial resolution is discussed. This chapter describes principles of near-field optical microscopy and the installation of the home-build near-field scanning optical microscope operating at cryogenic temperatures. The near-field setup was installed and tested during the first year of the present study. *Chapter 3* is dedicated to the details of the experimental protocol allowed to perform both near-field spectral imaging and structural analysis by transmission electron microscopy on one and the same nanowire.

Chapters 4 and *5* are focused on fundamental studies of local optical and electronic properties of GaAs–AlGaAs core-shell nanowires by the experimental approach described in previous chapters. The sub-wavelength resolution imaging of emission from individual nanowires reveals a distinct spatial variation of its spectral parameters such as photoluminescence intensity and peak energy along the nanowire axis. The structure-property correlations in such wires are discussed combining results of nanospectroscopic imaging and transmission electron microscopy measurements. In *Chapter 4*, the characteristic emission from individual crystal-phase heterostructures is identified and discussed. The model of the band alignment and the radiative recombination path in such heterostructures are suggested using experimentally derived quantitative parameters. *Chapter 5* is devoted in particular to the effect of doping on optical properties of individual heavily beryllium doped GaAs nanowires. The formation of a twinning superlattice in this type of nanowires is observed and its optoelectronic properties are discussed.

The summary of the thesis work is given in *Chapter 6*, which provides an overview of most important results and outlines prospects for future research.

Chapter 2

Spectral imaging with near-field scanning optical microscopy

The band gap energy of most common semiconductors lies in the energy range of optical photons. In a semiconductor illuminated by light, a fraction of the incident radiation can be absorbed, and electrons are excited from the valence band to the conduction band, if the energy of photons is sufficient. In turn, photoexcited electrons can recombine with holes and emit photons of a certain frequency. Such electronic transitions, which occur between different bands or energy levels, result in absorption and emission of electromagnetic waves at characteristic energies. Thereby, measurements of corresponding optical spectra provide direct information about the electronic properties of semiconductors [35]. In addition, optical measurements represent a non-destructive and typically easy to perform experimental approach, which does not require special preparations of a sample. Therefore, optical measurements are considered as one of the most important methods to probe electronic properties of semiconductors and nanostructures based thereon. The absorption, scattering, and emission of electromagnetic waves by semiconductors can be used for studying electrons localised on various defects, revealing the dynamics of charge carriers, electron spin states as well as lattice vibrations [35, 68].

In this thesis, the photoluminescence spectroscopy is used to study electronic properties of crystal-phase heterostructures in GaAs semiconductor nanowires. In order to reveal the energy levels resulting from the alternation of zinc blende and wurtzite segments of different length along the wire, spatially resolved photoluminescence spectroscopy technique is applied. Importantly, such alternation generally occurs on the length scale below 100 nm, which requires experimental techniques capable to provide a sub-diffraction-limited spatial resolution. Herein, the near-field scanning optical microscope operating at cryogenic temperatures is utilised to probe local photoluminescence spectra of crystal-phase heterostructures, which were not accessible with conventional far-field microscopy techniques used in previous studies. This chapter outlines principles of photoluminescence spectroscopy and limitations of spectral imaging of nanostructures, which arise from fundamental properties of light. Theoretical basics of high-resolution optical microscopy are introduced underlying the origin of the diffraction limit. Thereafter, the concept of near-field scanning optical microscopy and a design of experimental setup used in this work are discussed. The first test measurements by our custom-made near-field scanning optical microscope are summarised at the end of the chapter.

2.1 Spatially resolved photoluminescence spectroscopy

Spatially resolved spectroscopy, or spectral imaging, allows the investigation of optoelectronic properties of semiconductors resulting from spatial inhomogeneity of structural parameters, an alloy composition or a dopants distribution, which will necessarily influence their local optical spectra. For instance, spatially resolved measurements can be used to distinguish between individual emission lines in inhomogeneously broadened spectra of self-assembled quantum dots, which arises from their size and elemental composition fluctuations. In addition, spectral imaging can be used to investigate the diffusion length of excited carriers and transport properties of semiconductor structures with reduced dimensionality [68]. From practical point of view, spectral imaging combines two experimental techniques, namely spectroscopy and imaging, which will be considered in the next sections.

2.1.1 Photoluminescence spectroscopy

Optical processes that involve emission of light from a sample provide a rich information about its energy band structure. In these processes, the sample has to be brought from its ground state to an excited state by some external source of energy. For instance, the sample can be excited by electron bombardment (cathodoluminescence), direct injection of electrons and holes via an external current (electroluminescence), and optical excitation by an external light source and some other means. In order to promote electrons from the valence band to the conduction band by optical excitation, the energy of incident photons has to be larger than the energy of the band gap [35]. The resulting radiative recombination of photoexcited electron-hole pairs is known as a photoluminescence (PL) process. The photoluminescence spectroscopy is a widely used technique for the investigation of energy band structure of semiconductor materials, determination of crystalline quality and impurities incorporation, as well as for the evaluation of their properties for optical applications.

Three general steps of a photoluminescence process are illustrated in Figure 2.1a. In a photoluminescence experiment, the optically excited electrons and holes rapidly thermalise and accumulate at the edge of the conduction and valence bands, respectively, after some energy loss via electron-phonon interaction, referred to as a relaxation. The relaxation (thermalisation) time is shorter than the radiative recombination time, which is on the order of 10^{-9} s for the direct band gap semiconductors [35]. For instance, the thermalisation of photoexcited carriers in GaAs occurs within 100 fs after excitation [69]. The excess electrons and holes at the bands extrema can then radiatively recombine by emitting photons of characteristic energy, which is typically lower than the energy of the incident photons. The probability of radiative band-to-band recombination is high in semiconductors with a direct band gap, such as GaAs, which are strong emitters and hence used for optical applications [35]. In addition, electrons and holes can recombine via impurity energy levels and those energy levels formed by heterostructures, or at non-radiative recombination centres. The resulting PL spectrum provides thereby a precise fingerprint of the energy levels in the measured structure.

In Figure 2.1b, the experimental PL spectrum acquired from the epitaxially grown GaAs layer at a temperature of 10 K is shown. Two pronounced PL peaks at energies of $E_1=1.495$ and $E_2=1.516$ eV correspond to radiative recombination paths highlighted in Figure 2.1a. In high quality semiconductors at low temperatures, the Coulomb interaction between the excited electron and holes is expected to result in the formation of excitons [35]. The

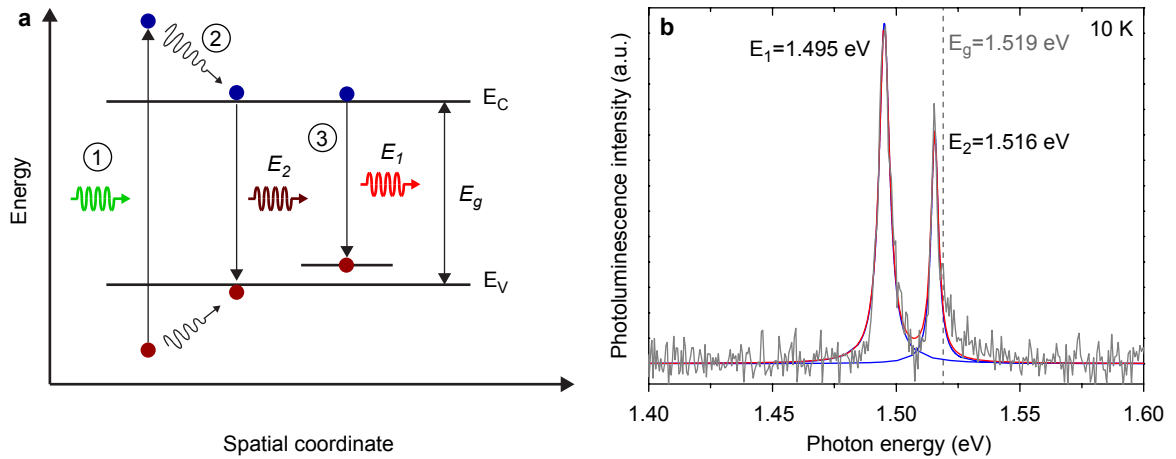


Figure 2.1: a) Photoluminescence process: (1) *excitation* — absorption of incident photons with energies exceeding E_g and generation of electron-hole pairs; (2) *thermalisation* — relaxation of electron-hole pairs and their accumulation at the bands edge; (3) *recombination* — emission of photons by radiative recombination of electron-hole pairs at energies, which correspond to the energy levels of the sample. b) Photoluminescence spectrum of the epitaxially grown GaAs layer measured at a temperature of 10 K (grey). The solid red and blue curves represent a fitting of the experimental data.

radiatively recombined excitons emit photons at the energy slightly smaller than that of the band gap. This reduction is proportional to the binding energy of electron and holes [35]. The band gap of zinc blende GaAs at 10 K is about 1.519 eV. Therefore, the PL peak at the energy of 1.516 eV can be assigned to the free-exciton peak (E_2) [70]. The epitaxially grown GaAs can contain a small number of impurities, typically carbon. The corresponding acceptor energy levels near the valence band provide additional recombination path (1.495 eV) for photoexcited carriers, e.g. conduction-band–acceptor transition indicated in Fig. 2.1a as E_1 .

The information that can be acquired by photoluminescence measurements also depends on experimental techniques used to collect a PL signal, disperse it into different wavelengths, and record. The detailed description of various experimental techniques of luminescence spectroscopy and their operation principles can be found in the textbook by I. Pelant and J. Valenta [71]. The important characteristics of an experimental setup for PL measurements include the spectral range of the detector, the lowest detectable signal, and the spectral resolution that allows to distinguish between the closest emission energies [71].

Whereas it is relatively easy to acquire the PL spectra experimentally, the interpretation of PL data might be less straightforward. It might be difficult to distinguish between intrinsic PL properties expected for a semiconductor crystal under study and extrinsic PL properties, which arise from crystal structure defects, alloy composition fluctuation or inhomogeneity of impurities incorporation. The issue is especially complicated if several radiative recombination paths contribute simultaneously to the experimental PL spectrum.

2.1.2 Spectral imaging and diffraction limit

In order to determine the physical phenomena that arise from the spatial inhomogeneity of studied nanostructures, spatially-resolved imaging of their properties is applied. The term

of imaging can include various experimental techniques, such as optical microscopy, electron microscopy or scanning probe microscopy, which generally aim to resolve a vast amount of information on the micro- and nanometer length scales. These techniques allow to address experimentally local optical, structural or electronic properties of nanostructures.

Herein, the discussion is focused on optical means of imaging, particularly on the photoluminescence imaging. The combination of dispersive elements providing individual PL spectra with an imaging system allows an acquisition of a full PL spectrum at each pixel of the image. The resulting three dimensional data set can be considered either as a collection of images from the region of interest acquired at a single wavelength per image, or as a collection of individual PL spectra measured at different pixels of the image.

The information that can be extracted from such hyperspectral data cube depends on the quality of the acquired data. One of the most important characteristics is a spatial resolution of the image, which defines the smallest spacing between two features in the object that can be distinguished. The spatial resolution might depend on the signal quality, sampling frequency (the size of pixels), however, it is limited generally by the wave properties of light.

If spectral imaging is performed by conventional optical microscopy techniques, where the excitation light is focused on a small volume of a sample and the emission is collected from this spot by the same focusing optics, the spatial resolution is limited due to the diffraction of the light waves [71]. This means that both the smallest distance between two distinguishable emitting features on the sample and the minimum spot size of the focused excitation light are given by this diffraction limit. When using the lens with a finite aperture to image the point-like emission source, its image is formed by a system of diffraction rings, which are known as the Airy pattern. The criterion used to define the resolution limit of the optical system can be represented by the Rayleigh criterion [72]. Two point-like emitters imaged by a conventional microscopy techniques can be resolved if the centre of the one Airy disk lies at the first minimum of the second Airy disk, which gives the distance d_{min} as:

$$d_{min} = 0.61 \frac{\lambda}{NA}, \quad (2.1.1)$$

where λ is the emission wavelength, $NA = n \sin \alpha$ is the numerical aperture of the imaging optics with the half of its acceptance angle α , and n is the index of refraction. Therefore, the resolution limit for the sample features emitting at the wavelength of $\lambda = 820$ nm imaged by an objective lens with a numerical aperture NA close to the unity is about $d_{min} = 500$ nm. Taking into account imperfections and aberrations of optical elements, the smallest distance between two distinguishable emission centres might be even large, than theoretically suggested. The concept that allows to overcome the diffraction limit is introduced in the following paragraphs.

2.2 Introducing the near-field optics

2.2.1 Evanescent waves

In order to introduce the experimental technique that allows to overcome the diffraction limit, some theoretical basics of high-resolution optical microscopy are outlined. The concept of evanescent waves is essential to understand optical fields that are confined to subwavelength dimensions. Evanescent waves decay exponentially and hence do not propagate in a

medium. Optical fields can be described as a superposition of *plane* wave and *evanescent* wave solutions to Maxwell's equations. In the following paragraph, the angular spectrum representation of optical fields is considered in brief, providing a useful mathematical technique for their description [73]. The electric field \mathbf{E} is observed in a plane that is transversed to the propagation axis z . The angular spectrum representation of the electric field for arbitrary z is given by

$$\mathbf{E}(x, y, z) = \iint_{-\infty}^{\infty} \hat{\mathbf{E}}(k_x, k_y; 0) e^{i[k_x x + k_y y \pm k_z z]} dk_x dk_y, \quad (2.2.1)$$

where the longitudinal wavenumber k_z is a function of transverse k_x and k_y wavenumbers. These wavenumbers, also known as spatial frequencies, are related to each other as follows:

$$k_z \equiv \sqrt{(k^2 - (k_x^2 + k_y^2))}, \quad (2.2.2)$$

where k is determined as $k = (\omega/c)n$, c is the vacuum speed of light and n is the refractive index of a medium. Notice that k is entirely defined by the frequency of light ω and properties of the media n where it propagates. The refractive index n is a real and positive number in case of a purely dielectric medium with no losses. Therefore, for certain k_x and k_y values the wavenumber k_z can be either a real or imaginary quantity that gives two different characteristic solutions [73]:

$$e^{i[k_x x + k_y y]} e^{\pm i|k_z|z}, \quad k_x^2 + k_y^2 \leq k^2; \quad (2.2.3)$$

$$e^{i[k_x x + k_y y]} e^{-|k_z||z|}, \quad k_x^2 + k_y^2 > k^2. \quad (2.2.4)$$

In the former, the propagator $\exp(\pm i k_z z)$ is the oscillating function that gives the plane wave solutions in z for the wavenumber spectrum $k_x^2 + k_y^2 \leq k^2$. In the latter, the exponential factor $\exp(-|k_z|z)$ is an exponentially decaying function along the z -axis that provides evanescent wave solutions for the broad spectrum of $k_x^2 + k_y^2 > k^2$ [73]. Since the intensity of evanescent waves decays exponentially, they do not propagate and can be thus detected only in a close vicinity to their source, in a near-field region. This means that evanescence waves do not exist in a homogeneous medium and they occur due to the light interaction with such inhomogeneities as a plane interface [73]. The conventional optical microscopy operates in the far-field and hence detects only optical fields of propagating waves with restricted spectrum of k_x and k_y .

2.2.2 Spatial resolution

As shown above, a spectrum of wavenumbers k_x and k_y of propagating waves is limited in the far-field by the condition (2.2.3). A spatial resolution provided by an optical imaging system operating in the far-field is connected with the spectrum of wavenumbers Δk_{\parallel} [73]. The distance Δr_{\parallel} between two point emitters that can be resolved depends on the bandwidth of spatial frequencies $\Delta k_{\parallel} = (\Delta k_x^2 + \Delta k_y^2)^{1/2}$ collected by the imaging optics as follows:

$$\Delta k_{\parallel} \cdot \Delta r_{\parallel} \geq 1, \quad (2.2.5)$$

This means that two objects can be resolved better the larger the bandwidth of wavenumbers collected by the optical system is. However, with only propagating waves in a far-field

the maximum $\Delta k_{||}$ is defined by the wavenumber $k = (\omega/c)n = (2\pi/\lambda)n$ as discussed above. Thus, the minimum distance between two distinguishable objects in a far-field is limited by:

$$[\Delta r_{||}]_{min} = \frac{\lambda}{2\pi n}. \quad (2.2.6)$$

In practice, the spectrum of Δk existing in the far-field is not entirely sampled [73]. Since the optical system has a finite aperture, only waves propagating within a specific angle α are collected and contribute to the bandwidth of spatial frequencies:

$$[\Delta r_{||}]_{min} = \frac{\lambda}{2\pi n \sin \alpha} = \frac{\lambda}{2\pi NA}. \quad (2.2.7)$$

This is the best theoretically suggested resolution that can be achieved with far-field waves. Similarly to the Rayleigh's criterion it depends mainly on the wavelength of light even though suggest a better resolution. However, the imperfections of optical elements, such as lenses and mirrors, additionally reduce the resolving power of far-field optical techniques. Therefore, the resolution power of conventional optical microscopy is restricted by both the fundamental diffraction limit of the light and the performance of optical elements.

To increase the bandwidth of the wavenumber spectrum $\Delta k_{||}$, the inclusion of $k_x^2 + k_y^2 > k^2$ is necessary. This requires to collect the evanescent waves, which exist only near the object plane. Therefore, the experimental concepts of the near-field optics that allow to include the evanescent waves to the imaging process are considered in the following section.

2.2.3 Near-field scanning optical microscopy

As it was previously mentioned, the conventional optical microscopy operates with light in a far-field region. This means that on the way from a sample to a detector evanescent waves completely vanish, and the associated wavenumbers k_x and k_y are not included in the spectrum of detected spatial frequencies [73]. This leads to the diffraction limit of the light and, consequently, restricts the ability to resolve local emission features of nanostructures. The goal of near-field optical microscopy is to improve the spatial resolution of an imaging system by collecting evanescent waves and thereby increasing the spectrum of spatial frequencies [73].

The principle of the near-field optical microscope can be considered in analogy with the far-field confocal microscope, schematically shown in Figure 2.2a [73]. The general idea of confocal microscopy is based on the selected far-field illumination of the sample through the high-numerical-aperture microscope lens, which provides a highly focused excitation light, and the selected far-field detection. This means that, the collected far-field signal originating away from the focal volume is filtered out by the detection pinhole (Fig. 2.2a). In order to reconstruct the image of the whole area of interest, the microscope lens is raster-scanned along the surface of the sample. At each step (pixel), a full spectral information is collected and then plotted as a function of the pixels coordinates. The spatial resolution is defined by the spatial confinement of the light flux through the object plane [73]. The higher the numerical aperture NA of microscope lenses is, the broader the spectrum of spatial frequencies $\Delta k_{||}$ is, and hence a better confined light flux is provided. However, using propagating plane waves, the spectrum of spatial frequencies is still limited by $k = 2\pi n/\lambda$.

To overcome the diffraction limit and increase the confinement of the light flux, evanescent waves have to be included in the imaging concept represented in Figure 2.2a. Since evanescent waves occur at the interfaces only and rapidly decay, the source of evanescent

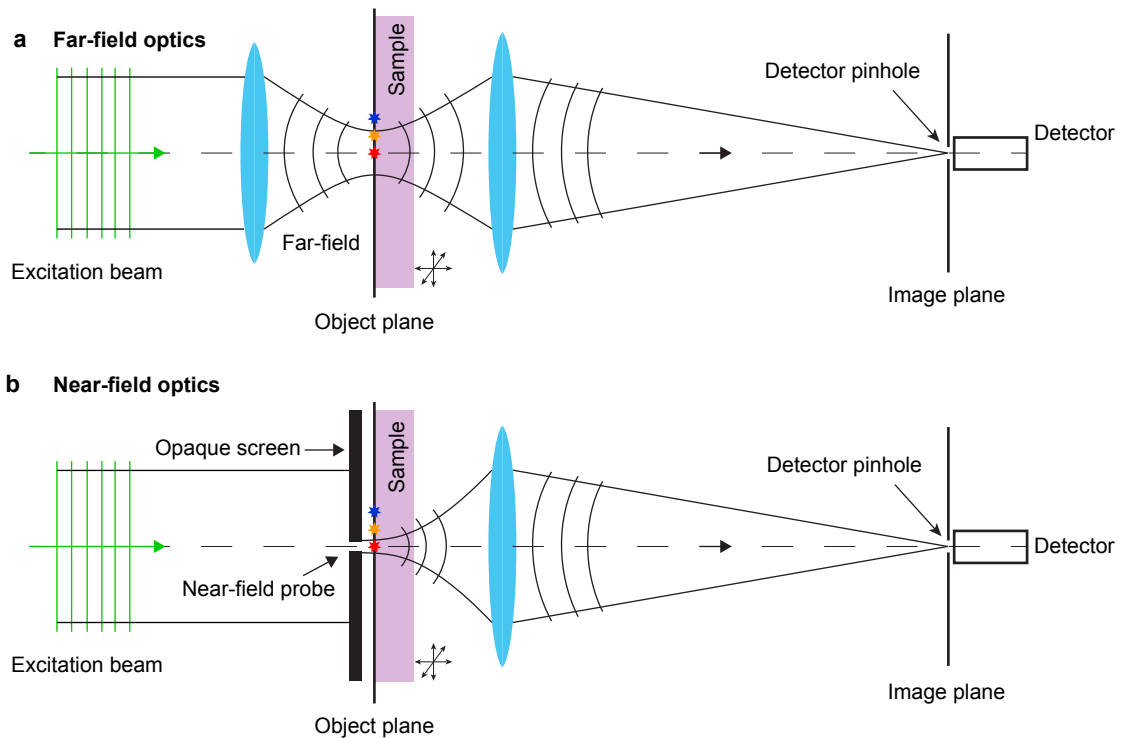


Figure 2.2: a) Far-field confocal microscope. b) Near-field optical microscope that allows to include spatial frequencies beyond $k = 2\pi n/\lambda$. Herein, a subwavelength aperture in a metal plate is used as the near-field probe. Adapted from [73].

waves has to be placed close to the sample surface. Particularly, this distance has to be much smaller than the working wavelength λ . For instance, a sample can be illuminated through a subwavelength aperture in an opaque metal screen placed in a close proximity to a sample surface ($\ll \lambda$), since the broad spectrum of spatial frequencies is only available near the aperture (Fig. 2.2a) [73]. Importantly, highly confined fields spread out and decay very rapidly along the optical axis [73]. Then, the emission from the locally excited area is collected from the back side, and the entire image of a sample is reconstructed in the same way as described above. However, the resolution of the imaging system is defined now by the size of the aperture and its distance from a sample surface rather than by the wavelength of light.

The idea to use a subwavelength aperture in a metal plate as the local probe and thereby to overcome the diffraction limit was initially suggested by Edward Hutchinson Synge in 1928 [74]. As it is often the case, this novel idea was suggested far before the technical implementation became possible such as a distance control between the local probe and the sample surface. The first subwavelength imaging was demonstrated in 1972 using 10 cm waves [75]. The sub-diffraction-limited resolution at optical frequencies became possible at the early 1980s with a rapid development of scanning probe microscopy that allowed for the precise probe-sample distance control. As a result, the first practical implementation of the near-field concept in the optical region was demonstrated by D.W. Pohl *et al.* [76] and independently by A. Lewis *et al.* [77] in 1984. In the work [76], the metal-coated tapered optical fiber was used as a near-field probe in order to deliver a highly confined optical

field with high spatial frequencies to the sample [76]. Nowadays, tapered optical fibers are widely used for scattering evanescent waves to a far-field. There are various configurations that allow the measurement of the near-field. In Figure 2.3, different schemes of excitation and detection of a photoluminescence signal in a fiber-based near-field scanning optical microscope are demonstrated. The selection of one of these configurations is defined mainly by the trade-off between the spatial resolution and the signal-to-noise ratio, i.e. a minimum emission intensity that can be detected. The main goal of these approaches is to provide a highly confined light flux between probe and sample as well as to find a compromise between light confinement and light throughput. In summary, the fiber-based near-field scanning optical microscope is considered as a powerful technique for a nanoscale characterisation of various photonic and optoelectronic materials [78–80].

However, this is only a part of the near-field optics. The phenomena related to the so-called *optical antenna* are not considered here, since they are out of the scope of this work. The detailed overview of the theoretical and experimental concepts of the nano-optics can be found in the book of L. Novotny and B. Hecht [73].

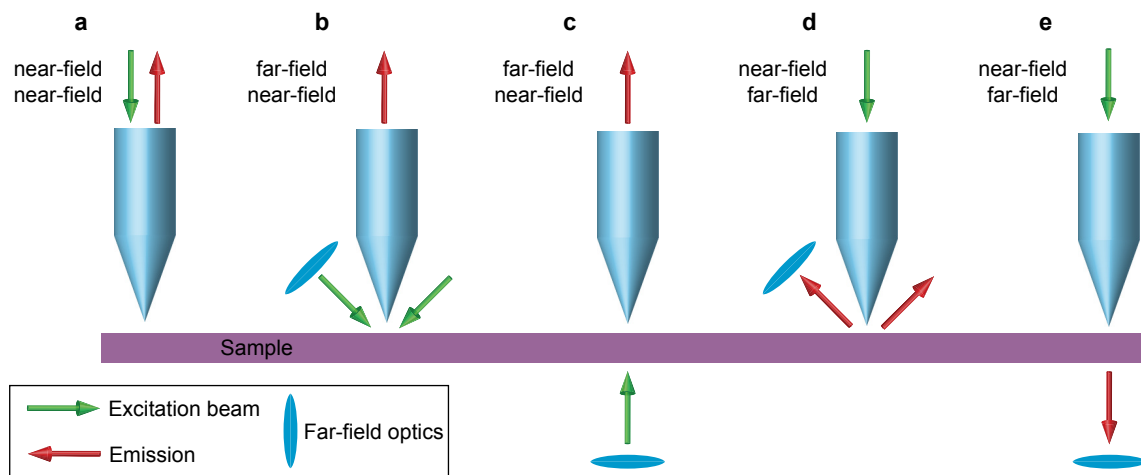


Figure 2.3: Overview of possible configurations of a fiber-based near-field scanning optical microscope: a) Near-field illumination of a sample and near-field collection of a signal by the same near-field probe. b) Far-field illumination and near-field collection. c) Variation of (b) for a transparent sample. d) Near-field illumination and collection by a far-field optics. e) Variation of (d) for a transparent sample.

2.3 Installation of the microscope

In this work, spectral imaging of crystal-phase heterostructures in GaAs nanowires is carried out using a fiber-based near-field scanning optical microscope. The microscope is a home-build system that, in contrast to typical commercial analogs, provides a number of possibilities for the customisation of its elements for dedicated applications. This includes selection of an excitation wavelength, a detection energy range, a type of the optical fiber and the near-field probe, different illumination-collection configurations (Fig. 2.3), optical measurements under the influence of external fields, and some others. The investigation of optoelectronic properties of semiconductor structures often requires to perform optical

measurements at low (cryogenic) temperatures. This allows to avoid the influence of thermally activated electronic transitions as well as improves the photoluminescence yield. The important advantage of the microscope applied in this work is the ability to perform the subwavelength resolution near-field spectral imaging at cryogenic temperatures. In contrast to low-temperature near-field scanning optical microscope concepts reported by other groups [81–83], in the microscope used here the sample can be cooled down to cryogenic temperatures while leaving the temperature of all other mechanical components close to the room temperature [84]. The original microscope design was reported in the work of G. Behme *et al.* [84]. The main components of the home-built near-field scanning optical microscope used in this work were constructed and assembled in the *Ultrafast Nano-Optics Group* at the *Carl von Ossietzky University* in Oldenburg. Afterwards, the installation of the setup, the customisation of its components and the first test measurements at cryogenic temperatures were performed within this work.

2.3.1 Microscope layout

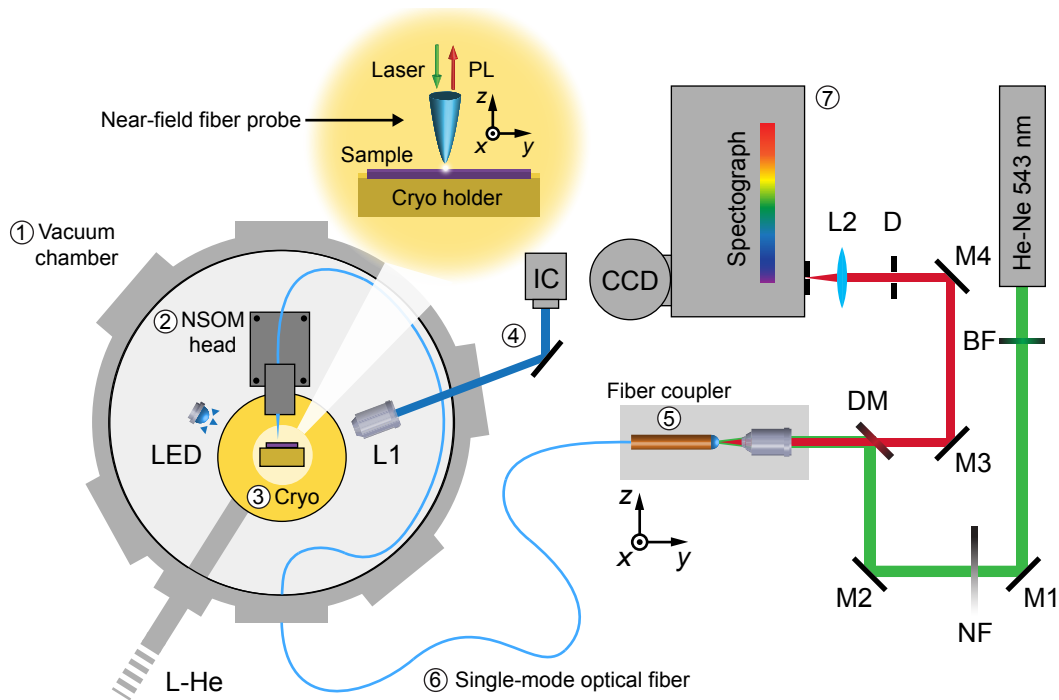


Figure 2.4: Layout of the low-temperature NSOM setup (top-view). The NSOM head, compact helium flow cryostat with a sample, and optics for coarse positioning of the tip are installed inside a high vacuum chamber. Inset: NSOM is operated in the near-field illumination and the near-field collection mode using a tapered uncoated single-mode optical fiber as a near-field probe. See Table 2.1 for abbreviations.

In Figure 2.4, the layout of the home-built near-field scanning optical microscope (NSOM) operating at variable temperatures is presented. The main components used for near-field spectral imaging are installed inside a high vacuum chamber (1). The NSOM-head (2) consists of a near-field fiber probe and a tuning fork shear-force distance control system, which is synchronised with the piezoelectric actuators for x - y - z fine positioning of the probe with

respect to the sample [84]. These components are installed on three motorised translation stages for x - y - z coarse positioning of the probe [84]. The distance control system is considered in detail in next sections. The sample is mounted on a cryo-holder (3) (“cold finger”) of a compact continuous flow helium cryostat and can be cooled down and measured at a temperature range from 8 to 330 K [84]. For the visual inspection of the probe-sample region, a long working distance $20\times$ microscope objective (L1) with a 0.35 numerical aperture is used. It collects the reflected light from the sample, which is illuminated with a light emitting diode (LED) [84]. These components of the NSOM are installed inside the high vacuum chamber, as shown in Figure 2.5. The light is then detected through an optical window by a charge coupled device camera (IC) (4), which is installed outside of the vacuum chamber (Fig. 2.4). Such design allows the *in vacuo* probe-sample alignment and the selection of a region of interest for measurements [84]. All components of the setup are installed on the optical table from Newport equipped with pneumatic isolators that ensure the mechanical stability and vibrations damping during measurements.

Table 2.1: Abbreviations of equipment in Figure 2.4

Abbreviation	Element description
BF	Bandpass filter, 540 ± 2 nm Center, 10 ± 2 nm FWHM
M1	Broadband dielectric mirror
NF	Linear variable neutral density filter, 0.04 to 4.0
M2	Broadband dielectric mirror
DM	Dichroic cold mirror
Cryo	Compact continuous flow cryostat
L-He	Liquid helium supply
LED	Light-emitting diode, tip coarse positioning optics
L1	Microscope objective, $20\times$, NA=0.35
IC	Inspection camera, tip coarse positioning optics
M3	Broadband dielectric mirror
M4	Broadband dielectric mirror
D	Iris diaphragm
L2	Aspheric lens, $f=100$ mm
CCD	LN-cooled charge-coupled device camera, 800-1700 nm

For the excitation of the sample, a helium-neon (He-Ne) continuous-wave laser at the wavelength of 543 nm is used. The laser light (Fig. 2.4, green) is transmitted by means of mirrors through a linear variable neutral density filter (NF), for a fine variation of excitation power density, and coupled into a single mode optical fiber. For this purpose, a selected optical fiber is mounted to a home-made fiber coupler (5), which is installed on a commercial fiber coupler stage from Newport. The optical fiber (6) is glued into the vacuum chamber and connected with a near-field fiber probe at the NSOM-head (Fig. 2.4 and Fig. 2.5b). The near-field probe used in this work is an uncoated tapered single mode optical fiber (Fig. 2.4, inset). The type of the optical fiber is specified later in the section related to a near-field probe preparation. Such uncoated near-field fiber probes combine a spatial optical resolution of about $\lambda/4$ to $\lambda/6$ [80, 85] of the working wavelength with a high collection efficiency and minimum perturbation of optical properties of a semiconductor nanostructure. It is

assumed that the near-field probe delivers an optical field with a broad spectrum of spatial frequencies to a sample and collects spectral information that contains a broad spectrum of spatial frequencies, thereby, providing a high spatial resolution. In this work, two types of near-field fiber probes were used. Chemically etched uncoated fiber probes were prepared in our laboratories within this work. The etching method is described below. Commercial uncoated and metal-coated near-field fiber probes provided by Nanonics Imaging Ltd. were also integrated to our NSOM setup.

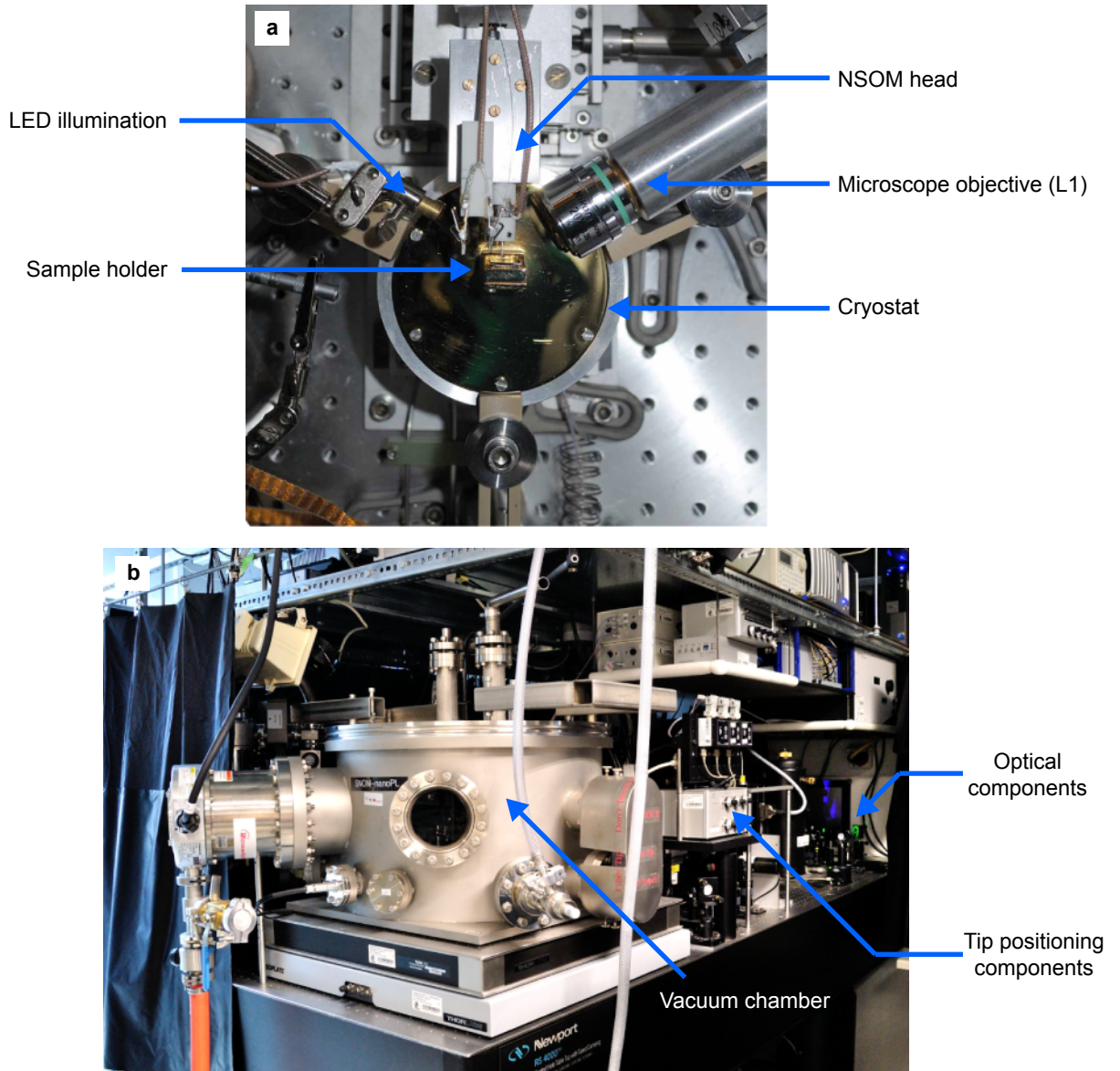


Figure 2.5: (a) Picture of the NSOM-head inside the high vacuum chamber as schematically shown in Fig. 2.4. (b) Picture of the home-built NSOM system operating at cryogenic temperatures.

All measurements were performed in a near-field illumination-collection mode (Fig. 2.4, inset) that provides the best spatial resolution for such type of probes and sufficient signal-to-noise ratio. The PL signal is collected through the same near-field fiber probe, and then

transmitted via an optical fiber and a set of mirrors and lenses to a detector (7). To remove the reflected laser beam from the emitted light, a dichroic cold mirror (DM) is used. The PL signal is dispersed in an imaging monochromator and recored with a liquid nitrogen-cooled InGaAs charge coupled device (CCD) camera operating in the spectral range from 800 to 1700 nm. The current home-built NSOM system and components of the microscope, which were installed inside the vacuum chamber, are shown in the photograph in Figure 2.5.

2.3.2 Near-field fiber probes

A key component of an NSOM setup is a near-field probe, which can serve as a near-field illuminator or a near-field collector, or both. In this work, a tapered conical single mode optical fiber is used for a near-field illumination of the sample and a collection of the photoluminescence signal. An advantage of the fiber probes is the flexibility to select an optimal optical fiber for particular applications in visible and near infrared spectral regions and their high throughput due to the waveguide structure. There are several basic methods to prepare tapered optical fibers, such as a heating and a pulling [86], a meniscus-etching [87,88], a tube-etching [89,90], and a hybrid selective etching [91,92]. Principles of some of these methods are briefly outlined further. A particular attention is given to the approach based on a chemical etching.

For the pulling of the optical fiber a CO₂ laser is normally used [86]. The laser pulse of a few milliseconds is focused onto the fiber, and the pulling starts subsequently after the

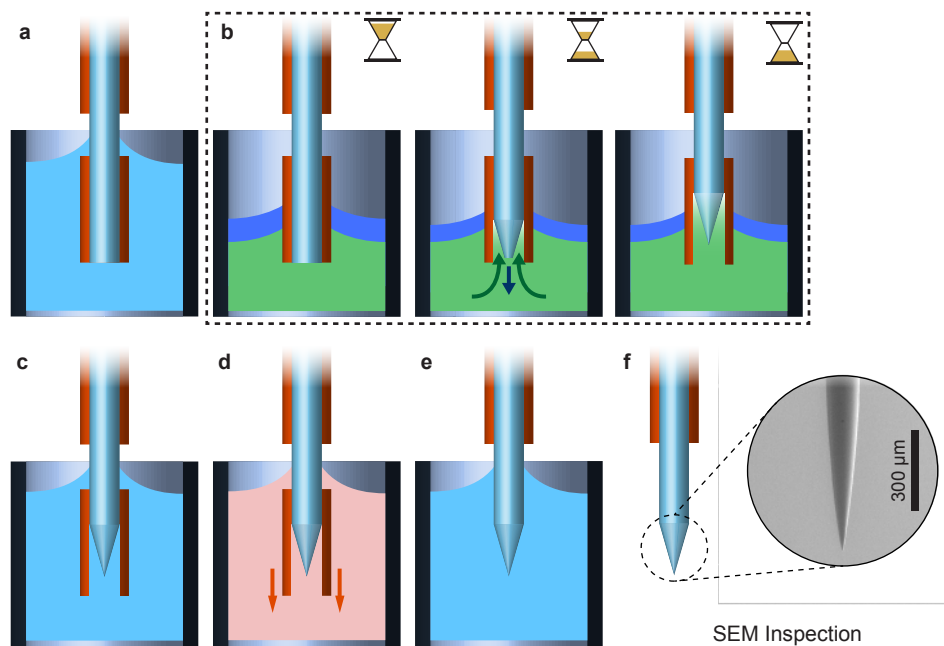


Figure 2.6: Illustration of the tube-etching process. a) The coating is cleaved about 1 cm above the end of the fiber and the fiber is cleaned in ethanol. b) – d) The fiber is dipped in 40% HF solution (green) covered with isoctane protection layer (dark blue). The etching time is varying from 30 minutes to 5 hours, depending on the fiber type. e) Etched fiber is cleaned from residuals in ethanol. f) The plastic coating is softened in dichloromethane and removed. g), i) The tapered fiber is cleaned again in ethanol and inspected by SEM.

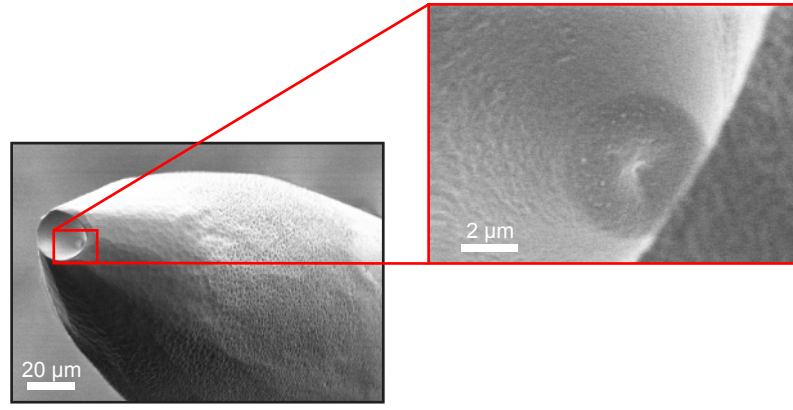


Figure 2.7: SEM micrographs with different magnification of the single mode optical fiber from Fibercore etched by tube-etching method.

laser pulse with a defined velocity profile [86]. This method allows to produce fiber probes with smooth surfaces that facilitate a high quality of metal coating. The weakness of this method is a relatively small solid angle of resulting near-field probes, which is typically of about 10° . This leads to a leakage of optical field through the sides of uncoated probes or a low throughput in case of metal-coated probes, which limit their performance [73].

A method for a fabrication of near-field fiber probes used in this work is a so-called *tube-etching*. The method is based on the etching of optical fibers in a 40 % hydrogen fluoride (HF) solution without removing of their plastic coating [89,90]. In Figure 2.6, the successive steps of the tube-etching method are schematically shown. The optical fiber is etched inside its plastic coating, which has to be removed after the etching procedure without damaging a tapered part. To this end, the plastic coating is cleaved about 1 cm from the end of the fiber as shown in Figure 2.6a. Prior to the etching, the prepared fiber is cleaned from contaminations in ethanol (Fig. 2.6a). The 40% HF solution is filled into a Teflon vessel and covered with isooctane (*2,2,4-Trimethylpentane*) layer, as shown in Fig. 2.6b. The isooctane overlayer prevents a fast evaporation of the HF solution and protect the upper part of the fiber and a holder from the corrosive HF vapour. The optical fiber is dipped into HF solution for about 1 mm. The fiber is tapered due to microconvection inside the tube formed by its plastic coating, which is chemically stable against HF. A faster removal of chemical reaction products and the excess of acid ions at the lower part of the tube results in gradient of the dissolution rate inside the tube and the subsequent tapering. The etching time can vary from 30 minutes to 5 hours, depending on the fiber type (Fig. 2.6b-d). Then, the fiber probe is cleaned from residuals in ethanol. The plastic coating is softened in dichloromethane (*Methylene chloride*) and slips off into the solution without damaging the tip (Fig. 2.6f). Afterwards, the fiber probe is cleaned again in ethanol and the quality of the probe is inspected with a scanning electron microscope (SEM).

Different types of optical fibers for operation in the near-infrared region were tested. It was observed, that the quality of the tip, e.g. surface roughness, solid angle, tip diameter etc., depends on the fiber rather than etching parameters, such as an HF concentration or a temperature. As an example, the tube-etching of two different fibers under similar etching conditions is discussed.

In Figure 2.7, the tube-etching of single-mode optical fibers from Fibercore (SM980,

operating wavelength 980 nm, inner core diameter $5.8 \mu\text{m}$) is shown. The fiber was etched in a 40 % HF solution for 90 minutes at a room temperature. For this type of the fiber, etching in HF solution leads to the hollowing instead of tapering of the probe, which is typical for a silica fiber with germanosilicate (GeO_2)-doped core and a pure silica cladding [93]. This can be qualitatively explained by the ratio of the dissolution rates of the core and cladding. Evidently, the dissolution rate of the core for presented fiber type is larger, than that of the cladding. In order to achieve a tapered fiber, the ratio of the dissolution rates for such fibers has to be changed by the selective etching, e.g. in a buffered hydrogen fluoride solution. Details of the selective etching are comprehensively described in the work done by M. Ohtsu [93].

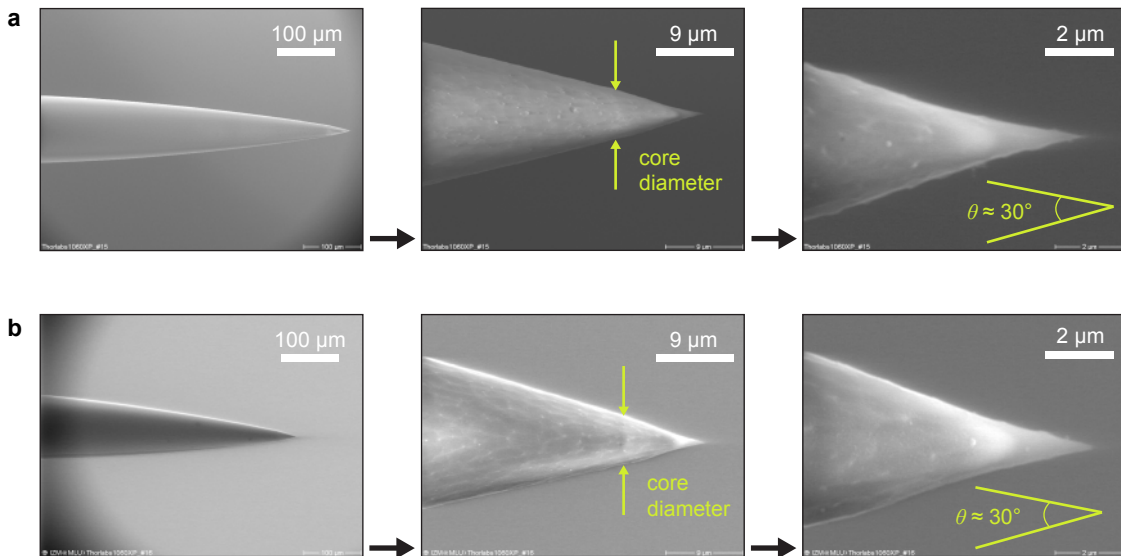


Figure 2.8: SEM micrographs with different magnification of the single mode optical fiber from Thorlabs (1060XP) etched by tube-etching method.

A single-mode optical fiber from Thorlabs (1060XP, operating wavelength 980–1060 nm, inner core diameter $5.8 \mu\text{m}$) has demonstrated the most promising results of etching in 40 % HF solution. For testing, 15 probes were prepared from the selected optical fiber. The optimum probe shape is achieved at etching times of about 4–5 h. The shorter time results in an incompletely removed long thinned part at the end of the tip. An average solid angle θ of the etched fibers is about 25° – 30° . Fiber tips with a smooth surface and a small apex diameter ($\sim 100 \text{ nm}$) are well reproducible. In Fig 2.8, a representative near-field probe prepared by the tube-etching from the Thorlabs-1060XP fiber is presented.

2.3.3 Distance control setup

In order to conduct near-field spectral imaging, the tapered optical fiber used as a near-field probe has to be brought to a close proximity to the sample surface, where evanescent waves can be included to the image formation. Moreover, it is essential to keep the probe-sample distance constant during the scan process to avoid artefacts in an optical response [94]. As it was previously discussed, this distance between a near-field probe and a sample surface is required to be smaller than the confinement of the light flux. Herein, to keep the near-field

probe in constant and close proximity to the sample during the scan process and avoid a collision with the surface, a shear-force distance control technique is applied [73, 95]. The principle of this method is based on the fact that the vibration of a probe (e.g. tapered fiber) parallel to the sample surface is affected by the proximity of the sample [73]. In comparison to laser-based techniques of the distance control, e.g. commonly used in atomic force microscopy [96], this non-optical method allows to avoid undesired background light in the collected signal.

The practical implementation of the shear-force distance control technique is schematically illustrated in Figure 2.9. The prepared tapered optical fiber is glued onto one of the prongs of a quartz tuning fork. The tuning fork is connected to a ceramic piezoelectric tube (dither piezo), which serves to excite the mechanical oscillations of the fork at its resonance frequency. This construction is placed then on top of the piezoelectric actuator. The standard quartz tuning fork has a resonance frequency of 32.768 kHz, which is slightly shifted when the probe is mounted. The piezoelectric signal, generated by mechanical oscillations of the tuning-fork prongs, is then picked up from two contacts on the fork and measured using a lock-in amplifier. This signal has a maximum value at resonance free oscillations of the tuning-fork (far away from the sample surface). As the near-field probe approaches the sample surface, the amplitude of piezoelectric signal, measured at resonance frequency, decreases due to the tip-sample interaction. The feedback loop consisting of proportional-integral-derivative (PID) controller and approach gain controller of a piezoelectric actuator allows to place the near-field probe from 0 to 25 nm above the sample surface by setting the desired amplitude at the resonance frequency (Fig. 2.9). The analysis of the shear-force mechanism can be found in the original work of K. Karrai and R. D. Grober [95].

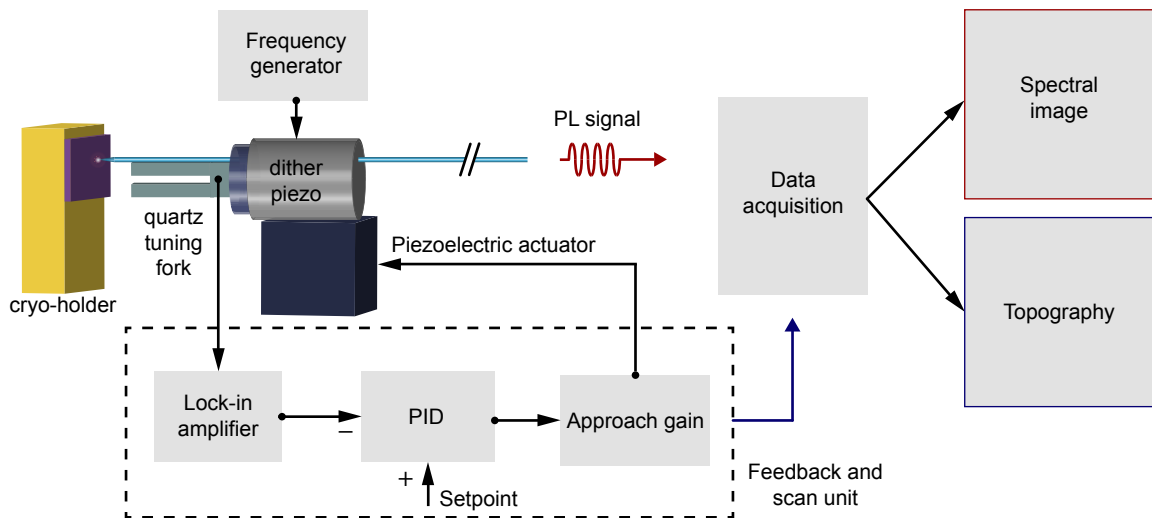


Figure 2.9: Schematic of shear-force distance control setup.

The shear-force distance control system allows thereby to approach a probe to the near-field region and performing a scan of the sample surface in a constant-gap mode, which ensures the absence of artificial changes in the optical signal such as an intensity variation related to the probe-sample distance fluctuations. In addition, a read out of a displacement of the near-field probe perpendicular to the sample surface provides information about topographical features of the sample (Fig. 2.9). A combination of the high-spatially resolved

spectral information and the topographical image of an object acquired within the same scan may substantially improve interpretation of experimental data.

2.4 Test measurements of single nano-objects

Having discussed the operation principles and design of the home-build NSOM system as well as characteristics of its essential elements, the capabilities of the microscope to image local photoluminescence of individual nanostructures are considered in the following sections. For this purpose, samples with semiconductor quantum dots are selected as reference nano-objects for a near-field photoluminescence study at cryogenic temperatures. Measurements by NSOM provide spectrally and spatially resolved information about the photoluminescence emission that allows to address optical properties of individual quantum dots. The sub-diffraction-limited spatial resolution and high signal-to-noise ratio of the detected signal are demonstrated. In addition to the purpose of evaluation of the NSOM capabilities, results of test measurements allow an improved understanding of the optical quality of this type of quantum dots, as it is reported in [97].

2.4.1 InAs quantum dots grown in nanoholes on GaAs surface

The reference nano-objects selected for test measurements are InAs semiconductor quantum dots (QDs) grown in GaAs nanoholes. The sample with QDs was grown and prepared by Yu-Ying Hu from *Ruhr-Universität Bochum* in the department of Prof. Dr. A. D. Wieck. Semiconductor QDs attract a particular interest due to their unique properties resulting from a three-dimensional confinement of the carrier wave function, which occurs when the characteristic size of nanostructures approaches an electron wavelength [98]. Such confinement of carriers leads to the formation of localised states in conduction and valence bands. The confinement potential limits the number of localised states, defines the transition energies, and, in turn, strongly depends on the composition of heterostructure materials and QDs morphology. This provides possibilities to tailor the energy band structure of QDs for device applications or for exploring their fundamental properties. The detailed analysis of phenomena associated with the discrete nature of QDs energy band structure is, however, out of the scope of this work and can be found in various reviews and textbooks [98–101].

The fabrication of size- and site-selected QDs is a longstanding technological issue and a critical requirement for their application in various devices, e.g. as a source of entangled photon pairs for quantum information processing [102]. Here, QDs provided by *Ruhr-Universität Bochum* are fabricated by a combination of a droplet epitaxy technique [103, 104] and self-assembled Stranski-Krastanow (SK) growth [105]. In general, the droplet epitaxy allows to produce QDs on lattice matched materials such as GaAs/Al_xGa_{1-x}As. First, gallium (Ga) material is deposited on the substrate. It forms metal droplets on its surface minimising thereby the energy of the system. Then, the arsenic (As) flux is introduced to initiate the crystallisation of the Ga droplets and GaAs QDs formation [103, 104]. However, at certain substrate temperature and/or As flux pressure, the same technique applied on the GaAs surface leads to nanoholes instead of islands formation [106]. Interestingly, these nanoholes can be used then as predominant nucleation centres for SK growth of InAs QDs. The density of nanoholes and their size is defined largely by Ga metal droplets, which can be controlled by growth conditions. Thus, the combination of SK growth and droplet epitaxy technique allows to reduce the density of QDs up to 10⁷ cm⁻² [107] and gain an additional control over

their size. However, such QDs are still randomly distributed on the surface. To overcome this issue and facilitate a site-selected growth, an *in-situ* focused ion beam (FIB) patterning of the GaAs surface prior to droplet epitaxy and SK growth is proposed in the work of Yu-Ying Hu [97]. As a result, the spatial distribution of nanoholes is governed by FIB-patterning that facilitates the formation of InAs QDs in an ordered array.

Even though, the described fabrication steps provide possibilities to control structural parameters and the distribution of QDs, they may also introduce undesired side effects, such as impurities or defects, which will necessarily influence the optical properties of nanostructures. Therefore, the correlation studies between structural properties (fabrication steps) and the optical quality of such QDs is essential. In order to address the optical properties of individual QDs and verify capabilities of the NSOM system, the low-temperature near-field spectral imaging is applied. For NSOM measurements, two types of QD ensembles are prepared: (i) QDs grown in randomly-distributed nanoholes on GaAs surface, i.e. without FIB-patterning, (ii) site-selected QDs generated in the arrayed nanoholes positioned on the FIB-patterned areas [97].

2.4.2 Spectral imaging of single quantum dots

Randomly-distributed quantum dots

First, InAs QDs fabricated in randomly-distributed nanoholes on the bare GaAs surface without FIB-patterning are studied. The sample is attached to a cryo-holder and cooled down to 10K to increase the photoluminescence yield and avoid thermally activated effects. A continuous wave (cw) He-Ne laser at 543 nm, i.e. 2.283 eV, is used for optical excitation of the luminescence. The laser light is coupled into an uncoated, single-mode chemically etched near-field fiber probe providing a laser power in the fiber of ~ 13 nW. The excitation intensity can be gradually varied using a linear variable neutral density filter. The PL signal is collected by the same fiber in the near-field illumination-collection geometry, which typically provides a spatial resolution of about $\lambda/4$ to $\lambda/6$ of the working wavelength. The spatial resolution estimated for QDs measured here is about 300 nm at the emission wavelength near 1070 nm. This may arise from the thick ~ 70 – 80 nm cap layer deposited above the emission centres. The collected PL signal is guided to an imaging monochromator with an entrance slit width of 150 μm , dispersed and recorded with the nitrogen-cooled InGaAs CCD camera. A grating with 150 lines/mm and a blaze wavelength of 800 nm is used as a dispersing element. To construct a map of PL signal in the region of interest, the near-field probe is raster scanned across the sample area of $4.8 \times 4.8 \mu\text{m}^2$ with a step size of 80 nm. At every step, a full PL spectrum is collected in the energy range of 1.02 to 1.40 eV using an integration time of 1 second per spectrum. The integration time and excitation laser power were selected to obtain an optimum signal-to-noise ratio and a convenient mapping time of about 90 minutes.

In Figure 2.10a, a two-dimensional map of total PL intensity of the area without FIB-patterning is presented. At every pixel, a PL spectrum is integrated over the energy range of 1.10 to 1.30 eV, in which all PL peaks are observed. The values of integrated PL intensity for every spectra are then plotted as a function of near-field probe position. A colour-code corresponds to resulting values that are normalised to unity within the scan area. In Figure 2.10a, about 20 clearly resolved single local emission centres are seen. They show the similar size and integrated PL intensity. Importantly, the density of observed emission centres is about $9 \times 10^7 \text{ cm}^{-2}$, which is in a good agreement with the density of

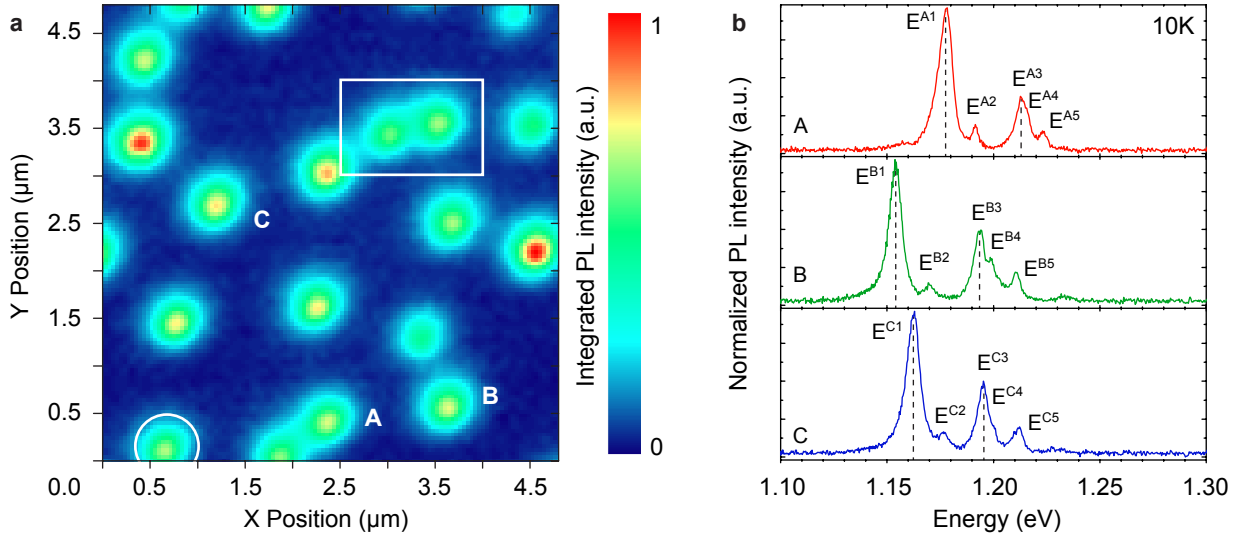


Figure 2.10: (a) Two-dimensional near-field map of total PL intensity, i.e. spectrally integrated for every pixel and normalised to unity within the scan area. The PL signal is collected by a raster scan of the near-field probe over the region of $4.8 \times 4.8 \mu\text{m}^2$ with a step length of 80 nm. The full PL spectrum is collected at every step and integrated then within the energy range of 1.10 to 1.30 eV. A colour-code corresponds to resulting values of integrated PL intensity. A white circle indicates a single QD selected for the power dependence measurement of its individual PL spectrum (Fig. 2.11). A white rectangle shows two QDs separated by a distance of about 500 nm, which PL spectra are analysed in Figure 2.12. (b) Representative local PL spectra are selected from another QDs marked by **A**, **B**, and **C** on (a).

nanoholes prepared by droplet epitaxy on GaAs surface ($7 \times 10^7 \text{ cm}^{-2}$ [97]). This result supports the predominant nucleation of InAs QDs in GaAs nanoholes and the tentative assignment of individual emission centres to photoluminescence from single QDs. Moreover, the correspondence between the density of emission centres and nanoholes suggests that most QDs are optically active. Representative local PL spectra from QDs marked by capital letters A, B, and C in Figure 2.10a are shown in Figure 2.10b. Several PL bands are resolved within each spectrum. Remarkably, the number of PL peaks, spectral separation and their relative intensities are comparable among selected spectra (Fig. 2.10b). This indicates the origin of photoluminescence from nano-objects with similar structure of energy levels.

In order to analyse energy levels of a single nano-object, the near-field probe was accurately positioned in the area of the QD shown in Figure 2.10a (white circle). Thereafter, the local photoluminescence was measured as a function of excitation power, which is controlled by a linear variable neutral density filter mounted on a mechanical actuator from Thorlabs (see Fig. 2.4). The excitation power in optical fiber was gradually varied from 4 to 268 nW. As shown in Figure 2.11, at a low excitation power only one PL peak at the energy of about 1.176 eV is clearly resolved. The intensity of this peak gradually increases with the increase of the excitation power. This PL transition is assigned thereby to the lowest ground-state E_{00} recombination in a single QD [97]. The increase of the excitation intensity leads to a slight red-shift of E_{00} peak (Fig. 2.11), which can be explained by the appearance of additional multiexcitonic lines at the low-energy side of E_{00} [108, 109].

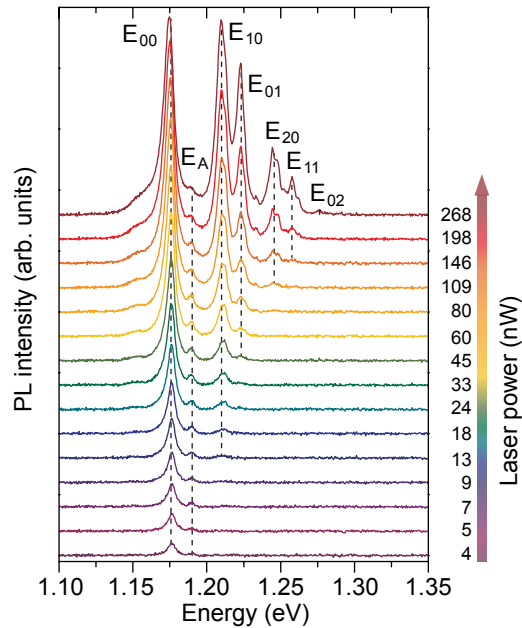


Figure 2.11: Power dependence of the local near-field PL spectrum recorded from the single QD marked by the white circle in Figure 2.10. The fiber probe is constantly positioned in the area of selected QD during power dependence measurements. The excitation power of the He-Ne laser is varied by calibrated a linear variable neutral density filter from 4 to 268 nW, measured previously at the end of the optical fiber.

In addition, the appearance of high-energy PL peaks at a higher excitation power is observed, which corresponds to saturation of lower electronic transitions and population of excited states. To assign PL peaks to certain electronic transitions within a single QD, near-field photoluminescence spectra were correlated with morphology of QDs studied in the work of Yu-Ying Hu [97]. It was observed that the diameter of nanoholes along the $[0\bar{1}1]$ direction is slightly larger than their diameter along the $[011]$ axis. This suggests that the corresponding QDs have the elliptical base with characteristic radii r_x and r_y along the $[0\bar{1}1]$ and $[011]$ directions, respectively. Thus, the anisotropic lateral QD confinement can be approximated with two parabolic potentials along x and y directions, as it was previously reported by Heyn *et al.* [110]. Thereby, the PL peaks in Figure 2.11 can be approximated by optical transitions between electron and holes from states with identical quantum numbers n_x and n_y in the form $E_{n_x n_y} = E_{00} + n_x \hbar \omega_x + n_y \hbar \omega_y$, where ω_x and ω_y denote the oscillator frequencies of two parabolic potentials [110]. The equidistant quantisation energies $\hbar \omega_x$ and $\hbar \omega_y$ in two parabolic potentials were found to be 35 meV and 47 meV, respectively [97]. In Figure 2.11, new PL peaks in near-field spectra appear at energies, which correspond to these quantisation energies as indicated by dashed lines, and found thereby to be in a good agreement with the approach of two parabolic potentials. The PL spectra of other QDs in Figure 2.10a can be also well described by this approach. An additional small peak marked as E_A is found near the ground-state transition E_{00} (Fig. 2.11). This peak likely originates from the optical recombination between ground-state electrons and holes from the second excited state [97, 109].

The spectrally integrated image, such as shown in Figure 2.10a, reveals the spatial distribution of all emission centres, which can be resolved with a given near-field probe and

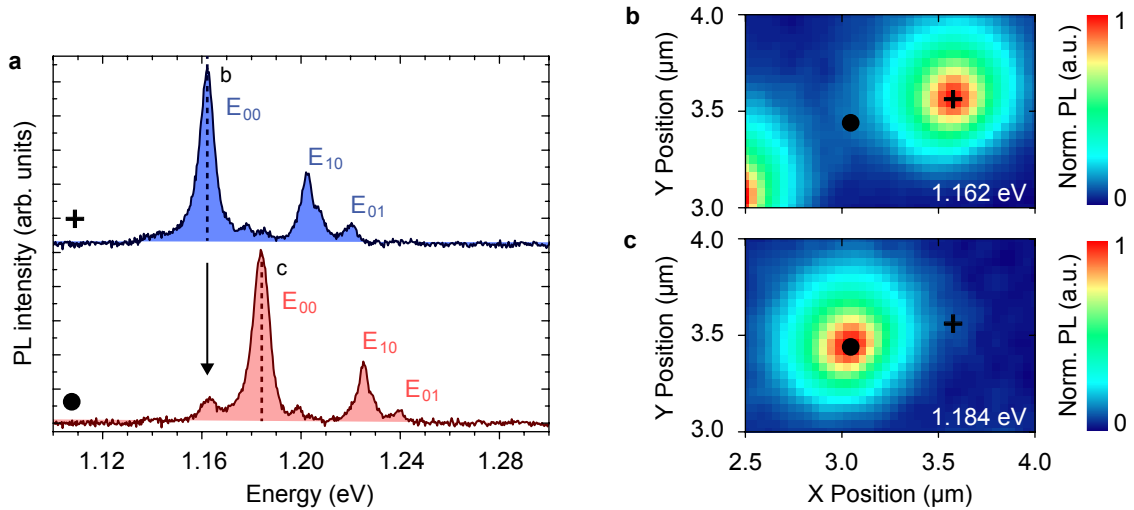


Figure 2.12: Two-dimensional spatial images of the local PL intensity of two single QDs from the region marked by the white rectangle in Figure 2.10: (a) and (b) plotted at detection energies of 1.162 eV and 1.184 eV, respectively. (c) Representative local PL spectra from positions marked by the black cross and the close circle. Dashed lines show energies of most intensive PL bands for each QD, which correspond to ground state transitions E_{00} .

experimental parameters. However, a distinction between the nearest emission centres and the assignment of spectral features to individual QDs can be substantially improved by the analysis of emission maps at characteristic energies. For instance, the region marked by a white rectangle in Figure 2.10a comprises two emission centres, which are separated by a distance of about 500 nm. Their representative local near-field PL spectra selected from the pixels with maximum PL intensity are shown in Figure 2.12a. The observed series of emission lines reflect recombination from different energy levels of these QDs. To assign these emission lines to certain localised states within each QD, it is first necessary to determine their spatial origin, namely to distinguish between two QDs. For this purpose, the PL intensity distribution at energies 1.162 and 1.184 eV related to the most intensive lines in both spectra, respectively, are plotted in Figure 2.12b,c. The intensity maps at selected energies clearly reveals maxima at different locations. This enables now for some additional spectral lines around the main maxima (Fig. 2.12a, black arrow) to be identified as emission originating from adjacent QDs, which are sampled during near-field measurements due to the finite spatial resolution. Thus, the small low-energy peak in the bottom panel in Figure 2.12a (red) is related to another QD with its spectrum shown in the top panel (blue), as indicated by the black arrow. The analysis of the spatial intensity distribution of all emission lines may then provide information about the fine structure of the nano-objects.

Site-selected quantum dots

Although the described InAs QDs prepared by droplet epitaxy and SK growth demonstrate high optical quality, they are still randomly distributed on the surface. To obtain an ordered array of QDs, the FIB-patterning technique was applied [97]. Even though this additional fabrication step is expected to provide ordered arrays of QDs, ions that impinge on the sample surface might lead to such defects as surface amorphization, crystal structure defect

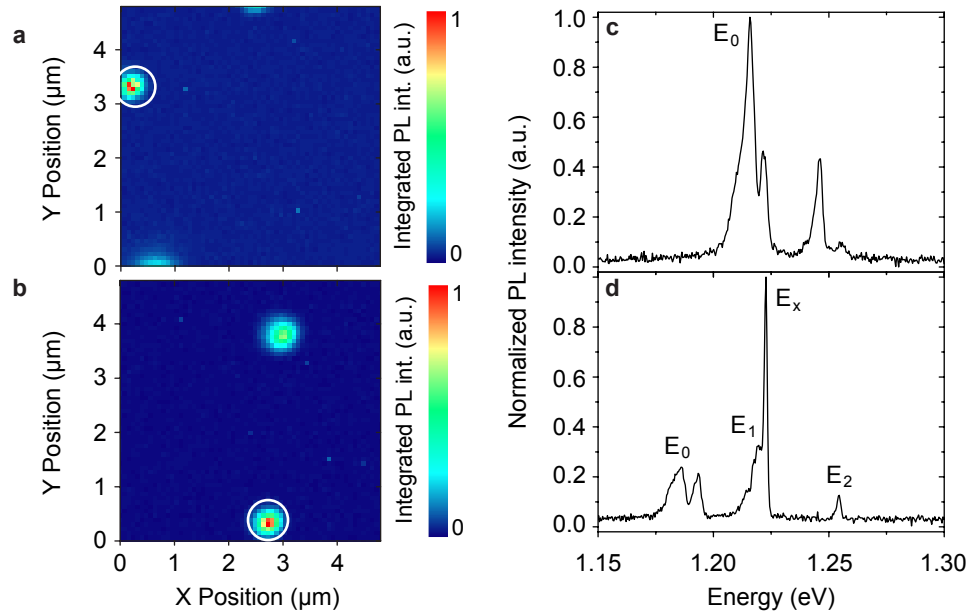


Figure 2.13: Two-dimensional near-field images of maximum PL intensity at every pixel, normalised to unity within the scan area: (a) area on the sample with 1 μm pitch between FIB spots, patterned using an ion beam of 1×10^6 ions/spot fluence, (b) area on the sample with 2 μm pitch between FIB spots, patterned using an ion beam of 3×10^5 ions/spot fluence. (c),(d) Representative local PL spectra selected from QD areas marked by white circles on (a) and (b), respectively.

formation and ion implantation. Thereby, this may strongly influence the quality of GaAs substrate and hence the optical properties of InAs QDs. Thus, the near-field spectral imaging by our NSOM system was applied to address the optical properties of individual QDs grown on FIB-patterned GaAs surface.

In Figure 2.13(a,b), the results of NSOM imaging of two sample areas patterned with an ion beam fluence of (a) 1×10^6 and (b) 3×10^5 ions/spot and inter-spot distances of 1 and 2 μm , respectively, are presented¹. Here, the maximum value of the PL intensity at every pixel is plotted as a function of the near-field probe position. As shown, only a few emission centres are observed. The PL signal localisation is comparable with that observed for the un-patterned GaAs surface presented in Figure 2.10a. However, the spacing between QDs in the optical map is about 2 to 3 times larger, than those defined by the FIB-patterning. An SEM examination of the sample confirms nucleation of QDs in ordered nanoholes with a high degree of probability [97]. Thus, the NSOM imaging indicates that some fraction of these QDs may not be optically active or the emission from such QDs is weak. This observation can be qualitatively explained by taking into account the influence of FIB-patterning. The FIB-induced defects might play the role of non-radiative recombination centres and carrier traps in the surrounding GaAs matrix.

In Figures 2.13c and 2.13d the corresponding local PL spectra of individual QDs marked by white circles in corresponding Figures 2.13a and 2.13b are shown. Presented PL spectra consist of several emission lines of a different intensity ratio. The full width at half max-

¹For details of the fabrication process and parameters, see [97].

imum (FWHM) of emission lines is about 6–8 meV, which is comparable with InAs QDs grown on an un-patterned GaAs surface. The assignment of these emission bands is less straightforward as it was for previously discussed QDs and requires consideration of FIB-induced effects. QDs fabricated on the FIB-patterned surfaces are expected to have rather isotropic confinements, than described above [97]. Low-energy peaks are tentatively assigned to the ground-state transitions E_0 . In Figure 2.13d, the equidistantly separated PL peaks $E_1=1.219$ eV and $E_2=1.254$ eV can be assigned to the next two excited states by following the single parabolic potential approximation [97]. However, the occurrence of the sharp emission line E_x with FWHM less than 2 meV in the spectrum suggests to consider alternative recombination scenarios, e.g. due to the formation of QD pairs in GaAs nanoholes [80, 97]. Clearly, an additional investigation of this type of QDs is required in order to unambiguously assign the observed electronic transitions, which is beyond the scope of this work.

2.4.3 Conclusion

Summarising the results of low-temperature near-field measurements of InAs QDs grown in nanoholes on the GaAs surface, the NSOM technique provides a powerful tool to image single nano-objects and probe their optical properties with a high spatial and spectral resolution at cryogenic temperatures. The density of InAs QDs formed in randomly distributed nanoholes on the GaAs surface is consistent with that of local emission centres imaged by NSOM. This allows to assign these emission centres to individual QDs, which preferably nucleate inside nanoholes, and confirm high optical quality of the resulting heterostructure QDs. By combining excitation power dependence measurements of the single QD with the structural analysis, which indicates the anisotropy of QDs along $[0\bar{1}1]$ and $[011]$ directions, the assignment of detected emissions bands of individual QDs to certain quantum confinement states was proposed applying a model of the anisotropic lateral confinement [97]. For InAs QDs grown inside ordered nanoholes formed on the FIB patterned GaAs surface, the NSOM analysis suggests a strong effect of the FIB technique on resulting optical properties of QDs. Particularly, only part of such QDs is optically active, and hence the assignment of emission bands is less straightforward. Presented NSOM results substantially support the study of individual InAs QDs fabricated by the novel approach [97] and demonstrate the high-precision capabilities of the home-build microscope to address the local optical properties of individual nanostructures.

Chapter 3

Experimental protocol for the nanoscale study of single nanowires

3.1 Introduction

In III–V semiconductor nanowires, many exciting physical phenomena are determined by the spatial inhomogeneity of the crystal structure and material composition at the nanometer length scale. As it was previously discussed, the current understanding of the relationship between morphology and optoelectronic properties of individual crystal-phase heterostructures in single nanowires is still incomplete. Structural parameters of nanowires are highly inhomogeneous within the same growth batch. The investigation of nanowire ensembles provides at most the information about predominant optical and structural properties. Therefore, an accurate determination of structure-property relationships requires the application of single-nanowire measurements. The main method widely used to correlate optical and structural properties is a combination of micro-photoluminescence (μ -PL) and transmission electron microscopy (TEM) measurements performed on the same single nanowires [22, 60, 111, 112]. In previous studies, this method was successfully applied to probe local photoluminescence spectra and the crystal structure information of individual nanowires [22, 60, 111, 112]. However, the diffraction-limited spatial resolution of the μ -PL spectral imaging (the smallest laser spot diameter is $\sim 0.8 \mu\text{m}$ [22]) reduces the overall resolution of the structure-property correlation technique. Such limiting factor induces uncertainties on the attribution of optical transitions to a particular crystal structure and hence on the interpretation of experimental data. This also hinders the use of experimental data for modelling of the electronic band structure and quantum confinement effects in crystal-phase heterostructures. Alternatively, spectral imaging by cathodoluminescence (CL) spectroscopy can provide the sub-wavelength spatial resolution of different optical properties at different locations in the wire [25, 64, 113, 114]. Recently, an attempt to directly correlate the spatially resolved spectral characteristics with the crystal structure of nanowires by applying the CL-TEM strategy was made [114]. So far, results of correlated studies were mostly based on the demonstration of the correspondence of the average emission energy shift of PL spectra to the predominate crystal structure in nanowires [64]. However, the assignment of individual emission lines to the local crystal structure is required. In addition, the variation of experimental parameters, model structures, or substrates for single-nanowire measurements may cause the inconsistency in experimental results of different studies. Therefore, an advanced procedure providing a direct nanoscale correlation of high spectrally and spatially resolved local optical properties with particular

crystal structures of the very same nanowire within the same experimental cycle has to be established. For this purpose, the previously described custom-made NSOM technique is successfully integrated with the experimental routine of the crystal structure characterisation. This approach is aimed to provide better insights into the structure-property relationships in individual III–V semiconductor nanowires in general and GaAs nanowires in particular.

3.2 Overview of the protocol

In this chapter, an experimental protocol (hereafter referred to as a protocol) outlines a procedure for sub-wavelength resolution NSOM spectral imaging of local regions in individual nanowires and a subsequent structural characterisation of the *same* regions by an atomically resolved TEM analysis. In the present study, the protocol is applied for the investigation of GaAs nanowires, although it can generally be applied to a large variety of semiconductor nanostructures. The protocol describes how to prepare a sample for multiple single-nanowire measurements, extract nanowires after spectral imaging for the structural characterisation and conduct data acquisition and correlation. In Figure 3.1, a flowchart of the protocol indicates the major steps of the procedure and their sequence.

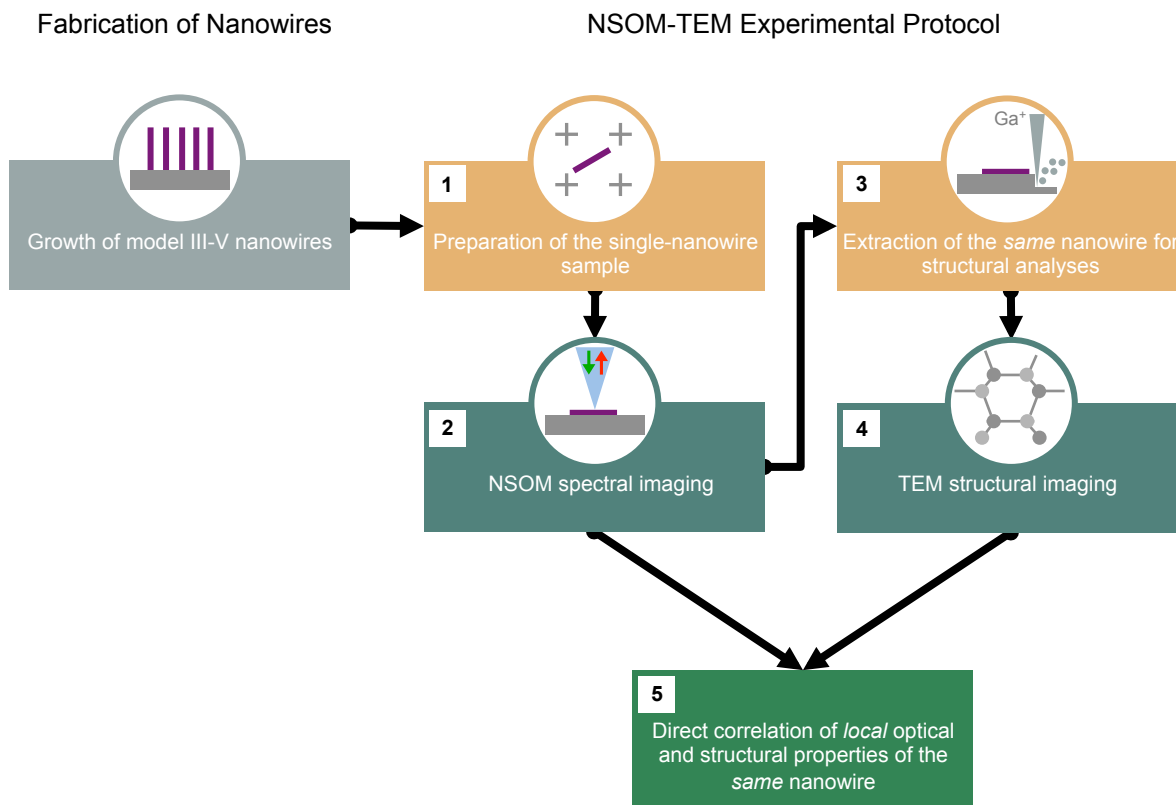


Figure 3.1: Flowchart of the protocol for the measurement and the direct nanoscale correlation of local optical properties and crystal structure of individual nanowires.

The protocol starts with the preparation of individual nanowires from the as-grown sample and their identification for multiple measurements (Step 1). At first, selected nanowires

are studied optically (Step 2) to exclude possible perturbations of photoluminescence spectra induced by other characterisation techniques. In the next step, the same nanowires are extracted from the substrate used for NSOM optical measurements and prepared by the focused ion beam technique (Step 3) for TEM analysis (Step 4). Finally, high-spatially resolved local optical and structural properties of the same nanowires extracted from experimental data can be directly correlated (Step 5). In the following, each step of the protocol includes a brief description of instruments applied for measurements. At the end of this chapter, limitations of the protocol as well as possibilities to further advance the acquisition and the correlation of optical and structural properties of individual nanowires are outlined.

3.3 Procedure

3.3.1 Sample preparation for the single-nanowire measurements

III–V semiconductor nanowires are typically grown by the vapour-liquid-solid growth mechanism using molecular-beam epitaxy (MBE) or metalorganic chemical vapour deposition (MOCVD) techniques. To perform single-nanowire measurements, free-standing wires have to be transferred from the growth substrate to an external holder facilitating both optical measurements and structural analysis. In previous studies, TEM holey carbon Cu grids [22] and SiN membranes [60,111] were used for this purpose. Here, silicon substrates are selected as a support material, which has an emission spectrum not interfering with that of nanowires under study. Si substrates were also applied as a support for single nanowire optical measurements performed by other authors [11]. In contrast to TEM holey carbon-coated Cu grids, a flat silicon surface ensures a stable contact of the nanowire with the substrate and a good thermal dissipation during optical measurements. The silicon substrate also excludes additional preparation steps such as a gold film deposition used to fix the nanowires on silicon nitride membranes [111], which could alter the optical properties of nanowires.

The preparation of the single-nanowire sample is schematically illustrated in Figure 3.2a. First, an external substrate that allows an identification of the same nanowire for multiple optical measurements and subsequent structural analysis has to be prepared. To select nanowires, store their coordinates and identify the same nanowires for various measurements, the external Si substrate is patterned with alignment marks. The square array of Au alignment marks with an equidistant spacing of $25\ \mu\text{m}$ was structured on Si surface by electron-beam lithography (Fig. 3.2a (2)). These alignment marks have a “+”-shape and every twentieth cross, i.e. every $500\ \mu\text{m}$ of the grid, is numbered respectively. At the next step, free-standing nanowires have to be transferred from the growth substrate to the pre-patterned Si substrate. The ultra-sonication technique is used to detach the nanowires from the original substrate. Then, the drop-casting technique is applied to disperse them on the pre-patterned Si substrate. For this purpose, a part of the growth substrate with nanowires of an approximate size of $5\times 5\ \text{mm}^2$ is immersed into the ethanol solution of 1–2 ml in a small glass beaker. Ethanol is selected for this procedure according to previous studies [58,115], although a mixture of ethanol and toluene or an isopropanol solution are also reported as appropriate chemical environments for sonication of GaAs nanowires [116,117]. Then, the beaker is placed into the bath of the ultra-sonic cleaner and sonicated for about 5 to 30 s. Finally, a droplet of 10–20 μl of ethanol containing the suspended nanowires is taken from the solution and drop-casted onto the pre-patterned Si substrate (Fig. 3.2a (3)). Once the ethanol solution evaporates (Fig. 3.2a (4)), the nanowire sample is preliminary inspected

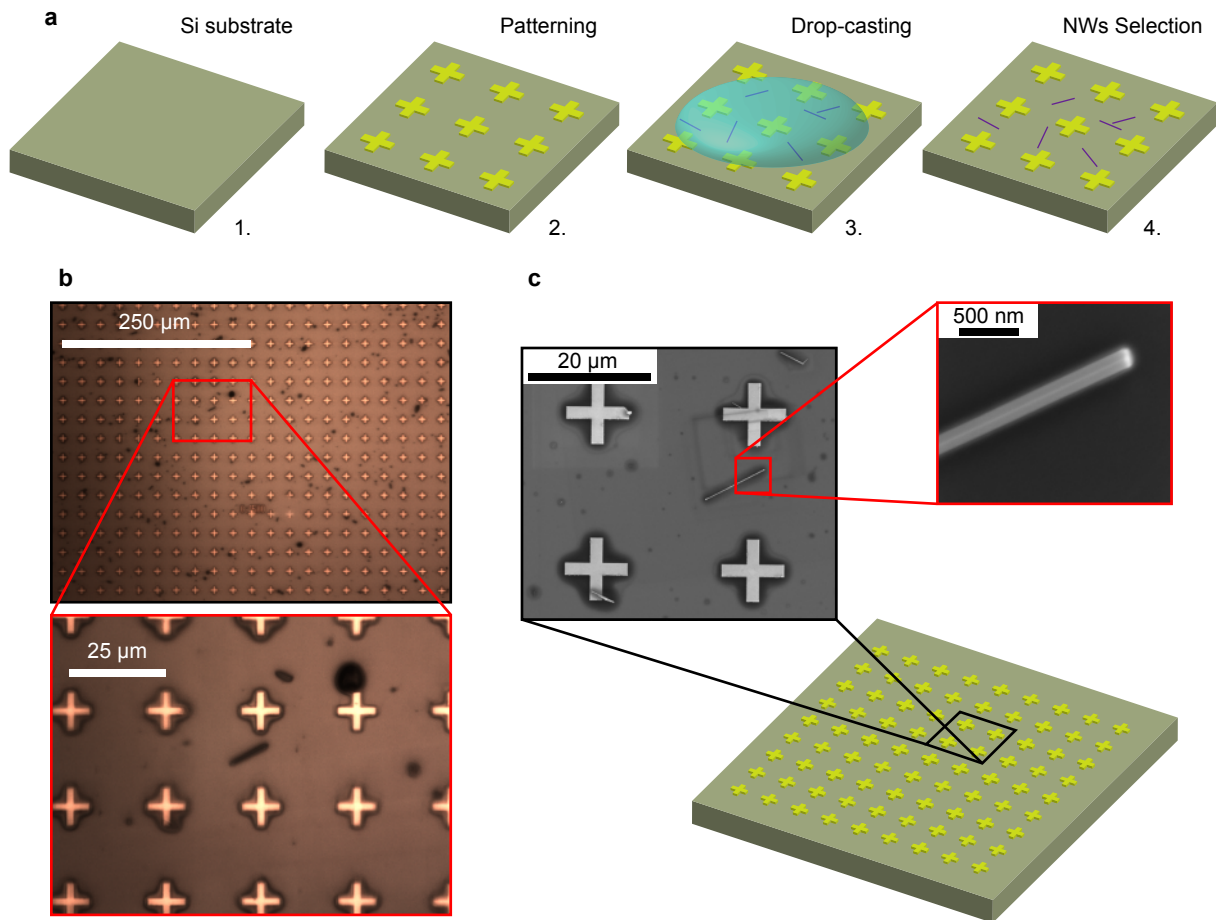


Figure 3.2: Preparation of a sample for correlated optical and structural analysis of individual nanowires. (a) Flowchart of the process: 1. Selection of an external substrate; 2. Deposition of Au alignment marks to form a grid with coordinates; 3. Drop-casting of nanowires suspended in an ethanol solution; 4. Evaporation of the ethanol solution and subsequent inspection by optical microscope. (b) Conventional optical microscopy image of the external substrate surface with a grid of alignment marks and the selected nanowire. (c) SEM inspection of some nanowires at low acceleration voltage of 5 kV and current of 0.4 nA.

with an optical microscope (Fig. 3.2b). Even though in the present study we rely on the precise high-spatial-resolution investigation of every single nanowire, rather than statistical analysis of predominant effects, several nanowires of similar length and diameter are generally selected to fulfill the requirements of data reliability. These nanowires are well isolated from each other and any objects on the surface to exclude possible interactions. The bonding of nanowires to the Si surface via van der Waals interactions is strong enough to insure their constant position during the whole experimental cycle [11]. Some nanowires are also inspected by scanning electron microscopy (SEM) to obtain the high-resolution information about their morphology as well as the surrounding surface to exclude other sources of photoluminescence (Fig. 3.2c). To prevent damage by an electron beam, the acceleration voltage of 5 kV and a current of 0.4 nA are applied. In this step, promising nanowires are selected on the pre-patterned substrate. Their coordinates are stored to identify the same wires for various subsequent measurements.

3.3.2 Spectral imaging by near-field scanning optical microscope

The comprehensive analysis of nanowires is started with non-destructive optical measurements using the dedicated custom-made NSOM microscope. The operation principle of spectral imaging by the NSOM technique was already discussed in *Chapter 2*. After the full spectroscopic information of a single nanowire is acquired, the next step of the preparation of the same wire for structural analysis is initiated. Obviously, for a complete characterisation of nanoscale materials the analysis of the morphology, the crystal structure and the elemental composition in addition to the spectroscopic information is highly desired.

3.3.3 Extraction of nanowires for the structural characterisation

Following the NSOM measurements, the same nanowires that were studied optically have to be prepared for a characterisation by transmission electron microscopy. To this end, a commercial FEI dual-beam Nova Nanolab 600 SEM/FIB system is applied. As mentioned above, to ensure a stable contact between the nanowire and the surface, and a good thermal dissipation during optical measurements, the Si substrate is used. The FIB technique is applied to prepare a thin lamella of a constant thickness along the wire axis. This allows to acquire the structural information along the whole length of the wire. The FIB routine of a lamellae preparation, that is similar to the routine described in [118], is used to achieve a high positioning accuracy of the lamella regarding to the nanowire axis and provide a damage-free transfer of single nanowires onto a TEM holder. Importantly, such FIB nanomachining can be also applied for the fabrication of complex single-nanowire specimens, e.g. for the atom probe tomography [119]. Various sample preparation techniques for the TEM analysis can be found in the handbook by J. Ayache *et al.* [118].

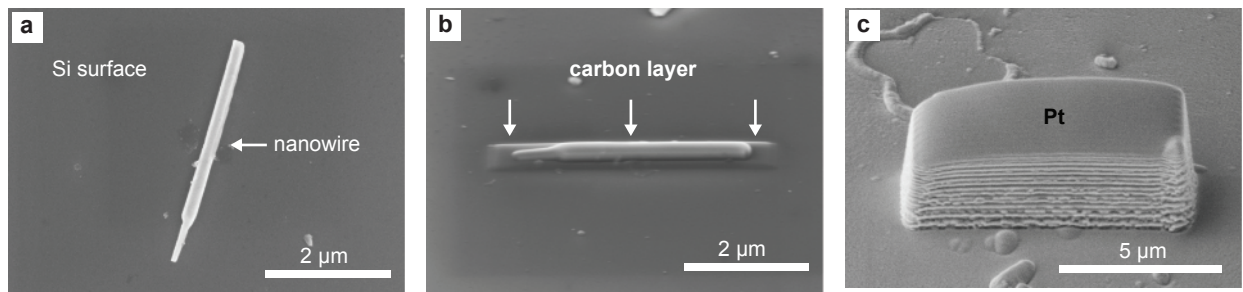


Figure 3.3: Scanning electron microscopy (SEM) micrographs: (a) Top-view of the nanowire transferred by ultra-sonication and drop-casting techniques onto the Si substrate. (b) Protection of the nanowire from damages during FIB preparation by coating it with carbon and platinum (Pt) layers. First layers are grown by the electron beam induced deposition at a low voltage of 5 kV. (c) Ion induced deposition of the platinum layer on the substrate area of $\sim 8.5 \times 3 \mu\text{m}^2$ containing the nanowire of interest. The final thickness of the Pt layer is approximately 4 μm.

The procedure starts with a growth of a few tens of nanometers of carbon in the target region by an electron beam induced deposition (Fig. 3.3). The carbon provides a good material contrast in SEM images. Therefore, it is used as a marker for the fine positioning of the lamella during the FIB target preparation. To protect the nanowire from damages induced by the ion milling, it is coated with platinum (Pt). Two types of Pt layers are

deposited by applying electron beam and then ion beam induced material depositions. In addition, these two Pt layers and the nanowire material also produce different contrasts in SEM images, which allows to control the location of the wire inside the lamella during the milling process. After the deposition of the protection layers, two trenches on both sides of

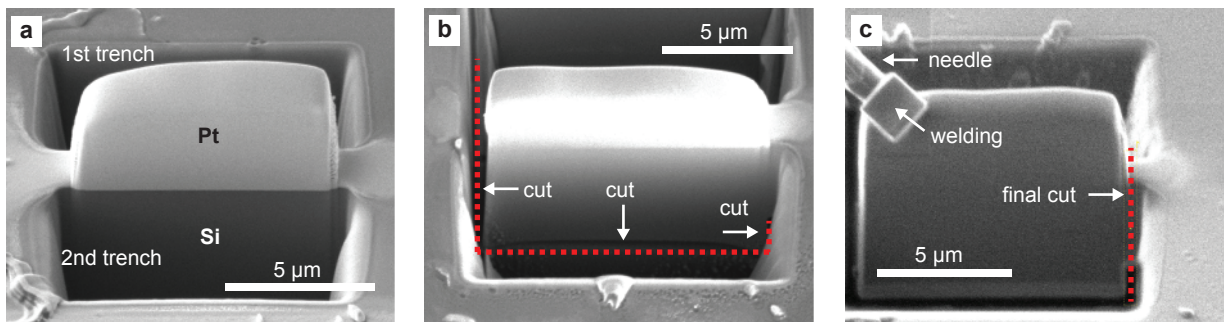


Figure 3.4: SEM micrographs: (a) Two trenches machined by ion milling on both sides of the area containing the nanowire of interest. (b) The lamella is partly cut using the ion beam. (c) Welding the lamella and the micro-manipulator (“needle”). The slice is completely detached from the Si substrate by the final cut.

the nanowire were formed by ion (Ga^+) milling at a high voltage (30 kV) and at a normal incidence of the ion beam to the substrate (Figure 3.4). These two trenches define the initial thickness of the slice that contains the nanowire of interest. The slice is undercut using the ion beam through the left side and the base, as shown in Figure 3.4b. The right side was partly cut, in order to hold the lamella in place for the following preparation stage. In the next stage, a needle-shaped micro-manipulator was approached to the sample and welded to the slice using the platinum source and the ion beam. After the slice is firmly connected to the micro-manipulator, it is finally cut out from the substrate (Fig. 3.4c).

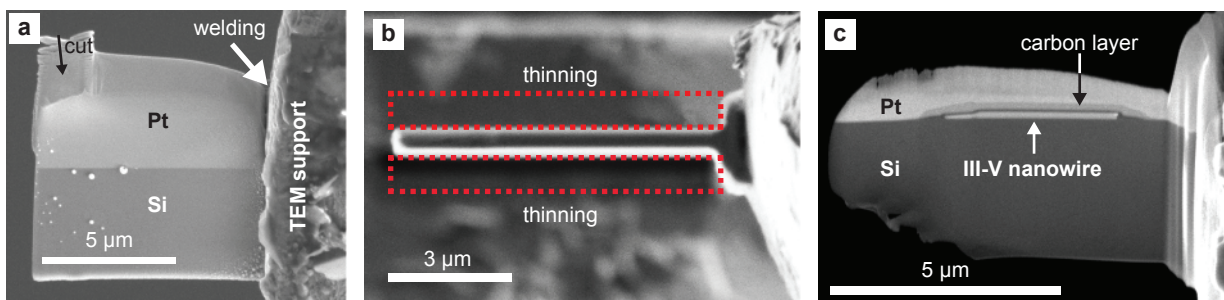


Figure 3.5: SEM micrographs: (a) Welding the lamella onto the TEM support. (b) Top-view of the thinned lamella. The area milled by the ion beam is depicted by red dashed lines. (c) The final thinned lamella. The clearly observed SEM material contrast indicates the position of the nanowire.

Then, the slice is extracted from the Si substrate and welded to a TEM compatible support. Afterwards, the micro manipulator was cut from the slice by ionic abrasion (Fig. 3.5a). To prepare the lamella for TEM measurements, both sides of the sample were alternately tilted to 1° with regard to the ion beam for a further thinning of the lamella. For this

purpose, an ion beam of 30 kV voltage and 100 pA current was applied (Fig. 3.5b). The exact position of the NW inside the lamella is controlled by the material contrast in *in situ* SEM micrographs. To remove the ion beam induced damage (surface roughness, amorphised layers etc.), the final target thinning was performed using a low energy ion beam (5 keV and 2 keV) at an incidence angle of about 4°. The thickness of the resulting lamella is approximately 80 nm (Fig. 3.5c). The nanowire is clearly seen inside the lamella due to the contrast in SEM images produced by different materials.

The nanowire prepared by this way allows to access the structural information as well as the material composition order along its entire length. Following the protocol (Fig. 3.1), the TEM support is mounted inside the transmission electron microscope for structural characterisation of the *same* nanowire which was measured optically earlier.

3.3.4 Characterisation of nanowires by electron microscopy

In the next step of the correlated analysis, the crystal structure and the elemental composition of nanowires complementing the high-spatially resolved spectroscopic data are measured by electron microscopy. For this purpose, various electron microscopy techniques are applied. To gain information about the nanowires morphology, stacking sequences of atomic planes and an arrangement of atoms with respect to each other, the ultimate spatial resolution is required. This is achieved using the wave nature of high energy, i.e. having a very short wavelength, electrons for imaging this specific information of nanowires [120]. For structural analysis, the lamella containing the nanowire of interest is mounted to the TEM-holder (see Step 3) and gently transferred from the FIB machine to the dedicated TEM. In this work, the crystal structure of nanowires is analysed applying two instruments: (i) FEI electron microscope TITAN 80-300 with the probe aberration corrector and the acceleration voltage up to 300 kV, (ii) JEOL JEM 4010 microscope with the acceleration voltage of 400 kV.

The interaction of electrons with a sample produces different types of signals. In Figure 3.6, a schematic of the electron-matter interaction indicates some of them [120]. Various types of electron microscopes, or various detectors within the same microscope, collect these signals to reconstruct the corresponding information. The direction of signals in Figure 3.6 is schematic, however it suggests the area where the signal is collected. In case of a thick specimen, secondary electrons and backscattered electrons emitted by the surface are typically used in a scanning electron microscopy (SEM) for imaging of the surface topography or the distribution of elements according to their atomic number [118]. In this work, nanowires are inspected by an SEM instrument integrated into the commercial FEI dual-beam Nova Nanolab 600 SEM/FIB system, which was also used for a sample preparation. The SEM measurements, which typically requires a minimal sample preparation, are applied to identify the same nanowires studied optically before to acquire accurate data about their diameter, length, or a surface quality. It also allows to inspect the surrounding area in order to exclude other emission sources. *In situ* SEM observation allows to control the FIB-preparation of lamellae containing the nanowire of interest for structural analysis.

In addition, the recombination of electron-hole pairs created by the electron beam leads to the emission of photons, which gives a cathodoluminescence signal. The energy of these photons provides a fingerprint of the recombination centres in a sample, e.g. band-to-band, impurities- or defects-related recombinations [25]. In analytical electron microscopes, which can provide information about the distribution of different elements in different regions, X-ray photons and Auger electrons are used for such chemical analysis. Some of these

measurements are also utilised in the current work to support the NSOM-TEM correlation and provide an additional information about the nanowires under study.

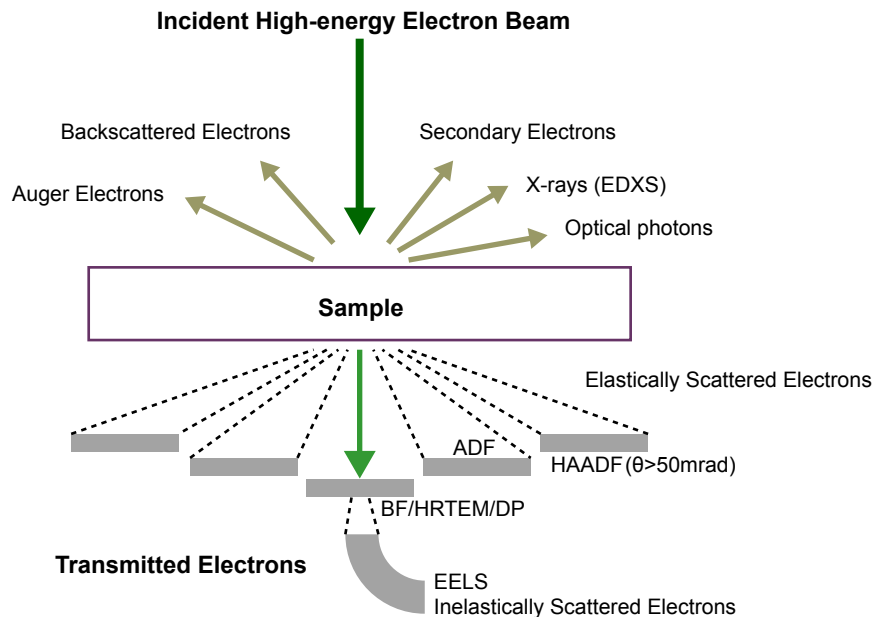


Figure 3.6: Different signals resulting from electron-matter interaction when a beam of high-energy electrons meets the sample. The schematic representation of each signal indicates where it is generally detected. Notations are provided in the text. Adapted from [120].

In case of a thin sample (≤ 100) and an electron beam of a high enough energy, electrons can pass through the sample experiencing an elastic and inelastic scattering or remain unscattered (lower portion of Fig. 3.6). Since the nanowires diameter is about 200 nm, they are already transparent for electrons of sufficient energy and, therefore, such samples require only a partial thinning for the high-resolution imaging. In the TEM measurements the acceleration voltage is about one or two orders of magnitude larger than the voltage in SEM. Similar to optical microscopy, where light can be focused or defocused for an image formation using glass lenses, the electron beam required for imaging in TEM is formed by electromagnetic lenses [120]. Even though the wavelength of high-energy electrons is very short, the achievable resolution is limited by an imperfection of electromagnetic lenses, such as spherical- and chromatic-aberrations and astigmatism [120].

In the conventional TEM mode, the incident electron beam is broad and parallel, which illuminates the complete region of interest. The parallel beam interacts with the nanowire, and the transmitted electrons are brought to a focus by the corresponding electromagnetic lens. Since semiconductor nanowires have highly periodic arrangements of atoms forming a symmetric crystal structure, electrons are diffracted according to the Bragg's law. The diffracted electrons are focused by the objective lens in the back focal plane forming a diffraction pattern (DP). The diffraction pattern can be used to identify the crystal structure of nanowires, when they are oriented in a crystallographic direction that allows to distinguish between ZB and WZ crystal phases. The diffraction pattern of a $\langle 110 \rangle$ oriented ZB GaAs nanowire measured with the JEOL JEM 4010 microscope is demonstrated in Figure 3.7a. The intensity distribution between different spots of the diffraction pattern provides information about the sample orientation, which is used to tilt the sample to the right viewing

direction. However, nanowire areas comprising a large number of stacking faults produce diffraction patterns, which can not be clearly assigned to the diffraction patterns of ZB or WZ inclusions and require an additional analysis, e.g. using high-resolution TEM images.

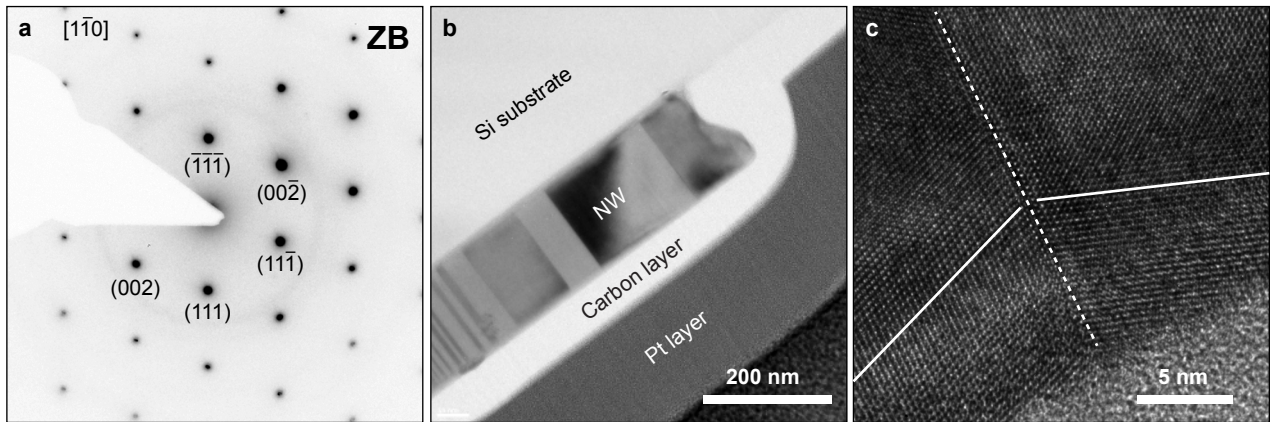


Figure 3.7: a) Diffraction pattern of the ZB segment of a GaAs nanowire along the $[1\bar{1}0]$ zone axis. b) Diffraction contrast TEM image of a GaAs nanowire acquired in the $\langle 110 \rangle$ crystallographic orientation. Bright and dark stripes in the image are produced by regions with different crystal orientation, crystal structure or planar faults such as stacking faults. c) HRTEM micrograph of the local crystal structure of a GaAs nanowire that demonstrates the interface (dashed line) between two rotationally twinned ZB segments. Bright spots in the image represent a projection of atomic columns along the $\langle 110 \rangle$ zone axis.

Another basic principle of the TEM operation is an image formation of a specimen. The contrast in TEM images results from the scattering of the incident beam by the sample. There are different mechanisms of the image formation based on the absorption contrast, the diffraction contrast, the phase contrast [121, 122], and the amplitude contrast, which is utilised in scanning transmission electron microscopy (STEM) [123]. Both the amplitude and the phase of the transmitted electrons contribute to the TEM image contrast of crystalline materials [120]. The variation of the amplitude can be produced by heavier elements or thicker areas of the sample, which scatter more electrons, and referred to as a mass-thickness contrast. If electrons that scattered to large angles are excluded from the image formation, the corresponding areas in the TEM micrograph will appear more dark. The second form of the amplitude contrast is a so-called diffraction contrast, which is generated by the crystal structure and the orientation of the specimen [120]. The diffraction contrast TEM images are generated by the similar mechanism, as described above. A small objective aperture is used to select only one reflection from the diffraction pattern. Therefore, only electrons that are scattered by sample areas in selected directions will contribute to the image and these areas will appear brighter. If the spot that formed by the direct-beam electrons (unscattered) is selected by the objective aperture, the resultant image is called a bright-field (BF) diffraction contrast TEM image. An image formed by the diffracted beam is referred to as a dark-field (DF) image [120]. In Figure 3.7b, the bright-field diffraction contrast TEM image of the nanowire, which contains areas with rotationally twinned zinc blende segments producing different electron diffraction conditions, is shown. The micrograph is acquired with the JEOL JEM 4010 microscope. The diffraction contrast TEM images provide information about morphology of nanowires, their crystal structure and the presence of crystal defects.

The difference in the phase of the electron waves scattered through the specimen also generates a contrast in TEM images. Especially, this effect dominates for electrons transmitted through a thin sample. It is used in a high-resolution TEM (HRTEM) to image the atomic structure. The so-called “phase contrast” is generated when the interference of several diffracted beams with the incident beam is used for the image formation [118]. Electrons gain a phase shift when pass close to an atomic nucleus, which temporarily cause a slight acceleration of these electrons. Therefore, electrons passing further away from the nucleus have a different phase. The example of HRTEM micrograph of the small area of a nanowire, which was measured with the TITAN 80-300 microscope, is demonstrated in Figure 3.7c. The HRTEM imaging provides information about the crystal structure and allows to acquire the lattice resolved micrographs. The interpretation of HRTEM images might be however a challenging task [120]. For the high quality HRTEM images the correction of various aberrations of electromagnetic lenses is particularly important.

Beside the HRTEM imaging mode, a scanning transmission electron microscopy (STEM) technique was applied in the present investigation. In the scanning mode TEM, a convergent electron beam is used to produce a small electron probe, which is scanned over the specimen by adjusting the scan coils [120]. The convergent beam is applied in STEM similarly to the one used in a scanning electron microscope (SEM). The signal is generated at each position of the probe on the specimen, recorded and displayed at a corresponding point on the STEM image. The basics of the image formation in the STEM mode are described in [120]. In order to select electrons that will contribute to the image formation, different type of detectors are installed. The bright-field (BF) detector is placed onto the axis of the microscope. It picks up only the unscattered electrons at each position of the probe (Fig. 3.6). The annular detector (ADF) surrounds the bright-field detector and collects scattered electrons providing dark-field imaging. The electrons scattered to large angles (>50 mrad) are intercepted by a so-called high-angle annular detector, which sits around the annular dark-field detector [120]. These electrons are used to generate high-angular annular dark field (HAADF) STEM images. Scattering of electrons to such high angles is sensitive to the thickness and the atomic number of the material. The contrast is related primarily to the composition of the sample [124]. The HAADF STEM images can provide a lattice resolved information about the specimen that is comparable to HRTEM approach. The quality of images depends on the probe, which might have aberrations due to the lens used to form it. Therefore, high-resolution imaging requires a probe-corrected system. In this work, the HAADF STEM images are measured with the FEI electron microscope TITAN 80-300 equipped with the probe aberration corrector. The amplitude contrast is applied for the image formation. The probe-corrected system allows to receive a point-to point resolution of about 0.1 nm providing an atomically resolved information about the crystal structure of nanowires under study. The HAADF STEM mode is intensively used for structural characterisation of crystal-phase heterostructures in GaAs nanowires.

3.4 Anticipated results

Direct nanoscale correlation of optical and structural properties

NSOM imaging provides a data set, which contains a hyperspectral data cube along with a topographical image of a single nanowire. This combination of simultaneously acquired data allows to attribute high spatially resolved spectral characteristics such as a peak energy, a

peak intensity or a full width at half maximum (FWHM) of photoluminescence bands to particular coordinates along the wire with the exceptional precision. To process experimental data, extract quantitative parameters from PL spectra, and visualise obtained results, the MATLAB [125] and ORIGINLAB [126] data analysis software are used. The structural information about defects, the lattice plane stacking and the lateral extent of ZB and WZ crystal phases acquired by TEM imaging is analysed applying DIGITAL MICROGRAPH [127] software. Then, the quantitative results of optical and structural measurements from the same single nanowire are collected and plotted within the same spatial coordinate system. Thereby, the direct nanoscale structure-property correlation can be performed. Such correlation provides both an overview of structure-property relationships along the whole length of the wire and local spectral characteristics as a function of the particular stacking of lattice planes. This allow to reconstruct a local optical band structure of measured ZB/WZ crystal-phase heterostructures. Therefore, results of the NSOM-TEM nanoscale correlation can provide more accurate quantitative parameters, than it was previously reported, to verify theoretical calculations and improve previous models of the electronic band structure and quantum confinement effects in such crystal-phase heterostructures.

Limitations of the study

It is important to realise that the spatial resolution of the presented NSOM technique is still lower than the actual spatial inhomogeneity of the crystal structure of the single nanowire revealed by the TEM analysis [64]. The spatial resolution of the NSOM technique is primarily defined by the near-field probe, which is an uncoated chemically tapered optical fiber in the present study. This type of near-field probes provides spectral imaging with a spatial resolution of about 150 nm [85]. However, the uncontrolled alternation of ZB and WZ crystal phases may occur on the length scale from a few to a few tens of nanometers. The metal-coated or advanced nano-structured fiber probes may provide a better lateral resolution, up to ~ 40 nm [128]. In scattering-type NSOM, the resolution can be potentially even better using spatially designed single-crystalline conical gold tapers [129]. However, the selection of the resolution of the system also depends on the material under study. To address a local photoluminescence of individual nanowires at a moderate excitation power, the high signal-to-noise ratio is crucial. Therefore, the uncoated chemically tapered optical fiber is selected as a trade-off between the high lateral resolution and the high collection efficiency. These near-field fiber probes offer a better collection efficiency, than provided by metal-coated tips, and hence a good signal-to-noise ratio. The near-field illumination and near-field collection geometry of NSOM measurements ensure a better spatial resolution, than provided by other illumination-collection geometries at given experimental parameters (see Fig. 2.3). Moreover, the design of the fiber-based NSOM used in this work allows to perform measurements at cryogenic temperatures, which are important for the investigation of semiconductor nanostructures.

In addition, the nanowires, which have the predefined sequence or the lateral extend of ZB and WZ crystal phases by growth conditions, would substantially facilitate the NSOM-TEM structure-property analysis. As it was previously mentioned, such control over the crystal structure of III-V nanowires is still a challenging task. Therefore, GaAs nanowires with randomly distributed crystal-phase nano-domains have been chosen for this work.

3.5 Summary

In conclusion, the NSOM-TEM experimental protocol is designed to provide a direct nanoscale correlation of high spectrally and spatially resolved local optical properties with the particular crystal structure of the very same nanowire. This approach can be applied for the investigation of various III–V semiconductor nanowires and also other type of semiconductor nanostructures. The results of the application of the protocol for a comprehensive analysis of structure-property correlations in crystal-phase heterostructures of GaAs nanowires are demonstrated and discussed in the following chapters.

Chapter 4

Electronic properties of crystal-phase heterostructures in GaAs nanowires studied by near-field spectral imaging

4.1 Introduction

The tremendous success in fabrication of III–V semiconductor nanowires with well-defined principal material parameters enables to validate the great technological potential of the nanowire systems. In fact, semiconductor nanowires are used as central functional elements in various prototype devices, including solar-cells [130], photodetectors [131], nanowire lasers [132], nanowire-embedded quantum light emitters [133], and transistors monolithically integrated on Si [134], to name a few. Although the progress in the field of nanowires is apparent, the continuous scaling down of the functional elements and the developing of single-nanowire based applications spark new scientific challenges. Current research interests are ranging from the reliable control of the size, the crystal structure, and the alloy composition of individual nanowires to understand their structure-property relationships at the nanometer length scale. The latter attracts a particular interest from both technological and fundamental points of view.

As it was discussed in previous chapters, the III–V semiconductor nanowires exhibit a complex crystal structure, which can be generally characterised by a mixture of zinc blende- and wurtzite-type crystal phases of various orders and lateral extents [49]. In the particular case of GaAs nanowires, the electronic band structure of the wurtzite-type phase is characterised by a positive offset of both conduction and valence bands with respect to those of the zinc blende-type phase [19, 64]. The alternation of different phases along the growth direction of nanowires is expected to form type-II heterostructures. Therefore, a certain sequence and a lateral extent of zinc blende and wurtzite phases can induce quantum confinement states for electrons and holes and hence significantly influence optoelectronic properties of nanowires [25, 61, 64]. Importantly, crystal-phase heterostructures may provide improved optoelectronic properties due to the atomically sharp heterointerfaces in contrast to properties of the conventional heterostructures formed by a modulation of the alloy composition. To verify this hypothesis, a precise control of the mixture of zinc blende and wurtzite phases up to a single monolayer has to be achieved.

Besides the need for the ultimate growth control, optoelectronic properties of nanowires resulting from a mixture of zinc blende and wurtzite phases trigger various theoretical and

practical questions. Foremost, the band structure of the wurtzite GaAs is often discussed controversially [20–23,25,64]. This introduces an uncertainty of quantitative parameters used for a modelling of optical and electronic properties that result from a mixture of different crystal phases. In addition, the change of the order and the lateral extent of zinc blende and wurtzite crystal phases often occurs on the length scale of a few nanometers. Therefore, the expected spatial variation of corresponding optical properties also lies in the nanometer length scale. As it was previously reported, GaAs nanowires with zinc blende and wurtzite crystal-phase heterostructures exhibit intricate optical spectra due to a large amount of possible optical transitions in such mixtures [25,64]. This also results from the application of conventional diffraction limited spectroscopic techniques to image optical properties of single nanowires [25,64]. Thus, the combination of high spatial and spectral resolutions is essential to probe crystal phase induced variations of optical properties at the length scale beyond the diffraction limit.

In this context, some spectroscopic techniques, which are widely used to study III–V semiconductor nanowires, are briefly recalled below. The micro-photoluminescence measurements using confocal microscopy allow to spectrally resolve some of individual emission bands in intricate photoluminescence spectra. However, the spatial resolution of the conventional optical microscopy, which has the fundamental limit of about $\lambda/2$, makes it difficult to attribute observed optical transitions to the exact crystal phase or a mixture of crystal phases [22]. Thus, it seems promising to switch to the alternative given by the cathodoluminescence spectroscopy [25]. Cathodoluminescence techniques can provide the spatial resolution of about 50 nm, which would be sufficient for studying local optical properties of nanowires. Although it is capable to provide the high spatial resolution, cathodoluminescence spectroscopy introduces a large number of incident electrons into the wire, which may fill the crystal phase induced energy levels and eliminate the fine spatial variations of low-energy optical transitions. Despite the limitations, both techniques were previously applied for the investigation of local optical properties of nanowires and combined with the structural analysis obtained by transmission electron microscopy on the same wires [22,60,64,111,112,114]. In addition, the room temperature near-field PL spectra of individual InP nanowires were reported, although without a direct correlation of these spectra with a particular crystal structure of the same wires [128]. Therefore, the remaining uncertainties require optical spectroscopic techniques with both high spatial and spectral resolutions combined with an atomic-resolution structural characterisation that allows an unambiguous structure-property correlation.

In this chapter, the spectral imaging in the near-infrared region with a nanometer scale resolution of a mixture of zinc blende and wurtzite crystal phases in GaAs nanowires is reported. For this purpose, a dedicated custom-made near-field scanning optical microscopy system operating at cryogenic temperatures is utilised. To understand the above mentioned structure-property relationships, the *experimental protocol* combining the near-field spectral imaging and the atomic-resolution transmission electron microscopy measurements performed on the same individual GaAs nanowires is applied. The sub-diffraction-limited spectral imaging of single nanowires reveals a distinct spatial variation of the photoluminescence intensity and the photon energy along the wire axis. The characteristic lateral scale of a photoluminescence heterogeneity is found to be below the exciton diffusion length in GaAs. This suggests that the charge carriers are effectively captured by the local confinement potentials induced by the alternation of the crystal-phase nanodomains. The NSOM-TEM approach allows to establish a direct correlation of near-field spectral maps with the atomi-

cally resolved structure of a mixture of zinc blende and wurtzite crystal phases in the same GaAs nanowires. Such nanoscale correlation, which has not been demonstrated before, allows the assignment of local spectral features to a particular sequence of lattice planes in crystal-phase heterostructures. The NSOM-TEM approach provides accurate quantitative parameters required for an exact calculation of optical transitions in GaAs crystal-phase heterostructures. The observed lateral variation of both the photon energy and the intensity of photoluminescence emission as a function of different sequences of lattice planes is described within a qualitative model of spatially indirect optical transitions between electrons and holes localised in neighbouring ZB and WZ segments, respectively. The corresponding recombination energy is thereby determined by the degree of confinement of excited carriers controlled by the length and the sequence of these crystal-phase nanodomains.

4.2 GaAs–AlGaAs core-shell nanowires grown on Si

4.2.1 Growth parameters

In this work, GaAs–AlGaAs core-shell nanowires were grown under the growth conditions described in the previous work done by U. Jahn *et al.* [25]. These nanowires were selected as promising models for structure-property analyses of crystal-phase heterostructures. The sample with GaAs nanowires was grown and kindly provided by a group of Dr. Lutz Geelhaar from the *Paul Drude Institute for Solid State Electronics (Berlin)* as a part of our collaboration on this topic. The molecular-beam epitaxy technique was applied to prepare nanowires using a self-catalysed, i.e. Ga-assisted, vapor-liquid-solid (VLS) growth mode. The substrate selected for this growth is a phosphorous-doped on-axis ($\pm 1^\circ$) Si(111) wafer [25]. To desorb the water from the surface, an annealing under an ultrahigh vacuum at 300°C for 20 min was utilised, while the oxide layer was remained on the substrate. Then, the substrate was heated to 580°C and introduced into the As_4 atmosphere, which was set to the pressure of 1.2×10^{-5} mbar. To initialise the nanowires growth, the Ga shutter was opened, and the Ga flux was set to the value equivalent to the planar growth rate of 820 nm/h and the corresponding As_4/Ga fluxes ratio of 1. After 30 min, the growth of a (Al,Ga)As shell with the nominal aluminium content of 10% was started. The resulting total growth time of GaAs–AlGaAs core-shell nanowires was 1 h. Such core-shell type nanowires have a potential advantage for single-nanowire measurements, since the presence of a wide-bandgap shell efficiently suppresses a nonradiative carrier recombination and hence increases a photoluminescence yield, which is particularly important for the present study [9, 135]. In addition, the core-shell geometries open up possibilities for the defect-free combination of lattice-mismatched materials and for a tailoring of the electronic band structure of radial heterostructures [136, 137]. The interest of the present study is focused on optoelectronic properties originating from the complex crystal structure of the GaAs core, while the AlGaAs shell is used to facilitate the photoluminescence measurements. Thus, through this chapter the selected model structures will be referred to as GaAs nanowires, unless the core-shell geometry is responsible for the certain effect and hence accordingly specified.

4.2.2 Morphology and crystal structure

At the beginning, some of the GaAs nanowires were mechanically transferred from the growth substrate to the holey carbon-coated Cu grid to have a first glance at their morphology and

structural properties by TEM analysis (Fig. 4.1). The NWs have an average diameter D on the order of 150 nm and a length varying from 8 to 10 μm . Low-resolution diffraction contrast TEM micrographs in Figure 4.1 reveal bright and dark segments of different lateral extents along the nanowire axis. This indicates that the wire is not a single crystal, but it rather consists of rotationally twinned zinc blende segments and wurtzite-type inclusions, that provide different electron diffraction conditions [138]. The length of individual segments varies from a few to 130 nm, as it can be seen in Figure 4.1a. For some GaAs nanowires such segmentation is not pronounced, and, instead, areas with a very high density of defects are observed (Fig. 4.1b).

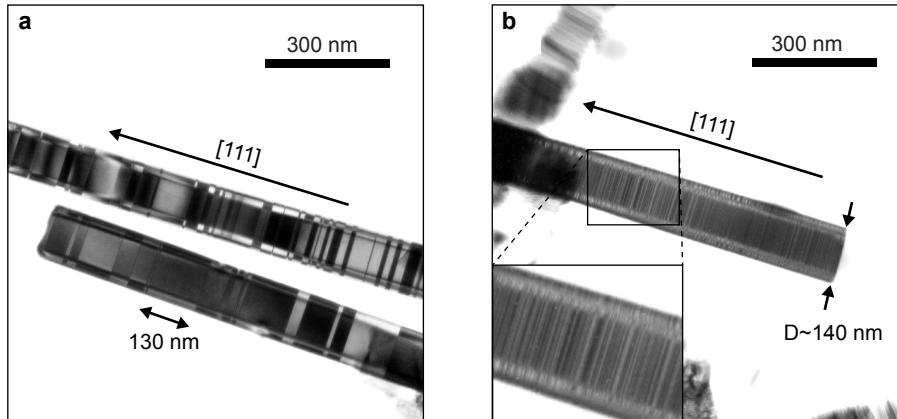


Figure 4.1: Diffraction contrast TEM micrographs viewed along the $\langle 110 \rangle$ zone axis that show GaAs nanowires dispersed onto the holey carbon-coated Cu grid: (a) clear axial segmentation of nanowires: crystal-phase nano-domains with a characteristic length from a few to 130 nanometers are observed; (b) area with a high density of crystal-phase defects.

In conclusion, the preliminary TEM observation of a representative number of nanowires indicates that their crystal structure is predominantly polytypic, which is in line with a previous study [25]. Therefore, the nanowires from this growth batch are considered as promising models for the investigation of relationships between optical and structural properties in GaAs crystal-phase heterostructures.

4.3 Experimental details

In order to probe the structure-property correlation in these polytypic GaAs nanowires, the *experimental protocol* of the direct nanoscale correlation of local optical properties with a particular crystal structure of individual nanowires, which was described in the previous chapter, is implemented. This includes the preparation of a substrate for multiple single-nanowire measurements, the sub-diffraction-limited spectral imaging, and the subsequent structural characterisation of the same selected wires. For this purpose, a silicon substrate patterned with gold alignment marks is used as a physical support for nanowires. Some GaAs nanowires are gently transferred from the growth substrate onto this Si substrate by ultrasonication and drop-casting techniques avoiding any further processing prior to optical measurements. Once the nanowire sample is ready and promising wires are selected the optical characterisation by the near-field scanning optical microscopy technique is performed.

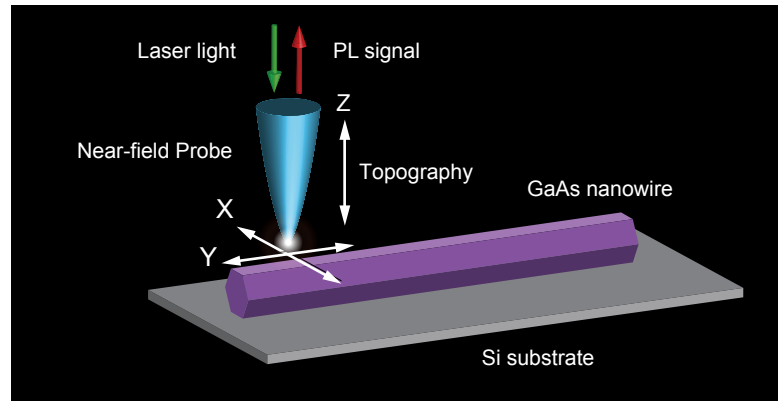


Figure 4.2: Schematic of the NSOM measurements of a single nanowire. Local PL spectra are recorded in the near-field illumination and near-field collection geometry using an uncoated, chemically etched fiber probe.

The substrate with nanowires is fixed on the sample holder of a continuous flow liquid-helium cryostat inside the NSOM vacuum chamber and cooled down to 10 K. The purpose of applying cryogenic temperatures is to increase the photoluminescence yield of single nanowires and avoid thermally activated effects [9]. For the optical excitation a line of the 0.5-mW helium-neon laser at the wavelength of 543-nm, i.e. 2.283 eV, is used. The excitation power for a single nanowire imaging is adjusted using the linear variable neutral density filter to insure the sufficient signal-to-noise ratio and at the same time to avoid the perturbing effect of the high-power laser beam on the photoluminescence spectra. Thus, a laser line power of only 115 nW is coupled to the optical fiber, which satisfies these requirements. The collected photoluminescence signal is dispersed then in an 0.5-m focal length imaging monochromator. The spectral resolution of spectral imaging is about 3 meV. Finally, the photoluminescence signal is recorded by the nitrogen-cooled InGaAs charge coupled device camera. A schematic of the single nanowire NSOM experiment is depicted in Figure 4.2. For the spectral imaging, the fiber-probe is raster-scanned across the sample surface of $4 \times 4 \mu\text{m}^2$ containing the nanowire of interest with a sampling step size, i.e. a spatial pixel, of 40 nm (X- and Y-axis). At every step, a full photoluminescence spectrum is recorded in the energy range from 1.244 to 1.872 eV, which includes PL emission expected for GaAs nanowires. For maintaining the fiber probe in a constant and close proximity to the sample surface, a shear-force distance control method is used simultaneously providing an AFM-like topographical image of the nanowire (Z-axis, a constant gap imaging)¹.

Following the spectral imaging by NSOM, exactly the same nanowires were studied by transmission electron microscopy (TEM). A focused ion beam (FIB) target preparation technique is applied to lift-off nanowires from the pre-patterned Si substrate and prepare the single-nanowire TEM sample. The crystal structure of nanowires is then analysed in the FEI microscope TITAN 80-300, which is equipped with a goniometer that allows the specimen to be tilted up to 30° . This gives more degree of freedom to reach the required crystallographic orientation for structural analysis. The measurements of the lattice structure are performed in the $\langle 110 \rangle$ crystallographic orientation, in which the stacking sequence of consecutive $\{111\}$ lattice planes could be determined. This allows to distinguish between ZB and WZ crystal

¹For details about the NSOM technique the reader is referred to Chapter 2.

phases. The entire length of each nanowire is investigated providing both the overview of the nanowire morphology, planar defects, and dislocations as well as the high-resolution information about the crystal structure, defects and the lattice planes stacking.

The discussion of the experimental findings is organised as follows. The next two sections provide an overview of results on near-field spectral imaging and transmission electron microscopy analysis that were performed on the same GaAs nanowires. In the following section, the discussion is focused on a direct nanoscale correlation of extracted optical and structural properties of crystal-phase heterostructures. The last section summarises the important findings of this chapter.

4.4 Near-field spectral imaging of individual nanowires

4.4.1 Outcome of the single-nanowire experiment

In Figure 4.3, the typical outcome of the NSOM mapping experiment on a single GaAs nanowire is illustrated alongside with the SEM image of the same wire. The first two panels, (a) and (b), show spectral and simultaneously acquired topographical images of the wire, respectively. In Figure 4.3a, the PL spectrum of each spatial pixel is integrated over the whole energy range. The resulting image provides a two-dimensional map of the total PL intensity and reveals thereby all emission centres within the scan area. The combination of spectral and topographical images of the same scan area allows then an unambiguous assignment of the PL spectra to the particular position of the near-field probe relative to the nanowire axis. This makes it possible to accurately align the spatial coordinates of optical characteristics and those of structural characteristics obtained from different experiments on the same nanowire.

As it can be seen from the comparison between NSOM maps and the SEM image of the same wire (Fig. 4.3a,c), the total PL intensity is strong in pixels sampled along the nanowire and drastically drops in pixels sampled away from the actual position of the wire. To emphasise this observation, linear cross-sections are taken from these maps at positions indicated by the white dashed line in Figure 4.3a and plotted in Figure 4.3d. Indeed, the PL intensity abruptly decays as the near-field probe moves away of the wire position, while the topographical profile changes slowly. The former indicates that the near-field probe provides a very local collection of the PL signal and hence the high spatial resolution of spectral imaging. Particularly, the broadening of the optical image Δw of the wire is estimated to be about 100 nm in comparison with the nanowire diameter (Fig. 4.3d). The slow change of the topographical profile reflects the convolution of the actual shape of the apex of the near-field probe and the nanowire geometry producing a broader topographical image, which is however sufficient to resolve the position of the wire on the substrate.

In addition, the pronounced spatial variation of the total PL intensity along the wire axis is observed (Fig. 4.3a). It is anticipated, that the intensity distribution might be affected by an unintentional variation of the distance between the near-field probe and the sample surface. To verify the reliability of the NSOM data set in this respect, linear profiles along the nanowire are taken from spectral and topographical images (as indicated in Fig. 4.3b) and plotted in Figure 4.3e (top and bottom panels, respectively). Indeed, two distinct PL intensity maxima are observed along the nanowire axis, while the topography profile reveals its negligible variations along the wire. This leads to the conclusion, that the observed inhomogeneity of the PL intensity is an intrinsic optical property of the sample rather than

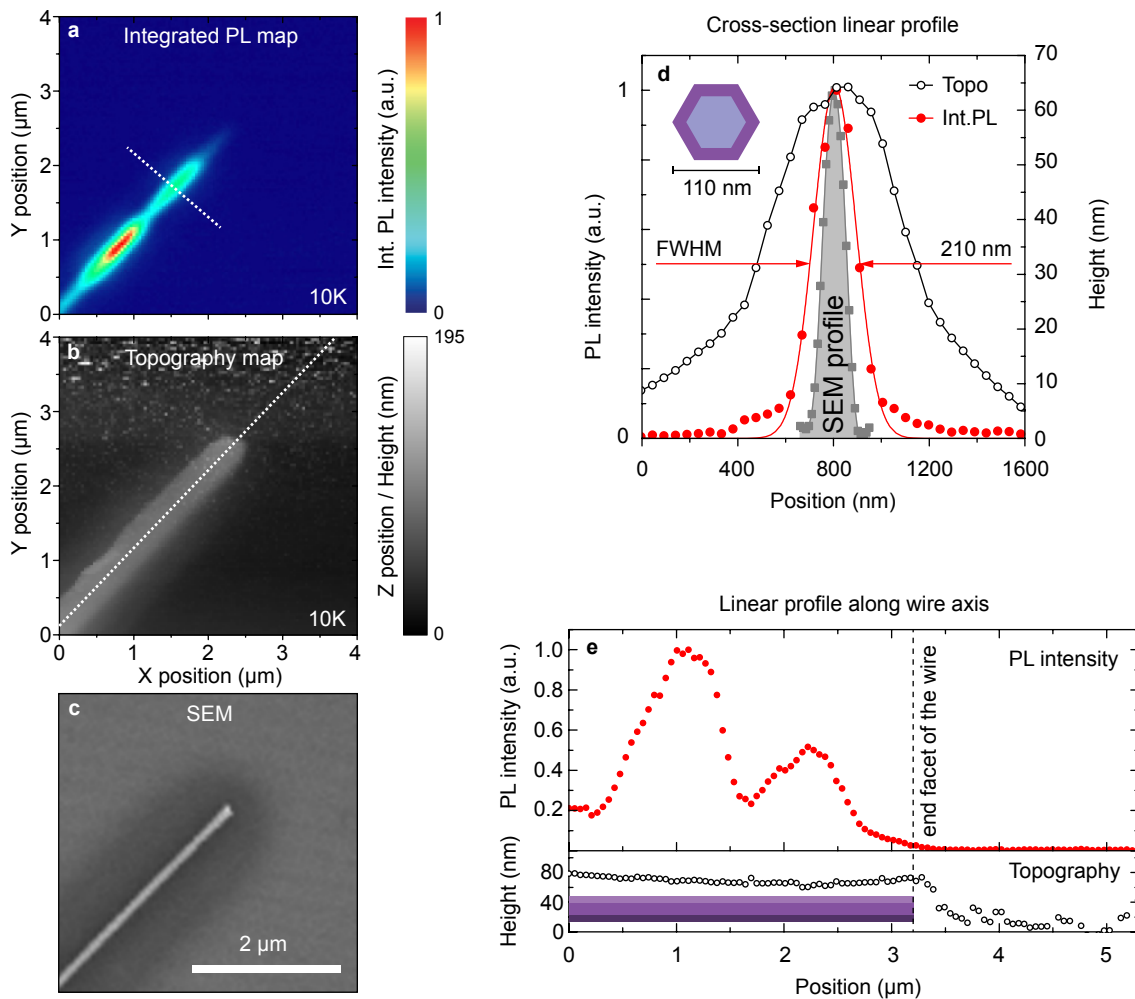


Figure 4.3: Hyperspectral and topographical imaging of a single GaAs nanowire by NSOM: (a) Two-dimensional map of the total PL intensity of the NW acquired at a temperature of 10 K. The image is constructed by a raster scan of the near-field probe over a surface area of $4 \times 4 \mu\text{m}^2$ with a step of 40 nm/pixel. A full near-field PL spectrum is recorded in the energy range between 1.244 and 1.872 eV at every pixel of the image within an integration time of 500 ms per spectrum. (b) Topography image recorded simultaneously during the scan process with the same spatial sampling, 40 nm/pixel. The SEM micrograph (c) shows the actual size of the corresponding NW. Spatial scales of (a-c) are equal. (d) Cross-sections of the wire at the position shown in (a) indicate the high spatial resolution of the near-field PL map (red full circles), even though the topographical image of the wire is relatively broad (black open circles). The PL cross-section is well fitted by a Gaussian curve (red) with an FWHM of 210 nm at the actual wire diameter of about 110 nm (inset). (e) The linear profile along the wire axis shows a distinct spatial variation of the total near-field PL intensity (top panel), while the spacing between the near-field probe and the wire surface is maintained at a constant level (bottom panel).

an experimental artefact.

Having discussed the typical outcome of the NSOM mapping experiment and the reliability of collected data, a comprehensive analysis of a complete single GaAs nanowire with emphasise on the direct nanoscale correlation of its optical and structural properties is presented in the following paragraphs.

4.4.2 Near-field map of the local carrier recombination

Figure 4.4 presents the complete map of a single 8.7- μm -long GaAs nanowire performed by NSOM at a temperature of 10K. The full map of the wire was composed of three subsequent rectangular NSOM scans covering the region on the substrate that contains the nanowire of interest. The top panel (Fig. 4.4a) shows a minor bending of the topographical image of the wire, caused by a slow drift of the sample during the scan processes. The black arrows indicate end facets of the wire used as markers to set an arbitrary beginning of the coordinate axis along the wire. In Figures 4.4b and 4.4c, spatial images of the local PL peak intensity and the PL peak energy are presented. When two or more PL peaks arise in a single pixel of the image, the most intense PL peak of the spectrum of a given pixel is selected and plotted.

It is seen that the spatial distribution of the PL peak intensity can be described by a set of clearly separated intensity domains of a various axial extent (Fig. 4.4b). The axial segmentation of optical properties is even more pronounced in the image of the PL peak energy position (Fig. 4.4c, right panel). The sharp borders between some PL peak energy domains, i.e. segments of a constant energy, coincide with abrupt borders of PL peak intensity domains, as emphasised by the dashed lines. Also, it is found that the axial extent of some segments of constant energy is as small as 270 nm. In Figure 4.4c, there is a minor variation of PL peak energy at some positions in the direction that is perpendicular to the nanowire axis. As it can be seen, when the near-field probe moves away from the actual wire position, the PL intensity drops drastically (Fig. 4.4b). Therefore, the determination of the PL peak energy is less accurate in these pixels due to the low signal-to-noise ratio and might cause such deviation.

A superficial analysis of the axial variation of the emission energy in Figure 4.4c (see colour scale), reveals that the short-length optical segments appear at energies that are predominantly well below the band gap $E=1.519$ eV of zinc blende GaAs at 10K. In contrast, the emission at energies that are close or slightly above the band gap of zinc blende GaAs is spread over a large area near the middle part of the wire. The vanishingly low PL intensity at the left end of the nanowire cannot be clarified so far by relying only on the NSOM data set and will be discussed later.

The NSOM map of the peak energy shows that the emission of the constant energy is localised in well-separated segments and varies as a function of a position along the wire. To emphasise the enhanced localisation of the PL signal as a function of the emission energy, the slices from the hyperspectral data set at specific photon energies are selected and plotted in Figure 4.5a-d. These slices represent the PL intensity maps of particular spectral components derived from Figure 4.4c (black crosses). The first map (Fig. 4.5a) shows the distribution of the PL peak intensity at the energy above the band gap of bulk GaAs at 10K. It is seen that the PL signal at this energy is spread over the 1- μm -length area of the wire. The spectral components at energies below the band gap of bulk GaAs (Fig. 4.5b-d) are localised within well-separated segments in correspondence to the spectral map in Figure 4.4c.

Representative PL spectra from pixels with a maximum of intensity at a given photon

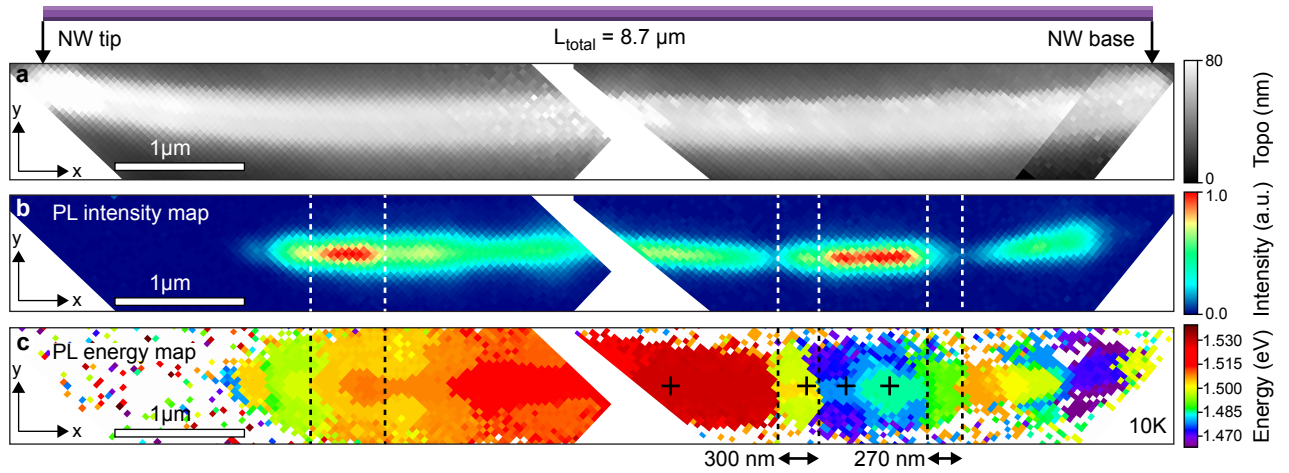


Figure 4.4: Spectral imaging of a mixture of zinc blende and wurtzite crystal phases in a single GaAs nanowire performed by NSOM. A complete map of the $8.7\text{-}\mu\text{m}$ -long wire is acquired within 3 subsequent scans of the rectangular areas, containing the nanowire of interest, with a spatial sampling of 40 nm/pixel . A full near-field PL spectrum is recorded at a temperature of 10K in the energy range between 1.258 and 1.904 eV at every pixel of the image within an integration time of 1 s per spectrum. (a) Topographical image of the single GaAs nanowire. Black arrows indicate the corresponding end facets of the wire. (b) Two-dimensional map of photoluminescence intensity of the most intense peak selected at each pixel of the image. (c) Two-dimensional map of the photon energy of the radiative recombination. If two or more spectral features appear in a single pixel, the photon energy of the most intense peak is selected. The scale bar of $1\text{ }\mu\text{m}$ applies for all maps. Both photoluminescence intensity and photon energy appear within distinct and well-separated segments, as emphasised in some areas by the dashed lines and black cross-marks.

energy are plotted in Figure 4.5e and the corresponding pixels are marked by the black crosses (Fig. 4.5a-d). The position of the black crosses coincides with those in Figure 4.4c. Some pixels contain two or more emission bands (Figure 4.5e, yellow spectrum), which originate from neighbouring local recombination centres on the distance smaller than the sampling length, i.e. size of the pixel, or the resolution power of the NSOM technique.

Finally, the qualitative analysis of the NSOM hyperspectral data set provides a comprehensive high spectrally and spatially resolved information about PL heterogeneity of the single GaAs nanowire. It was demonstrated that the spatial origin of acquired spectral features along the wire axis can be accurately determined by the combination of spectral and topographical imaging provided by NSOM. The presented GaAs nanowire exhibits spectrally rich PL emission with a distinct variation of spectral characteristics as a function of the near-field probe position along the wire. Remarkably, the enhanced signal localisation at particular photon energies is found to be on the length scale well below the exciton diffusion length in GaAs. Moreover, the energy of localised PL intensity domains is predominantly below the band gap of GaAs. These observations suggest the existence of local confinement potentials that efficiently capture and localise photogenerated carriers in radiative recombination centres. To understand the nature of these local recombination centres, the same GaAs nanowire was prepared and studied by transmission electron microscopy, following the *experimental protocol* of nanoscale correlated analysis.

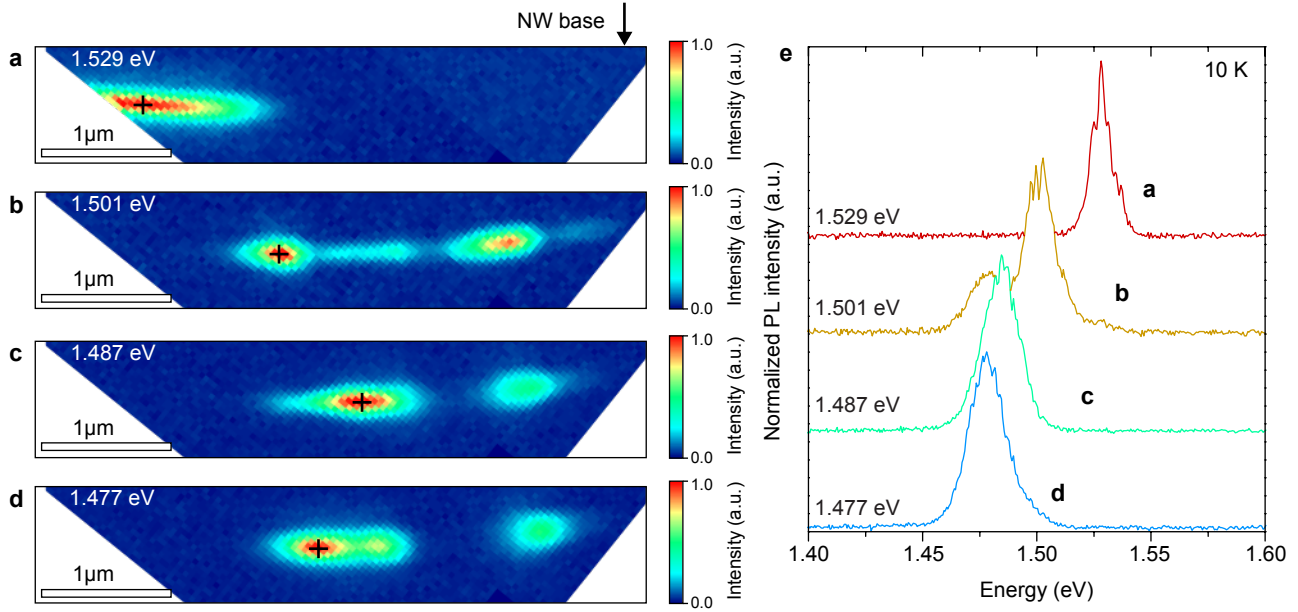


Figure 4.5: Spatially resolved spectroscopic information from the hyperspectral PL data set: (a-d) Two-dimensional maps that show local intensity variations for the selected spectral components in Figure 4.4c (right panel, black crosses), i.e. at photon energies of a – 1.529, b – 1.501, c – 1.487, and d – 1.477 eV, respectively. The black crosses indicate the position of the most intensive pixels at selected energies and match with positions of those in Figure 4.4c. The PL emission appears in pronounced and well-separated local recombination centres of various lengths. The scale bar is 1 μm . (e) Representative local PL spectra from pixels marked by black crosses. The colour code corresponds to the PL peak energy as shown in Figure 4.4c. Some pixels contain two or more spectral features (yellow PL spectrum), which originate from neighbouring local recombination centres.

4.5 Imaging of the crystal structure of nanowires

In order to address the main aspect of this study, which is a direct nanoscale correlation of optical properties to the local crystal-phase heterostructures, the systematic structural analysis of the same GaAs nanowire studied optically was performed. In Figure 4.6a, the result of diffraction contrast imaging of the wire by transmission electron microscopy is presented. The image is composed of a series of overlapped TEM micrographs along the whole available nanowire. The middle part of the wire of about 1.5 μm is cut because of the preparation of the TEM sample and hence is not available for structural analysis. The remaining lamellae contain two parts of the wire of about 3 and 4 μm length, as shown in Figure 4.6a. TEM images are scaled and presented in correspondence to the total length of the wire. The black vertical arrows point to the end facets of the wire, which are used to align the information acquired from spectral and structural imaging (see Fig. 4.4). The droplet that is visible on the left-hand end of the wire allows to assign this end facet to the NW tip, and the right-hand end of the wire to the NW base, respectively (Fig. 4.6a). The narrow dark and bright stripes, which alternate along the nanowire axis, indicate that the wire is not a single crystal (Fig. 4.6a, inset) [138]. As it was previously mentioned, such dark and bright stripes typically suggest that the crystal structure of the GaAs nanowire

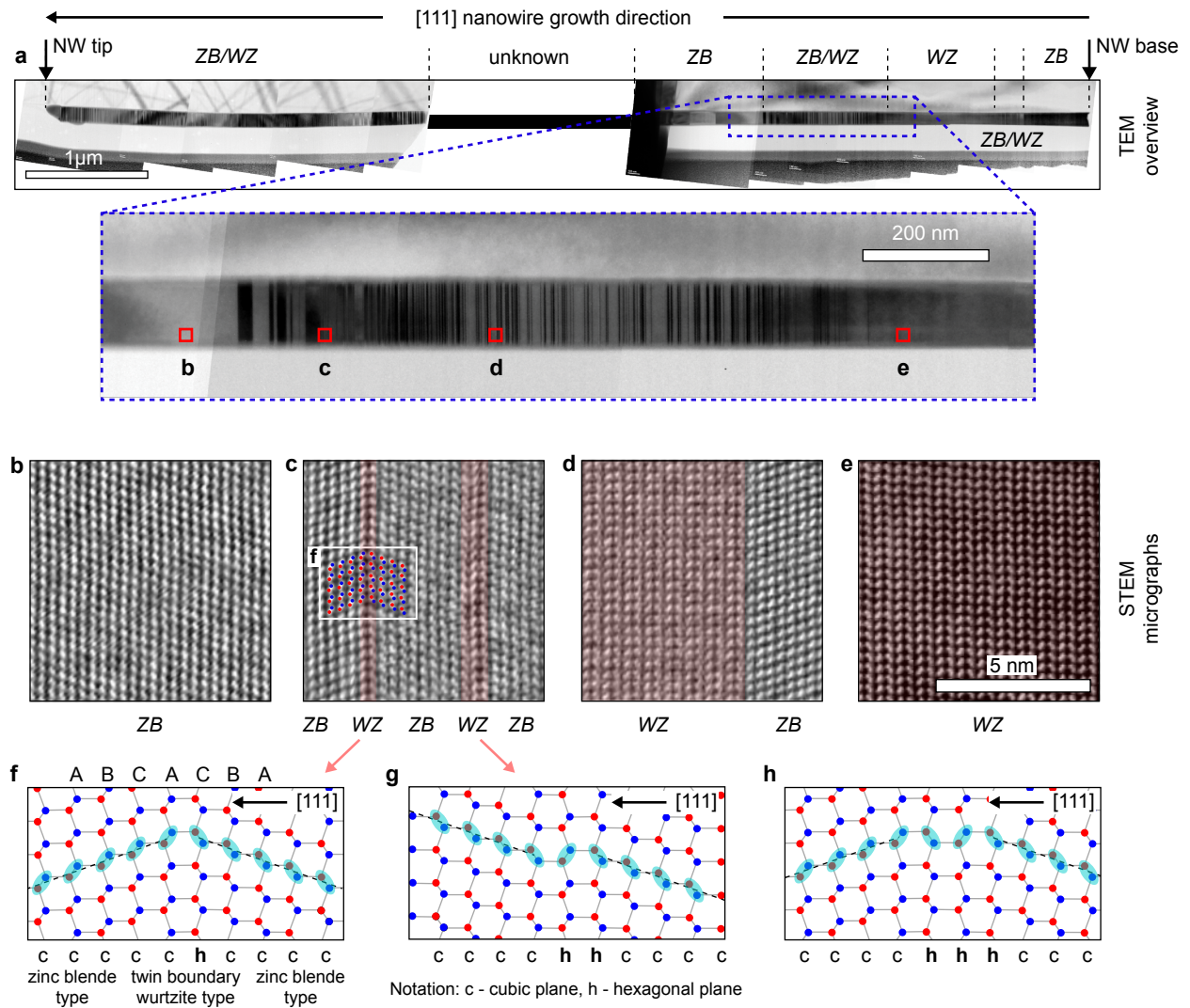


Figure 4.6: Mapping of the crystal phase structure of the single GaAs nanowire: (a) Complete diffraction-contrast TEM overview of the wire at a low magnification. Inset: enlarged segment of the nanowire indicated by the blue rectangle. The bright and dark stripes correspond to the disordered superlattices of rotational twins of the zinc blende phase and wurtzite inclusions. The droplet on the left end of the nanowire indicates its top end, which is labeled as a “NW tip”. The scale bar is 1 μm. (b-e) High-resolution STEM micrographs show the crystal lattices stacking along the [111] direction at different positions of the wire (red squares). The atomically resolved map of the crystal structure allows to distinguish several regions of the wire with characteristic crystalline phases. The scale bar of 5 nm applies to all STEM micrographs. (f-h) Crystal structure models demonstrate the different stacking of lattice planes and the indexing scheme.

can be characterised by rotationally twinned zinc blende type segments and wurtzite type inclusions that produce different electron diffraction conditions [138]. In order to perform a quantitative analysis of the crystal structure, series of high-resolution HAADF STEM micrographs covering the nanowire of interest were systematically acquired.

In Figure 4.6d-e, representative atomically resolved STEM micrographs are selected from various locations marked by the red squares in Fig. 4.6a. These images are acquired in the $\langle 110 \rangle$ projection and oriented in correspondence to the nanowire $[111]$ growth axis. In STEM micrographs, each elongated bright spot, “dumbbells”, corresponds to a pair of Ga and As atoms, and hence each vertical line made of these spots represents a $\{111\}$ lattice plane. For the quantitative description of a mixture of zinc blende and wurtzite crystal phases, the indexation of lattice plane sequences has to be introduced.

First, a rotational twin plane of the zinc blende type GaAs is considered. In Figure 4.6c (left side), the STEM micrograph of rotationally twinned ZB segments is demonstrated. The crystal structure model illustrating the interface between two rotationally twinned zinc blende segments is shown in Figure 4.6f. In this case, the ZB region with the $\dots ABCABC \dots$ stacking sequence is followed by the same ZB structure but with its atomic arrangements rotated at the interface between two segments by 180° around the $[111]$ growth axis. These different lattice plane orientations appear as dark and bright stripes in TEM diffraction contrast images in Fig. 4.6a. The rotational twinning forms an $\dots ABCACBA \dots$ stacking sequence at the interface. The CAC stacking at the twin boundary is commonly considered as an inclusion of a single unit of the WZ type structure in a ZB matrix.

Second, the occurrence of rotational twins at every $\{111\}$ plane of a ZB structure, i.e. a consecutive twinning, produces thicker WZ type segments (Fig. 4.6g,h). Therefore, the indexation have to reveal the occurrence of a single wurtzite-type lattice plane as well as the sequence of several wurtzite-type planes of a larger wurtzite segment. Following the work of G. Priante *et al.* [139] on the stacking sequences in III–V nanowires, the following indexation scheme is selected (Fig. 4.6f-h). At the beginning, the first lattice plane and the direction of the indexation are selected, e.g. from the left to the right. Then, the next consecutive plane is assigned to the zinc blende (cubic, c) plane if its Ga-As bonds are parallel to bonds of the preceding plane. If they are not parallel, the consecutive plane is assigned to the wurtzite (hexagonal, h) one, as shown in Figure 4.6f-h [139]. In the high-resolution STEM micrograph, it appears as parallel and not parallel Ga-As “dumbbells” along the growth axis, respectively. Therefore, all lattice planes resolved in STEM micrographs can be labeled either as a cubic (c) or a hexagonal (h). Importantly, that such indexation is not unique and can be shifted by one or two planes depending on the first selected plane and the direction of indexation or if it is defined by other indexation schemes. Nevertheless, resulting sequences are the same and hence allow to extract a quantitative information from structural analysis, which is sufficient for the current study of structure-property correlations.

Finally, the representative STEM micrographs in Figure 4.6(b-d) illustrate the following crystal phase mixtures: (b) – a twin-free ZB phase; (c) – a ZB phase with two inclusions of a WZ type phase of one hexagonal plane and two consecutive hexagonal planes, respectively; (d) – two large wurtzite (left) and zinc blende (right) type segments; (e) - a defect-free WZ phase.

Knowing the atomically resolved crystal structure, different segments of the nanowire can be categorised into three major groups. Interfaces between these segments are marked by the black dashed lines in Figure 4.6a and labelled accordingly: ZB — a virtually twin-free ZB region, ZB/WZ — a mixture of zinc blende and wurtzite phases of various fractions,

WZ — a virtually defect-free WZ region. Regions with a similar crystal structure have the same labelling.

4.6 Structure-property relationships at the nanoscale

4.6.1 Correlation of spectral imaging and structural analysis

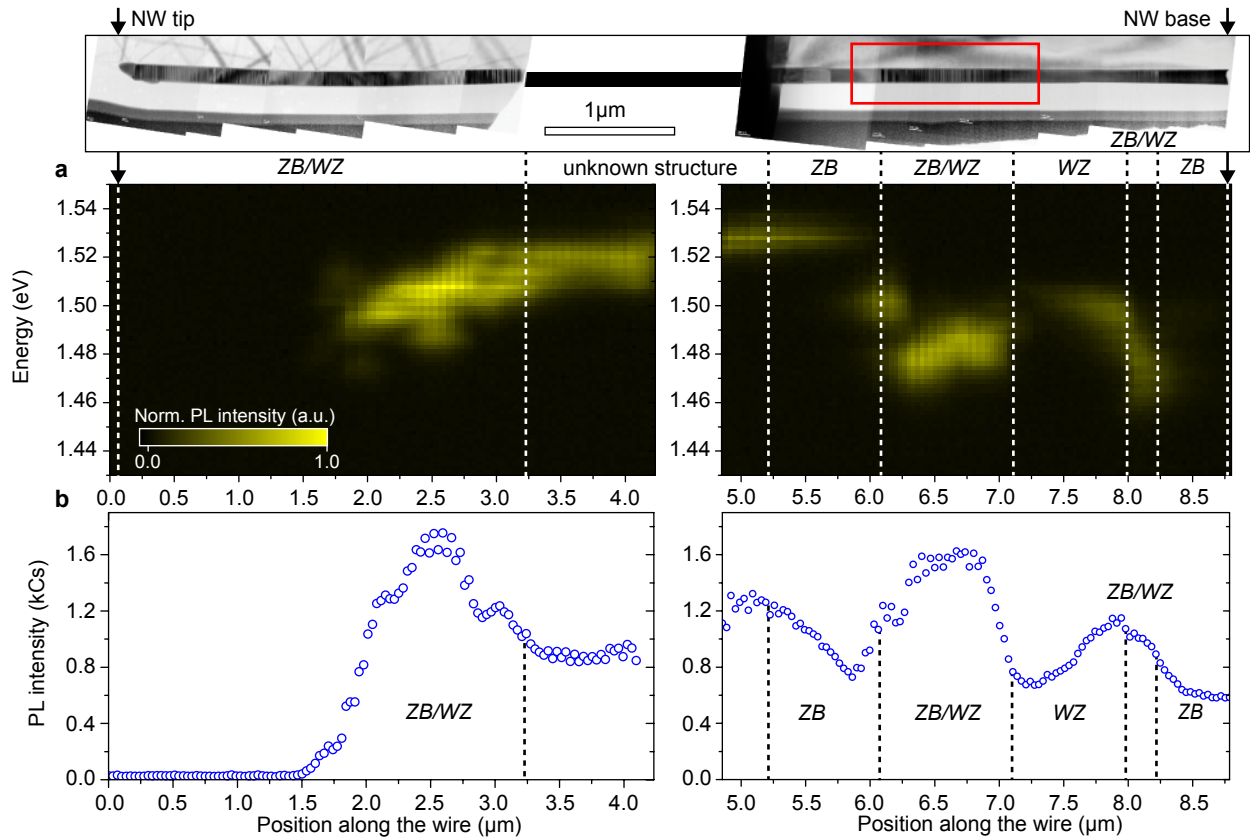


Figure 4.7: Spatial and spectral resolution of a mixture of zinc blende and wurtzite crystal phases and its correlation to their structural characteristics: (a) Mapping of local photoluminescence spectra from pixels selected along the wire. The scale bar applies to both the map of local PL spectra and the TEM overview in Fig. 4.6. (b) The spatial variation of the PL peak intensity along the nanowire. Top panel: the structural information from Fig. 4.6 is directly superimposed on spectroscopic data. The horizontal axis indicating the position along the wire is common for the top and bottom panels.

Structural imaging of the same nanowire makes the assignment of the local optical properties to the particular crystal structure straightforward. For this purpose, the local PL spectra are selected from pixels along the nanowire axis shown in Figure 4.4 and plotted in Figure 4.7b as a two-dimensional map combining the spatial and spectral information. There, the vertical axis indicates the photoluminescence energy and covers the energy range between 1.43 and 1.55 eV, which includes all spectral features. The horizontal axis indicates the position of each local PL spectrum along the nanowire. Following the *experimental protocol* of the direct nanoscale correlation, the spectral and structural data are scaled and

aligned using the end facets of the wire indicated in Figure 4.4 and Figure 4.6 (black arrows). The previously derived classification of crystal structure segments (Fig. 4.6a) is highlighted by the dashed lines. Now, local PL spectra can be directly related to the corresponding crystal-phase mixture. Therefore, the nanoscale correlation of optical and structural properties within each individual segment can be performed.

At a glance, the appearance of each spectral feature perfectly follows the segmentation derived from the preliminary crystal structure analysis. Such spatial variation of local spectral components of PL emission as a function of the particular crystal structure is especially noticeable in the combined spatial-spectral map shown in Figure 4.7a. In addition, to emphasise the spatial variation of the local PL intensity, the corresponding data is plotted in Figure 4.7b. The spatial inhomogeneity of the PL peak intensity along the wire is also in line with the derived classification of the crystal structure. The PL emission at the energy above the band gap of ZB bulk GaAs is found in the region from 5.0 to 6.0 μm of the wire (Fig. 4.7a, right panel). Its energy is constant near the *ZB* region. However, its intensity decays gradually through this region while approaching the *ZB/WZ* region (Fig. 4.7a, bottom right panel). Spectral components of all regions labelled *ZB/WZ* appear at a high variety of photon energies but below the band gap of bulk ZB GaAs. Remarkably, the emission from these segments and hence at the energy below 1.519 eV is characterised by a strong PL intensity, as it can be seen in Figure 4.7b. The emission near the “tip” end of the wire is vanishingly low. This part of the wire is characterised by a very high density of crystal phase defects, which might cause a suppressing of the PL signal. In the *WZ* region (Fig. 4.7a, right panel), which is a virtually defect-free *WZ* segment, PL emission is found at the energy also below the band gap of bulk ZB GaAs. The intensity of this emission increases while approaching the *ZB/WZ* region from the left to the right. At the interface between these two regions, the high-energy spectral component of the *WZ* region abruptly vanishes while the low-energy one appears on the site of the *ZB/WZ* region.

The combination of NSOM spectral and TEM structural imaging shown in Figure 4.7a,b provides a direct correlation of a crystal structure and optical properties of a single nanowire, which is similar to the approach previously reported by Heiss *et al.* [22]. However, taking the advantage of the sub-diffraction limited spatial resolution of individual spectral features provided by NSOM, the nanoscale structure-property relationships of individual segments of the wire can be directly derived.

4.6.2 Emission at energy above the band gap of zinc blende GaAs

The detailed discussion of the structure-property correlation is started from the segment of the GaAs nanowire in the region from about 5.0 to 6.0 μm (Fig. 4.7a, right panel). The emission is found at the energy of about 1.528 eV, which is clearly above the band gap energy 1.519 eV of bulk ZB GaAs. Importantly, such high-energy emission is observed only for this particular segment of the wire. The intensity maximum of this emission is observed in the region, where the exact crystal structure is not available due to the TEM sample preparation (Fig. 4.7, top panel). However, the high-energy PL intensity is spread throughout more than a 1- μm -long area and hence observed also in the neighbouring *ZB* region. The complete detection energy range of this region was examined, and no other PL bands, except the aforementioned, were found. The energy of PL emission above the band gap of bulk ZB GaAs was previously reported by Jahn *et al.* for nanowires grown under the same conditions as in the present study [25]. Luminescence spectra of these GaAs nanowires were measured

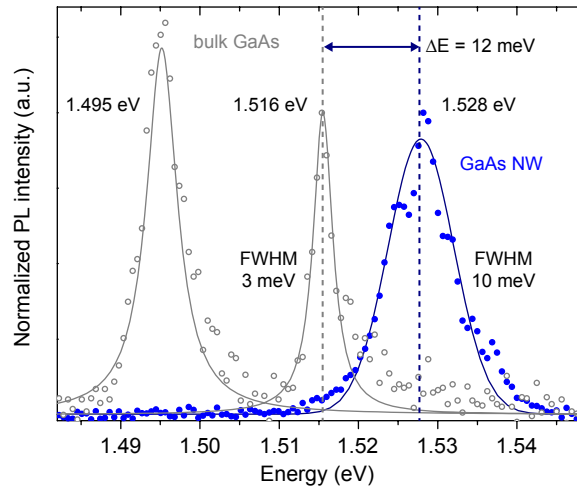


Figure 4.8: Representative near-field PL spectra of a zinc blende segment of the GaAs nanowire (blue full circles) and the epitaxial bulk GaAs sample (grey open circles) measured by NSOM at 10K. The PL spectra are normalised for clarity. The experimental spectra from the selected spectra of the wire and the planar GaAs are fairly well approximated by Gaussian and Lorentz curves, respectively. The PL emission of the zinc blende segment is blue-shifted for about 12 meV in comparison with the energy of a free exciton transition $E=1.516$ eV in bulk zinc blende GaAs at 10K. The FWHM of the PL band of the wire is about threefold of the one of epitaxial bulk GaAs.

by cathodoluminescence spectroscopy and discussed in terms of a type-II band alignment of ZB/WZ crystal phase heterostructures [25]. It was suggested that the luminescence at the energy above the band gap of bulk ZB GaAs results from electron confinement in thin ZB type inclusions between two neighbouring WZ sections [25]. In the present study, taking an advantage of the direct correlation of high spatially resolved optical and structural properties provided by the NSOM-TEM strategy, nanoscale phenomena that are potentially responsible for the high energy PL emission are discussed.

In order to exclude possible experimental artefacts and a contamination of the nanowire sample, the PL emission of a 1- μm -thick planar epitaxial layer of GaAs, grown in the same MBE system as nanowires, was measured by NSOM (following the similar approach in [22]). In Figure 4.8, the PL spectrum of the GaAs epilayer (grey open symbols) is superimposed on the PL spectrum from the NW region that shows the high-energy emission. To address their spectral characteristics, the experimental data on the GaAs epilayer and the nanowire are fairly well approximated by Lorentz and Gaussian curves, respectively. The PL peak energy of the GaAs epilayer is found at 1.516 eV, which is typical for free-exciton transitions in pure bulk ZB GaAs [70, 140]. An additional low-energy PL peak at about 1.495 eV can be assigned to carbon related band-acceptor transitions [70, 141, 142]. The FWHM of both PL peaks is about 3 meV, which corresponds to the applied spectral resolution of the system. Therefore, the emission from the GaAs epilayer grown in the same MBE system is consistent with optical transitions in bulk ZB GaAs reported by various authors. As a consequence, NSOM measurements on the planar epitaxial layer of GaAs reproduce well-known results such as energies of optical transitions and provide reference near-field PL spectra for further discussions. The PL emission from the region from 5.0 to 6.0 nm, which comprises also the

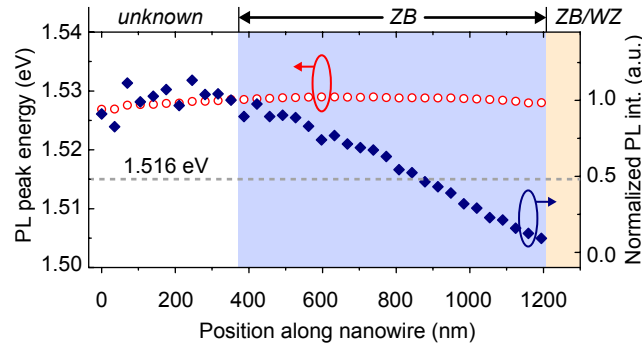


Figure 4.9: Spatially resolved spectroscopic properties extracted from the fitting of the data presented in Figure 4.7a at the position from around 5.0 to 6.0 μm . The beginning of the spatial axis is set for simplicity at the position of the first high-energy PL peak observed in the spectral map. The energy of PL emission (red open circles, left Y axis) of 1.527 \pm 0.002 eV of the zinc blende segment is constant along the whole area. The integrated PL intensity (blue full symbols, right Y axis) is constant at the distance of more than 800 nm from the *ZB/WZ* region and it monotonically decreases upon approaching this region. The decay of integrated PL intensity can be attributed to the diffusion of carriers to the area with low-energy recombination centers (see *ZB/WZ* region).

ZB segment (Fig. 4.7a, right panel) can be compared now with reference PL spectra from planar *ZB* GaAs. The emission from this region of the wire is peaked at 1.528 eV and hence blue-shifted at about 12 meV in comparison with the energy of excitonic transitions in bulk *ZB* GaAs (Fig. 4.8). The FWHM of this PL band derived from the fitting of the experimental data is 10 meV, which is about three times larger than that of the GaAs epilayer.

Interestingly, high-resolution TEM imaging of this region, except of the cut segment in the middle of the wire (Fig. 4.7a, top panel), reveals no significant variations on the crystal structure. It can be characterised as a virtually ideal *ZB* type structure, which consists of only three large rotationally twinned *ZB* segments throughout the distance of 1 μm . This provides a negligibly low density of twin planes of 3 μm^{-1} . In order to emphasise the spatial variation of optical properties, all PL spectra from this region were fitted by Gaussian curves and the corresponding spectral characteristics are plotted in Figure 4.9. The colour code indicates the position of the *ZB* region (light blue) and the interface with the *ZB/WZ* region deduced from structural analysis (Fig. 4.7a, top panel).

First, the PL peak energy of about 1.528 eV is constant along a 1.2- μm -long segment. Remarkably, the absence of spatial variations of the emission energy correlates well with the absence of significant changes in the crystal structure, which is almost a twin-free *ZB* type GaAs. However, the emission energy is blue-shifted \sim 12 meV in comparison with the one expected for the ideal *ZB* type GaAs, as it was shown above. The observed twin planes in this region cannot be a reason, since the localisation of holes on the interface between rotationally twinned zinc-blende segments is expected to lead to the red-shift instead of the blue-shift [48]. Second, the PL peak intensity is independent on the presence of twin planes and gradually decays while approaching the *ZB/WZ* region, where the low-energy optical transitions abruptly appear (Fig. 4.7a, right panel). The gradual decay of the PL intensity occurs on the length of about 800 nm, and the emission at 1.528 eV is completely vanished at the end of the *ZB* region. Interestingly, the observed continuous decay of this PL band

is comparable with a diffusion length of excited carriers in GaAs nanowires at 7–10 K [143]. Hence, the spatial variation of PL peak intensity can be explained by the escape of carriers from the *ZB* region due to the drift-diffusion transport, their subsequent localisation and the radiative recombination at low-energy states in the *ZB/WZ* region.

Therefore, the results of correlated optical and structural analysis lead to the following observations: (a) the constant emission energy is in a good agreement with negligible variations in the crystal structure; (b) the delocalisation of the near-field signal over the 1.2- μm -long area in combination with a virtually defect-free crystal structure suggests the absence of the local confinement states in this area, which could effectively capture the excited carriers; (c) the blue-shifted PL peak energy is inconsistent with the one expected for the virtually defect-free *ZB* type GaAs and hence cannot be solely explained by the local crystal phase structure.

So far, the assignment of the observed high-energy PL emission relying on the presented above experimental results was not achievable. It is anticipated, that there could be a unique mixture of zinc blende and wurtzite crystal phases in the small segment of the nanowire that is cut in the lamella prepared for structural imaging (Fig. 4.7a, top panel). The speculation on the resulting crystal-phase induced local confinement potential, which could cause the high-energy PL, is might be ambiguous, generally because of the large delocalisation of the near-field signal of the constant energy. In addition, the direct correlation of local optical and structural properties (Fig. 4.7a) shows that the regions with a mixed crystal phase structure, i.e. labeled as *ZB/WZ*, exhibit PL emission at energies below the band gap of *ZB* GaAs.

In this context, to understand the phenomena that could possibly induce the PL emission at energies above the band gap of *ZB* GaAs, the alloy composition profile of individual nanowires is also investigated.

Supporting composition analysis of GaAs–AlGaAs core-shell nanowires

As it was previously discussed, the GaAs nanowires presented in this study are passivated with the AlGaAs material during the MBE growth. Such AlGaAs shell effectively suppresses the recombination and the scattering of carriers on the surface of the GaAs core and thus substantially increases the PL yield [9, 135]. Since the AlGaAs shell has a large band gap energy than the one of the GaAs core, the core-shell geometry produces a radial heterostructure. Consequently, the following effects, which may strongly influence the PL emission, have to be examined: (a) incorporation of impurities into the GaAs core due to the diffusion and segregation of group-III elements during the passivation of nanowires; (b) radial confinement effect in GaAs–AlGaAs heterostructure nanowires.

The analysis of the core-shell structure of the model nanowires is performed by high-angle annular dark field (HAADF) scanning transmission electron microscopy (STEM) and spatially resolved energy dispersive X-ray spectroscopy (EDXS). For this purpose, another nanowire is selected after optical measurements and two cross-sections that are perpendicular to the wire axis are prepared for structural analysis. In Figure 4.10a, the cross-section HAADF STEM micrograph shows a hexagon-shaped section of the wire formed by the corresponding $\{110\}$ crystal facets. The core-shell structure is clearly resolved from the contrast. The darker region of the image corresponds to the Al-rich shell, while the brighter inner part to the GaAs core. The average diameter of the core and the corresponding thickness of the shell are estimated to be 85 ± 2 and 25 ± 2 nm, respectively.

The chemical composition is further elucidated by the spatially resolved EDXS measurements. Elemental maps that show the spatial distribution of As, Ga, and Al in the

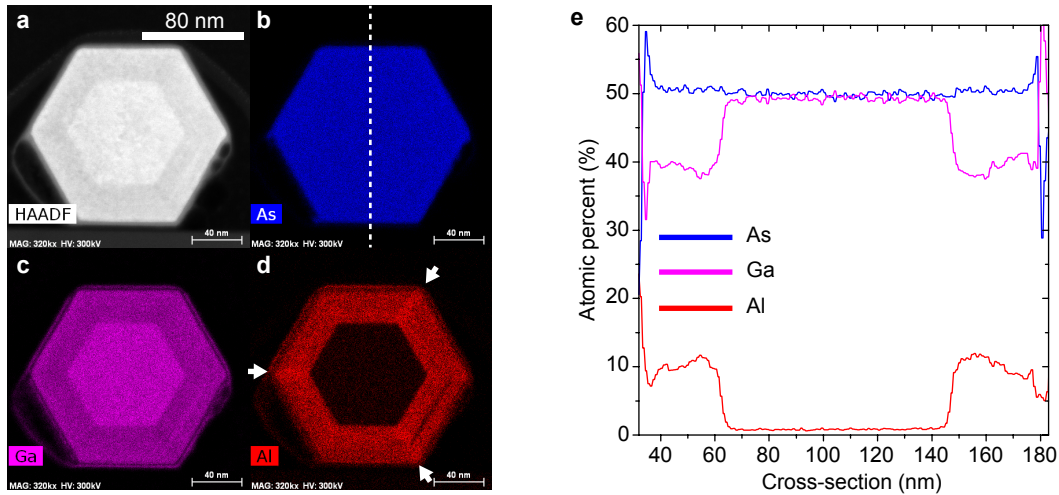


Figure 4.10: (a-d) HAADF STEM micrograph and elemental maps (EDXS maps) that show the spatial distribution of As, Ga, and Al of the GaAs-Al_{0.1}Ga_{0.9}As core-shell NW cross-section (provided by Dr. Andreas Graff, Fraunhofer Institute for Mechanics of Materials IWM). The scale bar of 80 nm applies to all maps. (b) Atomic percentage profiles of As, Ga, and Al obtained from the EDXS elemental maps along the cross-section marked by white dashed line.

cross-section of the GaAs-Al_xGa_{1-x}As core-shell nanowire, are presented in Figure 4.10b-d. The regions with a higher concentration of the respective element appear brighter in the map. All maps are measured within 200×200 nm² scan area with a spatial sampling of 0.24 nm/pixel. The data is corrected by the drift of the sample during the scan process. The contrast of the map in Figure 4.10c indicates the substitution of the group-III elements Ga and Al in the shell area, while the map in Figure 4.10d suggests the absence of aluminium in the nanowire core. The presented elemental maps reveal sharp interfaces between the GaAs core and the AlGaAs shell.

To emphasise these observations and estimate the Al concentration, the quantitative analysis of elemental maps is performed. The results are presented in Figure 4.10e. The atomic percentage profile of each element (As, Ga, Al) is extracted from the corresponding map along the line, as indicated in Figure 4.10b. The Al concentration of about 10% is in a good agreement with growth parameters. The Al concentration profile shows sharp interfaces between the AlGaAs shell and the GaAs core and the absence of Al in the body of the GaAs core within the experimental error. Therefore, the incorporation of aluminium is highly ambiguous and cannot be the reason for the observed blue-shifted PL emission. Additionally, a 3-fold Al-rich substructure along the corners of the hexagonal AlGaAs shell, where the Al-content is larger than in the body of the AlGaAs shell (white arrows), is observed. This observation is qualitatively similar to the spontaneous alloy composition ordering in GaAs–AlGaAs core-shell nanowires previously reported by several authors [144,145]. However, the PL emission associated with a local increase of the Al concentration in the AlGaAs shell is expected at higher energies than the emission energy discussed in the present study.

Having the structural and composition parameters, the estimation of electronic states of the 90-nm-wide GaAs quantum well in the Al_{0.1}Ga_{0.9}As matrix is performed. The resulting electron confinement energy is found to be about 0.6 meV, which is negligible in comparison

with the observed blue-shift of the PL emission.

Therefore, the results of HAADF STEM and EDXS measurements reveal a high quality of selected nanowire model structures for the investigation of the structure-property relationships. The anticipated incorporation of impurities into the GaAs core and the radial confinement effect in GaAs–AlGaAs heterostructures are not found in the present nanowires, and hence observed high-energy PL emission can not be attributed to these phenomena.

Summarising the discussion above, the PL emission at the energy that is larger than the band gap of bulk ZB GaAs is experimentally observed for the 1- μm -long zinc blende region of the single GaAs nanowire by the NSOM-TEM experimental approach. Several phenomena that are potentially responsible for such high-energy shift of the PL peak energy are discussed and experimentally verified within the current study. The origin of this shift so far was not fully understood. Summarising the results presented here and those from the literature, the following effects have to be considered and revised while addressing the PL emission in GaAs nanowires at the energy above the band gap of bulk ZB GaAs:

1. Band gap of wurtzite GaAs. Even though the exact value of the band gap energy of the WZ phase in GaAs nanowires is still discussed controversially, there are several reports suggesting its value to be above the band gap energy of ZB GaAs [25, 64, 146–148], which can be the reason for observed high-energy optical transitions. However, this hypothesis is not supported by the experimental results of the current study;
2. Quantum confinement in crystal-phase heterostructures. In the discussed region, the crystal structure is a virtually defect-free ZB phase, which can not explain the high-energy PL peak. In the previously reported results, the optical emission at the energy above the band gap of ZB gas was tentatively assigned to the radiative recombination of carriers confined in a crystal phase mixture [25]. However, there are also some experimental results suggesting that the emission from GaAs nanowires with a short-periodic mixture of crystal phases occurs at the energy below the band gap of ZB GaAs [22]. Since the effect of crystal-phase heterostructures on PL spectra of GaAs nanowires requires further investigations, it is considered in the following paragraphs;
3. Radial confinement effect. When the radius of GaAs nanowires approaches the exciton Bohr radius (~ 14 nm in GaAs), the effect of radial 2D confinement on optoelectronic properties has to be considered;
4. Effect of dopants on optoelectronic properties of GaAs nanowires. For instance, a possible incorporation of Al into the GaAs core during the passivation process will necessary influence optical properties of nanowires due to the increase of the band gap energy of the $\text{Al}_x\text{Ga}_{1-x}\text{As}$ alloy [149]. However, in this study the presence of aluminium in the GaAs core is not supported by the results of the material composition analysis;
5. Strain-induced changes in the band structure of GaAs nanowires. As it was previously reported, the uniaxial strain intentionally applied to zinc blende and wurtzite GaAs nanowires strongly influences their electronic band structure [150, 151]. Particularly, the applied tensile stress leads to a remarkable decrease of the band gap of the ZB GaAs nanowire. In turn, the increase of the band gap under the compressive stress was observed [150]. Therefore, the consideration of the stress in GaAs nanowires is important for the detailed discussion of their optoelectronic properties. There are possible internal and external sources of the strain. It is known, that the wurtzite lattice

parameter is slightly larger than the one of the zinc blende phase [152]. Thus, the ZB sections should be under a tensile strain in WZ dominated regions and, in turn, the WZ sections should be under a compressive strain in ZB dominated regions. This effect was confirmed by the characteristic shift of wave numbers in μ -Raman spectra [64, 153]. In addition, the single-nanowire measurements often require some physical support for the wire during experiments. GaAs nanowires are transferred from the growth substrate onto an external silicon substrate facilitating the single-nanowire measurements. It is assumed, that the main force holding wires on the Si flat surface is the van der Waals interactions that allow to fix nanowires during the whole experimental cycle [11]. Thus, different strains might be induced by the interaction of GaAs nanowires with the Si substrate due to the mismatch in their thermal expansion coefficients or the bending of long nanowires during the dispersion process. The strain-induced changes of optical properties were recently reported for GaN nanowires dispersed on the Si substrate [154]. However, in the particular case of GaAs nanowires on the Si substrate the mismatch in thermal expansion coefficients of these materials would lead rather to the low-energy shift, instead of the high-energy one [155, 156].

4.6.3 Carrier confinement in individual crystal-phase nanodomains

The discussion is focused now on the main issue of this work, which is the elucidation and the understanding of the structure-property relationship at the nanoscale in a mixture of zinc blende and wurtzite crystal phases. Several areas of the wire comprising a mixed crystal structure are identified by *a posteriori* performed high-resolution TEM analysis and indicated in Figure 4.6a as *ZB/WZ* regions, i.e. regions comprising ZB and WZ crystal-phase nanodomains of various orders and lateral extents. The NSOM-TEM strategy of measurements on one and the same wire allows an unambiguous assignment of the local PL spectra to the corresponding stacking of lattice planes. Of particular interest from both spectral and structural points of view is the region highlighted by the red rectangle in Figure 4.7a (right panel). Firstly, it shows several pronounced spectral signatures within a 1- μ m-long area. Secondly, TEM analysis reveals that the crystal structure of this region is the transition from the zinc blende region (*ZB* region on the left side) to the defect-free wurtzite region (*WZ* region on the right side) by a gradual increase of the wurtzite phase fraction. Therefore, this region with clearly identified crystal-phase nanodomains presents a promising model structure for in-depth discussions of structure-property correlations.

The diffraction-contrast TEM micrograph of the selected region is shown in Figure 4.11a. In Figure 4.11b, the spectral and spatial information of the same region is presented. The vertical axis indicates the emission energy. This axis is scaled to include all spectral features, while the horizontal axis shows the position of the corresponding local PL spectra along the nanowire. The colour code reveals the PL intensity distribution, which is spectrally and spatially resolved. Here, spatial coordinates correspond to those shown in Figure 4.7. From the spatial and spectral localisation of PL intensity, the 2D-map presented in Figure 4.11b can be divided into three emission segments with characteristic PL peak energies: (*A*) 1.501 eV, (*B*) gradually varying from 1.477 to 1.485 eV, and (*C*) \sim 1.492 eV.

The results of the structural analysis of the same region are plotted in Figure 4.11c, where the spatial axis is matched to that of the 2D spectral-spatial image in (b). The position of virtually defect-free *ZB* and *WZ* regions is indicated by the grey colour on the left side and the right side of the *ZB/WZ* region, respectively. A series of high-resolution

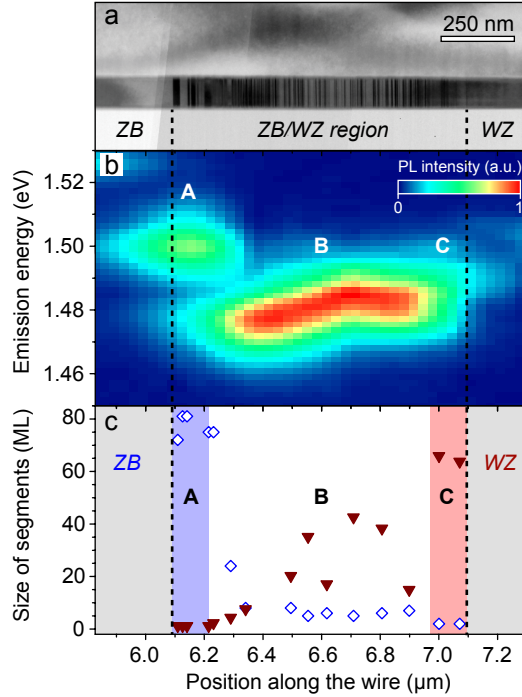


Figure 4.11: (a) Diffraction-contrast TEM overview of the selected region of the nanowire. (b) Spatial and spectral resolution of PL emission in the *ZB/WZ* region of the GaAs nanowire. The region is divided into three segments marked as A, B, and C, respectively. (b) Number of consecutive lattice planes of the largest zinc blende (open squares) and wurtzite segments (full symbols) in each high-resolution HAADF STEM micrograph acquired along the *ZB/WZ* region.

HAADF STEM micrographs is acquired along the *ZB/WZ* region. The previously described indexation scheme is used to assign each lattice plane to ZB or WZ phase and hence provide a quantitative information about the stacking sequence of lattice planes and the size of crystal-phase nanodomains with the lattice resolved accuracy. To describe spatial variations of individual spectral features as a function of the stacking sequence of lattice planes, the following concept of the direct correlation is selected. First, it is considered that the main recombination mechanism of excited carriers in the *ZB/WZ* region is a spatially indirect radiative recombination between electrons and holes localised in the ZB-type and WZ-type segments, respectively [22,64]. Such spatially indirect transitions are characteristic for the type-II heterostructures generated by the alternation of ZB and WZ phases along the nanowire axis (for instance, see Fig. 4.12d). As expected for a quantum confinement effect, the energy of optical transitions in a mixture of different phases depends on the width of quantum wells formed by thin enough ZB and WZ segments. Second, it is assumed that at low-temperatures and the moderate excitation power the majority of photoexcited carriers diffuse to quantum wells with lower energy states, which correspond to larger ZB and WZ nanodomains. Therefore, the largest ZB and WZ segments in a local mixture of crystal-phase nanodomains capture most of the carriers, which recombine there and give rise to PL bands at the corresponding energies. Thus, spatial variations of local near-field PL spectra in Figure 4.11b can be correlated with a width of the largest ZB and WZ segments within each STEM micrograph acquired along the *ZB/WZ* region.

For this purpose, the following quantitative structural information is plotted in Figure 4.11c. For each data point, the value on the horizontal axis indicates the spatial coordinate of the corresponding high-resolution HAADF STEM micrograph along the *ZB/WZ* region from which the structural information is derived. The vertical axis shows the size of the largest ZB and WZ nanodomains within each STEM micrograph. It is measured as a number of consecutive lattice planes: open symbols – zinc blende type (cubic, c) lattice planes, full symbols – wurtzite type (hexagonal, h) lattice planes. The size of each STEM image is 35 nm, which is comparable with the largest zinc blende and wurtzite segments observed in this region. Therefore, the experimental data in Figure 4.11c represent a spatially resolved information about the largest sequence of ZB-type and WZ-type lattice planes per period of 35 nm along the *ZB/WZ* region. Another concept commonly used to describe the crystal phase mixture is the variation of the wurtzite phase fraction [22]. In Figure 4.11c, the wurtzite phase fraction systematically increases moving from the left to the right border of the *ZB/WZ* region.

Now, the PL emission of segments *A*, *B*, and *C* can be compared to their lattice-plane-resolved crystal structure. The discussion is started from the segment *A*. The PL signal is spatially and spectrally well-resolved and represents the individual emission centre at the energy of 1.501 eV. The corresponding PL spectrum with a dominated emission band originated from the region *A* is shown in Figure 4.12a. The emission energy of this band is found to be constant within the segment *A*. Importantly, the spatial extension of this emission centre is found to be as small as 280 nm (the FWHM of the single 2D maximum along the spatial axis, see Fig. 4.11b), which is smaller than the carrier diffusion length in GaAs. This result suggests the efficient spatial localisation of excited carriers by some local confinement potential.

The crystal structure of the segment *A* is described by the formation of rotationally twined ZB segments of a thickness varying from 60 to 80 monolayers, i.e. from 20 to 26 nm (Fig. 4.11b, open symbols). According to the previously described indexation scheme, the lattice plane at the interface of rotational twins is assigned to the wurtzite-type one (Fig. 4.12b,c). Hence such inclusion produces the type-II heterostructure in a zinc blende matrix [22, 64]. The area that can be described by the concept of rotational twins only is emphasised by the blue colour and labeled with the letter *A* in Figure 4.11c. Remarkably, the position of the emission centre at the energy of 1.501 eV exactly coincides with this area. As shown in Figure 4.12d, such WZ inclusions in a ZB matrix produce thin barriers and quantum wells in the conduction (CB) and valence bands (VB), respectively. In this case, barriers in the conduction band are virtually transparent for electrons, while the corresponding quantum wells in the valence band may induce the localisation of holes. Taking into account the thickness of rotational twins, the resulting quantum wells can be assumed to be uncoupled. Therefore, the PL emission in the segment *A* is assigned to the recombination of excitons localised at the single unit of WZ structure, i.e. at single twin defects. The schematic of the band alignment and the recombination process in this segment is proposed in Figure 4.12d. The emission energy of 1.501 eV allows then the derivation of the localisation energy of excitons on a single twin-plane defect in comparison with the free exciton energy in ZB GaAs of 1.516 eV [70], which gives the value of about 15 meV.

Moving from the left to the right of the *ZB/WZ* region in Figure 4.11b, the PL peak at the energy of 1.501 eV (segment *A*) abruptly disappears, while the emergence of the new low-energy intensive PL band at 1.477 eV of the segment *B* is simultaneously observed. From the structural point of view, this process correlates with drastic changes of the crystal

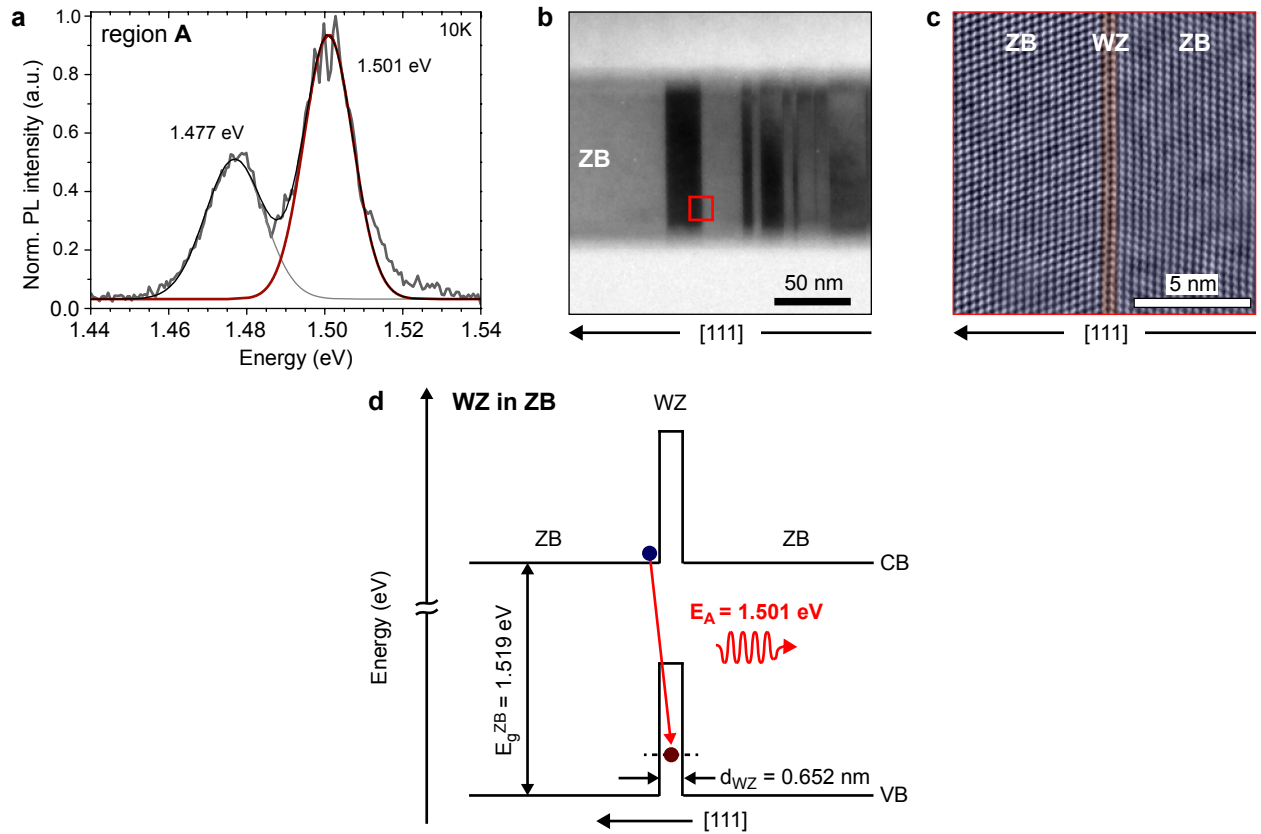


Figure 4.12: a) Low-temperature (10K) local PL spectrum selected from the region *A* indicated in Fig. 4.11b. The dominating PL band has the emission energy of 1.501 eV as defined by the Gaussian line fit (red solid line). b) Diffraction-contrast TEM image of the same region *A* (enlarged). The alternating dark and bright stripes correspond to rotationally twinned zinc blende segments, which have thicknesses on the order of 20 nm. c) Representative high-resolution HAADF STEM micrograph of the interface between two rotationally twinned ZB segments. The stacking order of [111] lattice planes at the interface produces the WZ inclusion with a thickness of 2 monolayers (ML), which corresponds to $d = 0.652 \text{ nm}$ in a GaAs nanowire. d) Schematic of a band alignment produced by the single 2ML-thick WZ disk in a ZB matrix and a radiative recombination path deduced from NSOM-TEM analysis.

structure. Particularly, the systematic inclusion of WZ segments with a larger number of consecutive wurtzite (hexagonal, h) lattice planes is observed (Fig. 4.11c, full symbols). Following the concept of a hole localisation in the wurtzite phase, thicker wurtzite segments introduce large quantum wells and hence could account for the lower recombination energy, as expected for a quantum confinement effect. The corresponding optical transitions are illustrated in Figure 4.13a (B1 transition). In addition, the continuous blue-shift of the PL peak energy from 1.477 to 1.485 eV is observed within the range from 6.3 to 6.7 μm of the ZB/WZ region (Fig. 4.11b). Here, the variation of the lattice planes stacking induces new optical transitions on such length scale that individual events of the emergence and the disappearance of individual PL bands cannot be spatially resolved by NSOM. This can be also explained by a higher density of crystal-phase nanodomains in this region and hence a

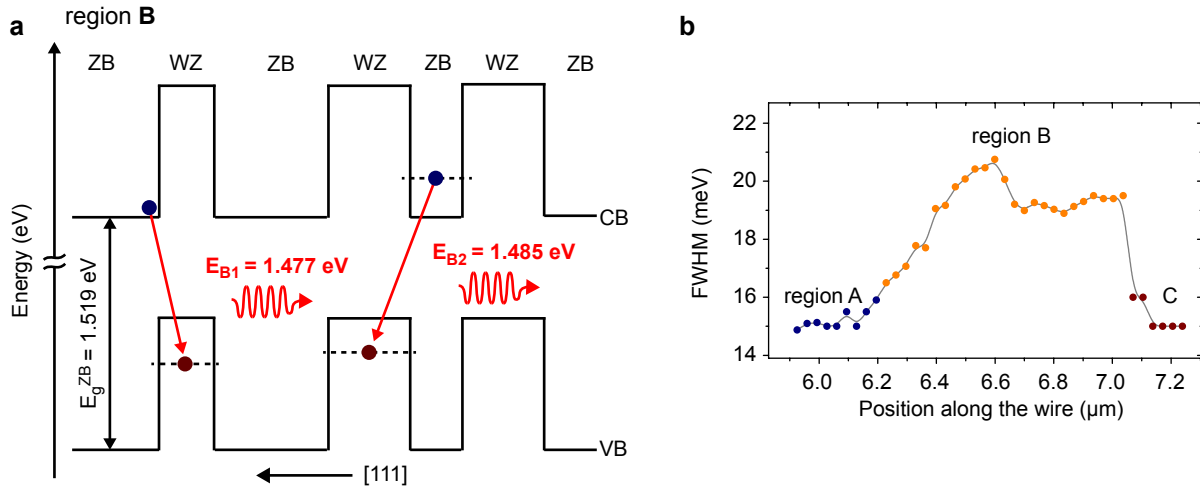


Figure 4.13: a) Schematic of a band alignment in the region *B* and the corresponding radiative recombination paths. b) Spatial variation of a full width at half maximum (FWHM) of local PL spectra of segments *A*, *B*, and *C*, respectively. The solid line is drawn to guide the eye.

larger variety of nanodomain sizes. Therefore, the large number of possible optical transitions is responsible for the significant broadening of the PL spectra in comparison with the segment *A*, as revealed in Figure 4.13b. Nevertheless, the clearly observed blue-shift of the PL peak energy on the length scale of about 400 nm can be correlated with changes of the local crystal structure. In the area from 6.3 to 6.7 μm , the thickness of WZ segments further increases (Fig. 4.11c, full symbols), that would be expected to lead to the red-shift instead of the blue-shift of the PL peak energy due to the increase of the quantum well width for holes. However, the crystal structure changes are not limited to the WZ inclusions, the substantial decrease of the thickness of ZB segments is found as well (Fig. 4.11c, open symbols). Therefore, the formation of relatively thin ZB segments in the WZ-dominated matrix is expected, in turn, to induce the confinement states for electrons with the energy slightly lifted from the bottom of the conduction band (Fig. 4.13a, B2 transition). If the impact of the ZB-size reduction is stronger in this region than the WZ-size extension on the carrier confinement energy, then the appearance of thin ZB segments will cause the emergence of higher energy PL bands that shift the entire PL spectrum. Alternatively, the high density of thin ZB and WZ segments in this region may lead to coupled quantum wells and a more complex recombination scheme, than shown in the simplified model in Fig. 4.13a. In this case, the evaluation of optical transitions will require additional calculations [61, 111].

In the final part of the *ZB/WZ* region (segment *C*), the emergence of a weak PL band at the energy of 1.492 eV dominating in emission spectra is observed, as it can be seen in Figure 4.11b. The representative PL spectrum from the region *C* is shown in Figure 4.14a. Simultaneously, the crystal structure changes to the almost pure wurtzite phase with a few inclusions of thin zinc blende segments (Fig. 4.11c). In this part (Fig. 4.14b,c), the size of the largest ZB inclusion is 3 ML, which corresponds to $d_{ZB} = 0.978 \text{ nm}$. The FWHM of this PL band is similar to that observed in the segment *A*, due to the reduced density of crystal-phase nanodomains (Fig. 4.13b). The inclusion of zinc blende segments in the wurtzite matrix produces quantum wells and barriers in the conduction and valence bands,

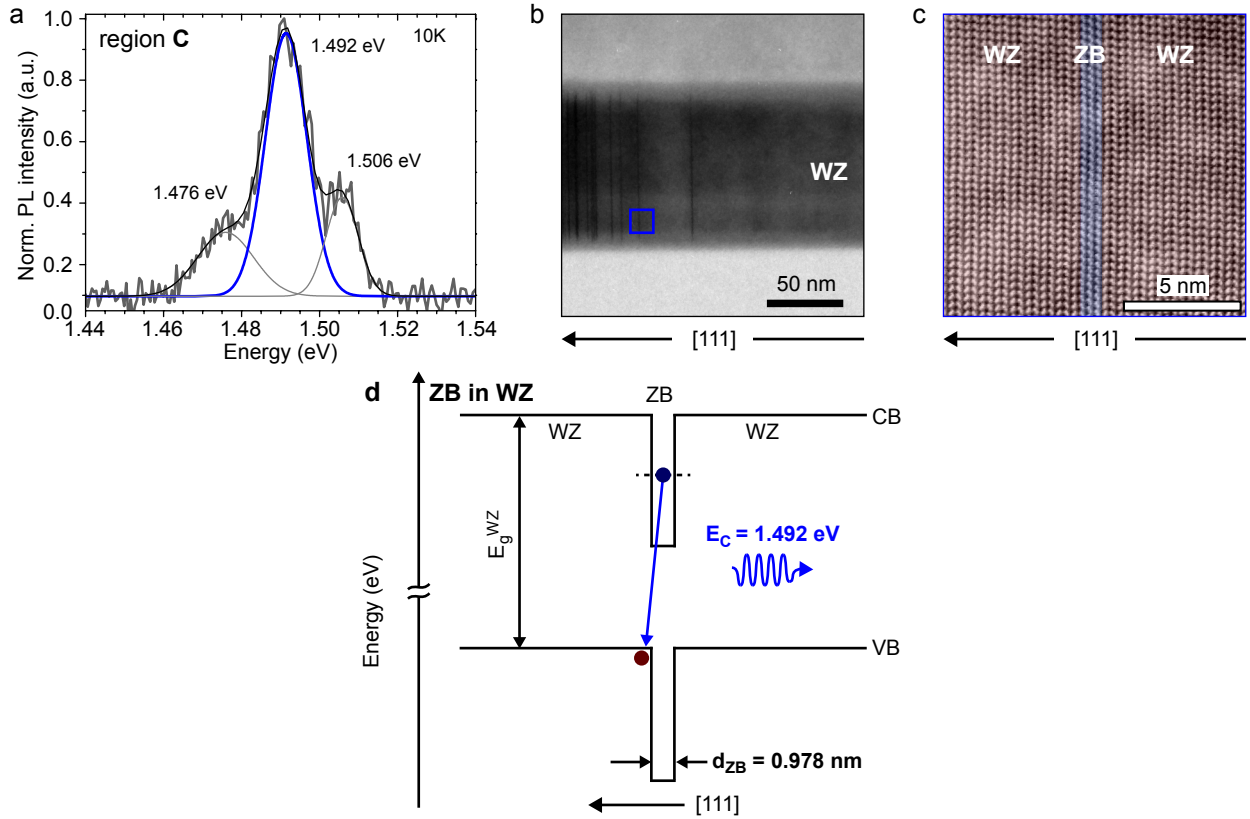


Figure 4.14: a) Low-temperature (10K) local PL spectrum selected from the region *C* indicated in Fig. 4.11b. The emission dominates at the energy of 1.492 eV, which is defined by the Gaussian line fit (blue solid line). b) Diffraction-contrast TEM image of the same region *C* (enlarged). The sharp dark vertical lines correspond to short inclusions of ZB segments in a WZ matrix. c) Representative high-resolution HAADF STEM micrograph of the 3 ML (i.e. $d = 0.978 \text{ nm}$) ZB disk in a WZ matrix, which is a dominating structure at the right end of the region *C*. d) Schematic of a band alignment produced by the single 3ML-thick ZB disk in a WZ matrix and the expected radiative recombination path deduced from NSOM-TEM analysis.

respectively (Fig. 4.14d). Therefore, this emission is assigned to the radiative recombination between holes from the top of the valence band in wurtzite segments and electrons localised in thin zinc blende quantum wells, as demonstrated in Figure 4.14d.

The proposed model of indirect optical transitions between electrons and holes localised in ZB and WZ segments (Figures 4.12, 4.13, 4.14, respectively), can be also supported by measurements of local PL spectra at various excitation intensities. The previously reported results on quantum wells with the staggered band alignment, e.g. GaAs/GaAsSb quantum wells formed by the alternation of the alloy composition, show the characteristic excitation power dependent blue-shift of the PL peak energy [157]. In Figure 4.15, the results of measurements of another nanowire from the same growth batch by NSOM are presented. The representative PL spectrum acquired at various excitation intensities at the same position of the near-field probe along the wire is plotted in Figure 4.15a. Its PL peak position is within the energy range of optical transitions observed in the *ZB/WZ* region (Fig. 4.11a).

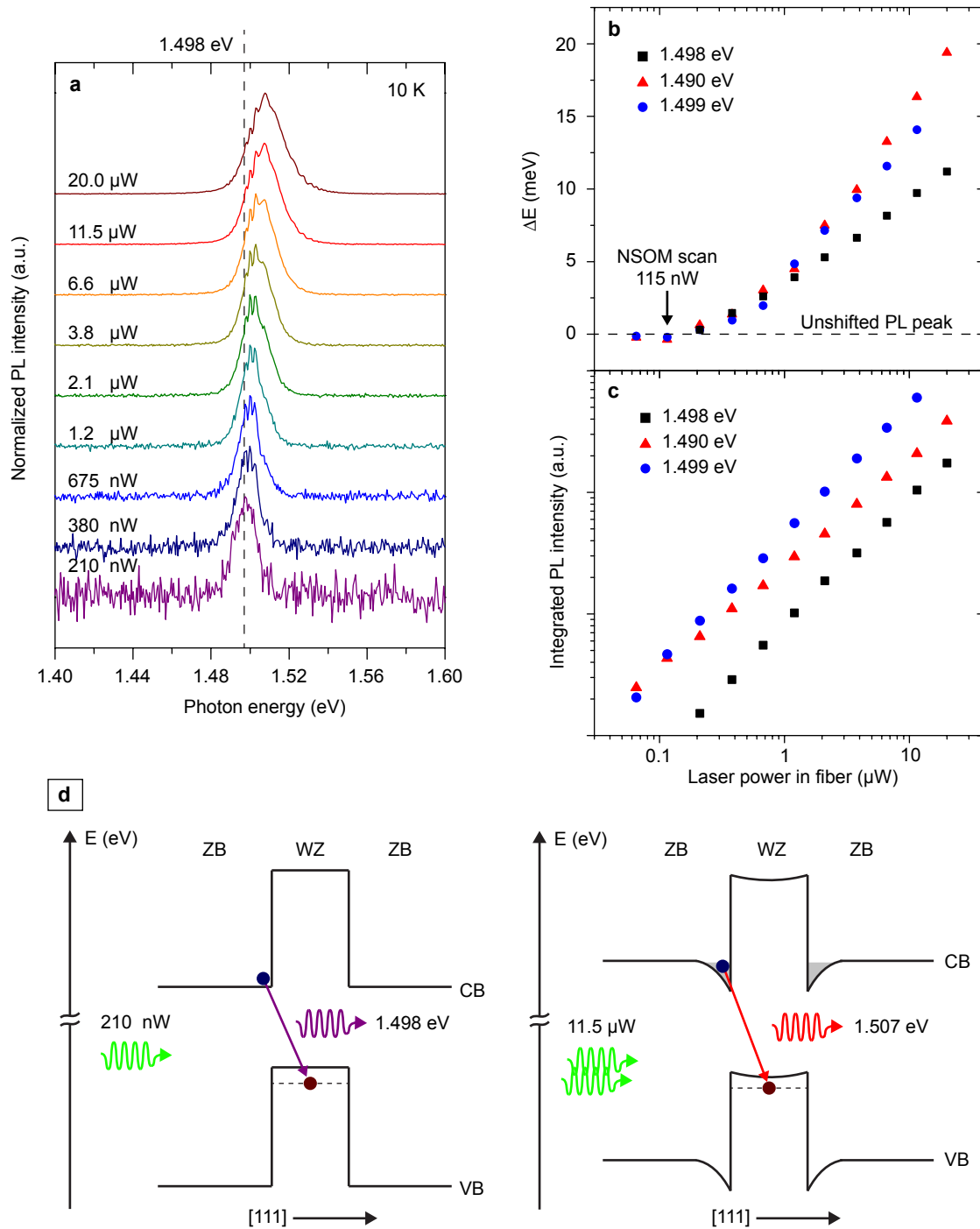


Figure 4.15: (a) Local PL spectrum of the wire under different excitation powers measured at 10K. (b) Shift of the PL peak energy as a function of the excitation intensity. (c) Integrated PL intensity as a function of the excitation power. (d) Schematic of the band alignment in a GaAs nanowire with a WZ segment in a ZB matrix and the corresponding radiative recombination through the spatially indirect transition: *left* – at the low excitation intensity of 210 nW, *right* – at the high excitation intensity of 11.5 μW .

In Figure 4.15a, the PL peak position shifts to higher energies with an increasing of the laser power coupled to the optical fiber. The excitation power dependence of three PL bands of similar energies selected along the single wire are plotted in Figure 4.15b,c. At low excitation intensities, the shift of PL peak energy is negligible (Fig. 4.15b). According to these results, the excitation power used for the NSOM scan (115 nW) of the previously discussed nanowire excludes significant laser-induced perturbations of local PL spectra. At high excitation intensities, all PL peaks are blue-shifted with a slight variation of the dependence on the excitation power. Simultaneously, the PL peak intensity reveals its linear increase as a function of the excitation intensity (Fig. 4.15c).

Since the excitation power dependence of the PL peak energy in Figure 4.15b reveals at least two slopes, it can be considered that some different mechanisms work at different laser intensities. Such spectral behaviour was previously reported for rotationally twinned InP nanowire heterostructures [111]. The dependence of the PL peak energy on the excitation power can be explained by two mechanisms by analogy with quantum wells with the staggered band alignment [111]. The type-II band alignment, assumed for ZB/WZ crystal-phase heterostructures, leads to the spatial separation of electrons and holes across the heterojunction. At low excitation intensities, the spatial charge separation induces an electric field across the heterointerface and causes a corresponding band bending. This, in turn, increases the PL peak energy due to the shift of electron and hole energy levels via the Stark effect. At high excitation intensities, the low-energy levels become saturated. The excited carriers begin to populate the higher energy levels, leading to high-energy optical transitions. Therefore, in the current study, the blue-shift of local PL spectra of GaAs nanowires as a function of the excitation power is in a qualitative agreement with the proposed model of indirect optical transitions due to the staggered band alignment between zinc blende and wurtzite crystal-phase nanodomains.

4.7 Summary

In this chapter, the spectral imaging in the near-infrared region with the nanometer scale resolution of a mixture of zinc blende and wurtzite crystal phases in GaAs nanowires was demonstrated. As a result, several PL bands, whose peak energies vary within the range of 24 meV at the most, are spatially discriminated on the length of 1 μm . Importantly, the lateral extension of some local PL emission bands is found to be as small as 280 nm. This result suggests the efficient spatial localisation of excited carriers in polytypic nanowire structures and supports the expected high spatial resolution provided by NSOM spectral imaging. By applying the *experimental protocol*, which combines near-field spectral imaging and transmission electron microscopy measurements performed on one and the same GaAs nanowire, the well-resolved local photoluminescence peaks were assigned to individual zinc blende and wurtzite disks. Moreover, the crystal structure of these crystal-phase disks was defined with the lattice-resolved accuracy. The degree of confinement of excited carriers, which is controlled by the thickness of these crystal-phase nanodomains, can be described now, since the corresponding energies of optical transitions are known. Results of the present study provide a better insight into the structure-property relationships in GaAs nanowires. They can serve to refine or possibly revise previous theoretical and experimental findings on optoelectronic properties of crystal-phase semiconductor heterostructures.

Outlook

In order to clarify the origin of the photoluminescence emission at energies above the band gap of ZB GaAs, which was discussed in the first part of this chapter, the following research steps are undertaken. By using μ -photoluminescence measurements, additional GaAs nanowires from the same growth batch, which exhibit high-energy emission peaks, are preselected. Near-field spectral imaging allows to identify the exact position of the corresponding emission centres along these nanowires. At the next step, structural analysis of these regions by transmission electron microscopy is expected to reveal the dependence of high-energy photoluminescence peaks on the local crystal structure.

Chapter 5

Effects of beryllium doping on local optical properties of GaAs nanowires

5.1 Introduction

5.1.1 Doping of III–V semiconductor nanowires

Nanowires grown directly on Si wafers [6] hold a great promise for the integration of optoelectronic properties of III–V semiconductor materials with the mainstream silicon technology. The rapidly growing number of publications on prototype nanowire-based photonic [4] and electronic [15, 17, 158] devices confirms technological expectations towards the developing of advanced nanowire-based one-dimensional electronics [10, 11, 159].

The control over electrical properties of semiconductor nanowires is a prerequisite to their application in various electronic devices. Therefore, the ability to control the conductivity and the carrier type of nanowires by introducing *n*-type or *p*-type dopants is essential. This, in turn, requires the understanding of several cornerstone issues such as: (a) mechanisms of a dopant incorporation into nanowires [160, 161], (b) effects of dopants on a growth process and a morphology of nanowires [51, 162], (c) the evaluation of a carrier concentration, a spatial distribution and their effect on optoelectronic properties of nanowires [163–165]. Fundamental challenges and important achievements in the field of doping of semiconductor nanowires were previously reviewed in the work of J. Wallentin and T. Borgström [67].

The vapour-liquid-solid (VLS) growth mechanism is commonly applied for the fabrication of semiconductor nanowires [166]. Dopants are typically introduced during the growth process. The bottom-up growth conditions and the one-dimensional nature of wires result in the *in situ* incorporation of impurities, which is expected to be different from that known for planar materials. Therefore, incorporation paths in nanowires have to be defined to receive a control on the doping efficiency and the spatial distribution of impurities. In order to substantially improve our understanding of doping mechanisms in semiconductor nanowires, the ability to probe the carrier concentration introduced by impurities, their spatial distribution and the overall effect on optoelectronic properties is required. The nanoscale dimension of nanowires makes it difficult to probe the carrier concentration and the mobility applying standard Hall measurements. However, the electrical measurements of single nanowires performed by using special 2-probe and 4-probe contacted NW-devices are commonly used. Such measurements allow to reveal the efficiency of the dopants incorporation and evaluate the effective carrier concentrations in nanowires [161, 167]. Moreover, the dopant profile

along free-standing nanowires was successfully resolved by resistance measurements using a multi-tip scanning tunnelling microscope [165]. For the comprehensive analysis of doping, electrical measurements are often combined with other characterisation techniques, e.g. Raman spectroscopy [168]. However, most of the electrical measurements require the fabrication of metallic contacts and do not provide the nanoscale resolution of doping profiles along nanowires. In order to provide more precise measurements, atomic probe tomography is considered as a promising technique for high-resolution analytical imaging of dopants in nanowires [169,170].

5.1.2 Impact of doping on nanowire properties

As it was previously discussed, the III–V nanowires may exhibit a crystal structure, which is different from the crystal structure observed in the bulk form of the corresponding material. In *Chapter 4*, the strong influence of the alternation of ZB and WZ crystal phases along the undoped GaAs nanowire on its optoelectronic properties was demonstrated and thoroughly discussed. Interestingly, the incorporation of dopants into III–V nanowires may have also a substantial impact on the crystal phase formation [51,55] and the morphology [160,162] of nanowires. Thereby, doping can be used as an additional tool to gain a better control over the crystal phases formation. Indeed, under certain growth conditions the introduction of impurities leads to the formation of twin planes, which have a constant spacing along the wire. They present a new class of so-called twinning superlattices (TSL) and provide opportunities for the electronic band structure engineering [51,56]. The ability to control periodic arrangements of TSL was reported for different III–V NWs [47,51,55]. Due to the atomically sharp interfaces of these TSL, one may expect that such crystal-phase nanostructures exhibit optical properties, which are not perturbed by the alloy composition fluctuations at the interfaces, which is the case for heterostructures obtained with semiconductors of a different composition. However, doping necessarily affects optical and electronic properties of nanowires. Impurities might obscure the advantages resulting from the high crystalline quality. Thus, a comprehensive study of the joint contribution of these competitive parameters (the crystal structure and doping) to optoelectronic properties of III–V nanowires is essential. To this end, optical characterisation methods have certain advantages. They are sensitive to changes of optoelectronic properties of nanowires induced by both variations of the crystal phase structure and the incorporation of impurities. Indeed, photoluminescence measurements performed on GaAs nanowires are capable to provide information about the effect of dopants on the energy band structure and the spatial distribution of impurities along the nanowire length [163,164,171]. Moreover, the carrier concentration can be quantitatively derived by a comparison of spectral characteristics of nanowires with those characteristics obtained from bulk reference samples with the same crystalline structure. However, the impact of the local crystal phase structure and the carrier concentration in most of III–V nanowires has to be carefully disentangled. First, this requires to achieve a high spatial resolution of spectral characteristics of individual nanowires. The nanoscale free-carrier profiling of InP nanowires with a doping modulation was previously proposed by applying an infrared scattering-type scanning near-field optical microscope [172]. Second, the local optical spectra have to be clearly assigned to a certain crystalline structure to perform a direct comparison with bulk reference samples, which may not exist in some crystal phases. Therefore, the previously described *experimental protocol* of the complementary NSOM and TEM analysis of individual nanostructures is perfectly suitable to address the aforementioned issues.

In this chapter, subwavelength-resolution low-temperature near-field photoluminescence spectra and transmission electron microscopy images of the very same heavily beryllium (Be) doped GaAs–AlGaAs core-shell nanowires are analysed. The pronounced spatial variations of spectral characteristics along the length of the wire are clearly resolved. By correlating optical and TEM analysis, the transformations of local photoluminescence spectra induced by joint contributions of the crystal structure inhomogeneity and the Be doping are deduced.

5.2 Be-doped GaAs–AlGaAs core-shell nanowires

5.2.1 Growth and *in situ* beryllium doping

To study structure-property correlations in the presence of dopants, heavily beryllium-doped GaAs–AlGaAs core-shell nanowires grown directly on a Si (111) substrate were selected as a model system. The nanowire sample was grown and provided by a group of Dr. George Cirlin from *St. Petersburg Academic University RAS (St. Petersburg)* as a part of our collaboration on this topic [173]. Beryllium was taken as the most commonly used dopant that defines the *p*-type conductivity in GaAs [174]. These wires were fabricated by a Ga-assisted growth technique using the commercial EP-1203 molecular beam epitaxy (MBE) system. The Si (111) substrate was first annealed in a vacuum at 660°C in order to partially desorb the oxide layer from its surface. Then, the temperature of the substrate was reduced to 610°C and a flux of Ga was supplied to the surface for 60 s. The latter induces the formation of Ga droplets on the Si substrate, i.e. catalyst nanoparticles. Then, a flux of As was added by opening the corresponding source to initiate the growth of GaAs nanowires. The deposition rate was held at 1 monolayer (ML)/s at the As₄/Ga fluxes ratio of 0.5. Simultaneously, thermally evaporated beryllium was supplied in order to perform an *in situ p*-type doping of GaAs nanowires. The temperature of the beryllium source was set to 860°C. The selected temperature of the Be cell corresponds to a doping level of $\sim 5 \times 10^{19} \text{ cm}^{-3}$, which was estimated for the case of planar GaAs layers grown on a GaAs(111)B substrate by the Van der Pauw measurements. The growth of nanowires was completed within 15 min. Afterwards, the procedure was interrupted and the temperature of the sample was reduced to 550°C. To produce a core-shell structure, the growth of the Al_{0.3}Ga_{0.7}As shell was then performed within 5 min. The GaAs–AlGaAs core-shell nanowires are also referred to as GaAs nanowires through this chapter, unless the core-shell geometry is needed to be emphasised.

5.2.2 Morphology

In Figure 5.1a, a side-view scanning electron microscopy (SEM) image of as-grown nanowires is presented. As it can be seen from the SEM micrograph, these nanowires have a typical length L of 2–5 μm and an average diameter d of 200 nm. Nanowires form a high density array on the Si substrate. The strong variation of the nanowires geometry suggests the corresponding fluctuation of their structural and optical properties within the ensemble. Therefore, single-nanowire measurements are particularly important for a direct structure-property correlation. Following the *experimental protocol*¹, nanowires are transferred from the growth substrate to the Si substrate with alignment marks by the ultra-sonication and drop-casting techniques (Fig. 5.1b). As it was previously mentioned, such substrate facilitates both NSOM and TEM measurements on the same wires. Four nanowires that have

¹For details about the *experimental protocol* the reader is referred to Chapter 3.

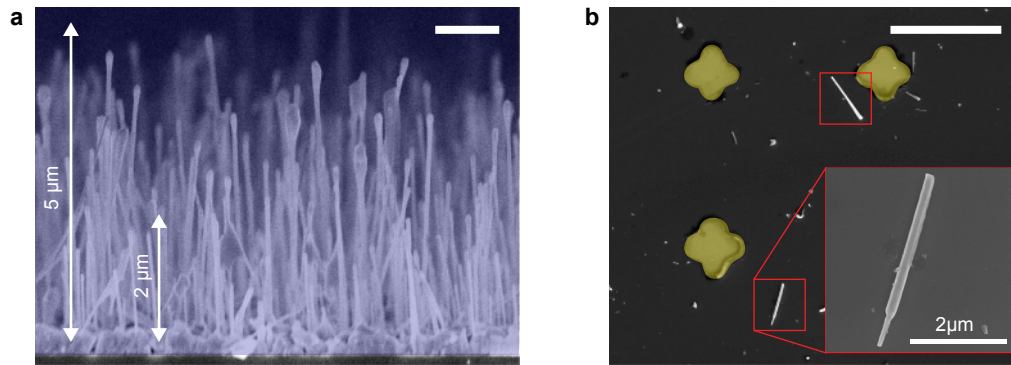


Figure 5.1: (a) Side-view SEM micrograph of as-grown self-catalysed Beryllium-doped GaAs–AlGaAs core-shell nanowires grown directly on the Si (111) substrate. The wires have an average diameter d of about 200 nm. Their length L varies from 2 to 5 μm . The scale bar is 1 μm . (b) Top-view SEM micrograph of nanowires transferred by ultrasonication and drop-casting techniques onto the Si substrate with alignment marks (yellow pseudo-colour). This approach allows to perform both NSOM and TEM measurements on one and the same wire. The scale bar is 10 μm . Inset: a nanowire selected for NSOM-TEM analysis.

a full contact to the Si surface are preselected for correlated analysis. They are spatially well-isolated from other NWs. The average length of preselected wires L is about 4 μm .

5.3 Experimental details

Protocol of the structure-property correlation

Details of the NSOM-TEM strategy are described in *Chapter 3*. In brief, after the preparation of the sample for single-nanowire measurements (Fig. 5.1b), the selected nanowires are studied optically by the low-temperature NSOM providing a high spatially resolved spectroscopic information. Following optical measurements, exactly the same nanowires are prepared for structural analysis. Particularly, using the focused ion beam (FIB) milling, selected nanowires are extracted from the Si substrate. Afterwards, the cross-section TEM samples that contain the nanowires of interest are created. TEM measurements provide atomically resolved maps of crystal phase mixtures along individual nanowires, which can be then directly correlated with a spectroscopic information obtained from the same wires before.

5.4 Near-field spectral imaging and structural analysis

In Figure 5.2a, a spectrally integrated near-field map of the total PL intensity of the scan area of $4 \times 4 \mu\text{m}^2$, which contains the nanowire of interest, is presented. At every pixel of the image, the PL spectrum is integrated in the entire detection energy range. Then, the resulting value is plotted as a function of the position of the near-field probe. The topography image of this wire, which is simultaneously recorded during the same scan process by shear force microscopy, is shown in Figure 5.2b. In this figure, the topography image is overlaid

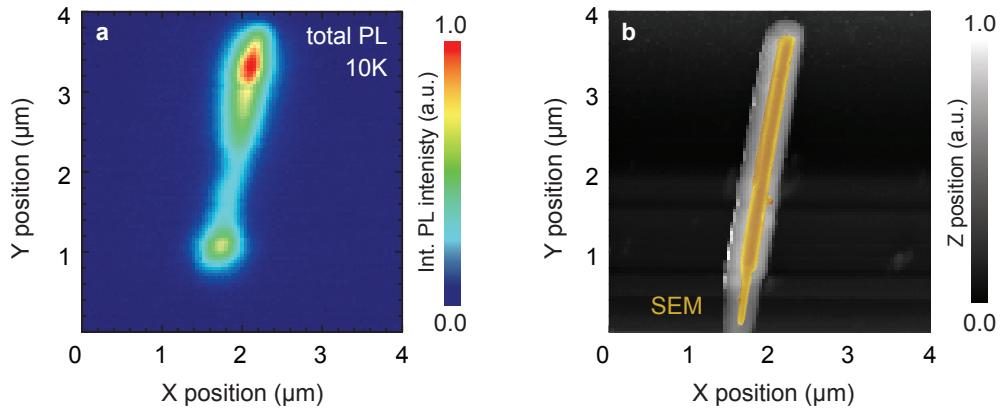


Figure 5.2: (a) Two-dimensional map of the total near-field PL intensity of the single nanowire acquired at a temperature of 10 K in the region indicated by the inset in Fig. 5.1b. A full near-field PL spectrum is recorded in the energy range between 1.245 and 1.870 eV at every pixel of the image with an integration time of 500 ms per spectrum. (b) Topography image recorded simultaneously during the scan process by shear force microscopy. For comparison, an SEM micrograph of the same NW, shown in the yellow pseudo-colour, is overlaid with the topography image.

with a scanning electron microscopy (SEM) micrograph (shown in the yellow pseudo-colour). It indicates that the topography image indeed reflects the actual shape of the nanowire. As it was previously mentioned, the combination of optical and topographical maps simultaneously provided by NSOM allows to reveal the spatial origin of different PL emission features along the wire with a high accuracy.

In Figure 5.2a, two pronounced emission maxima at the top and bottom parts of the nanowire are clearly seen. The analysis of topographical images allows a tentative assignment of such intensity distribution profile to intrinsic optical properties of the wire rather than to an experimental artefact, which is induced by the distance variation between the near-field probe and the sample surface. Indeed, as it will be shown by means of the direct correlation with TEM analysis, two maxima in the near-field PL map are found in comparatively large pure ZB-type regions of the wire, which act as carrier traps.

For a spatially resolved spectroscopic characterisation, local near-field PL spectra acquired at 10 K are selected from pixels along the wire axis and plotted in Figure 5.3a. These PL spectra reveal a distinct spatial variation of spectral characteristics along the nanowire. Specifically, the spectral shift of the most intensive emission band around the energy of 1.48 eV and the emergence of new weaker sidebands in the top and bottom regions of the wire are observed.

The diffraction-contrast TEM map of the same NW studied by NSOM is the inset in Figure 5.3a. Its scale matches to the spatial axis of the spectroscopic scan. Clearly, the PL emission is suppressed in the thin region at the very bottom. Probably, the bottom part has not been passivated by an AlGaAs shell. Therefore, the PL emission is quenched due to the strong nonradiative recombination at the NW surface typical for bare GaAs NWs, which is in line with Ref. [9] and [135]. The rest of the wire can be visually divided into three regions, a bottom (1), a centre (2), and a top region (3). Representative PL spectra from these regions, indicated by arrows in Figure 5.3a, are plotted in Figure 5.3b. All spectra show an intense,

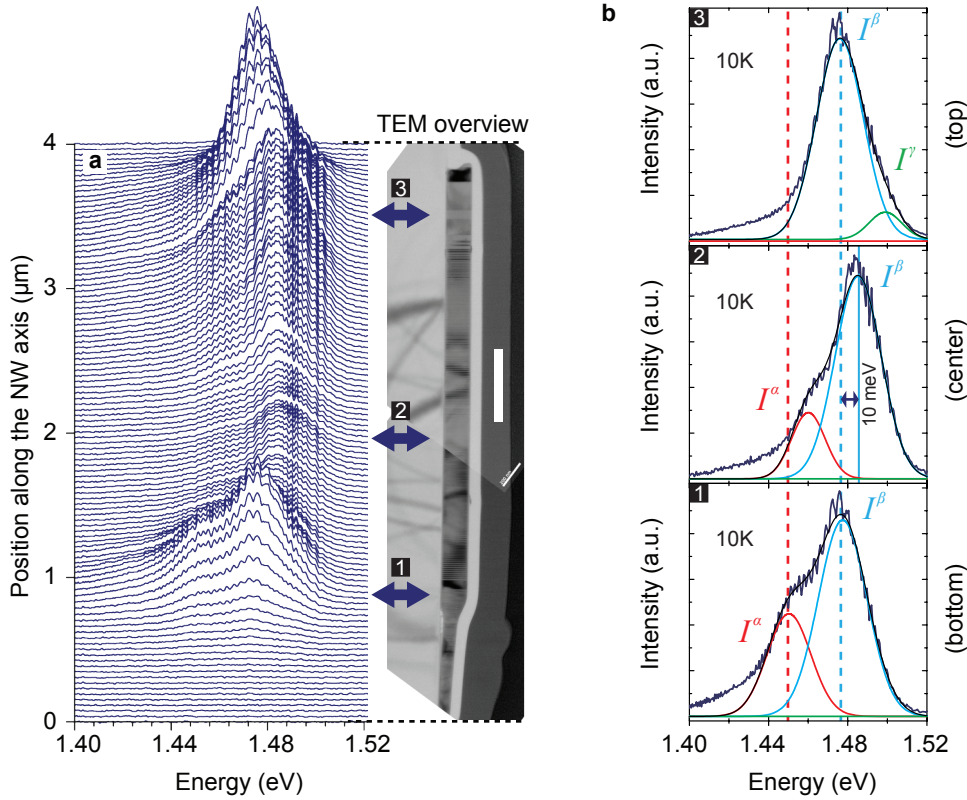


Figure 5.3: (a) Selected near-field PL spectra along the axis of the single NW shown in Fig. 5.2. The right inset shows a diffraction-contrast TEM overview of the corresponding nanowire. The scale bar of 500 nm applies to both the spatial axis of the spectral-spatial map and the TEM image. This facilitates a direct correlation between TEM structural analysis and the local near-field spectral response. (b) Selected normalised local near-field PL spectra from the regions marked by arrows in the inset of Fig. 5.3a. The red I^α , blue I^β , and green I^γ curves show the decomposition of the PL spectra into three Gaussian emission bands.

approximately Gaussian-shaped emission peak around 1.48 eV, labeled I^β , and a broad low-energy emission shoulder. In addition, PL spectra in the bottom and centre regions reveal a second, weaker low-energy emission band at around 1.45 eV, labeled I^α . Instead, PL spectra in the top region show a high-energy peak I^γ at about 1.50 eV. As seen in Figure 5.3b, all near-field spectra at energies above 1.43 eV are reasonably well described by the sum of three Gaussian curves. The spectral decomposition was performed for all PL spectra in Figure 5.3a. The results of the fitting of the experimental data provide a map of the peak energy, the spectral width, and the relative intensity of each of these three bands along the NW axis. The PL peak energy of I^α and I^β bands is plotted in Figure 5.5a as a function of a position along the wire length. Interestingly, a pronounced, spatially homogeneous blue shift of the I^β band is observed in the central part of this specific NW.

Such spectral changes in PL spectra of Be-doped GaAs nanowires are expected to arise either from a fluctuation of the doping level or the crystal structure, e.g. the alternation of ZB and WZ crystal phases. Therefore, their impacts on optoelectronic properties of nanowires have to be carefully disentangled. First of all, to address the microscopic origin of PL bands derived from spectral imaging, the quantitative TEM analysis of the crystal

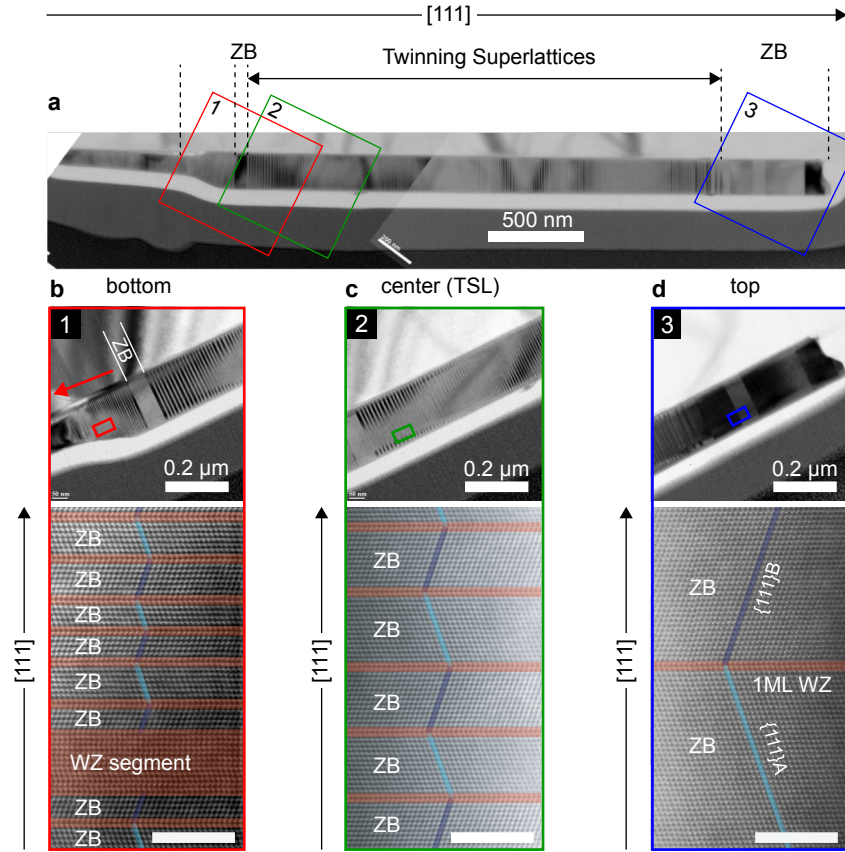


Figure 5.4: Map of the crystal phase structure of the single Be-doped GaAs nanowire: (a) Complete TEM overview of the wire at a low magnification. The black dashed lines visually separate the regions of the wire with the distinctly different crystal structure. (b-d) Upper panels: enlarged TEM micrographs of the NW from regions highlighted in (a). The pronounced bright and dark stripes correspond to the rotational twins of the zinc blende phase [138]; Lower panels: The corresponding atomic resolution STEM images that show the density and the periodicity of rotational twin interfaces indicated by the red colour. The light and dark blue lines emphasise the rotation of atomic arrangements around the [111] direction of adjacent twinned ZB segments. Scale bars of all STEM images are 5 nm.

structure of the entire NW is performed. Following the *experimental protocol* of the nanoscale structure-property correlation, the same nanowire studied optically is prepared for structural analysis. The overlapping TEM and STEM images were analysed to characterise the crystal structure with a lattice-resolved accuracy. The diffraction-contrast TEM overview is plotted in Figure 5.4a. Regions with a particular crystal structure are visually separated by the black dashed lines. In Figure 5.4b-d, representative enlarged TEM micrographs are shown for three regions of the wire, which are highlighted in Figure 5.3a. In the corresponding high-resolution STEM images (Fig. 5.4b-d, lower panel), each bright spot represents a pair of Ga and As atoms. Interestingly, distinctly different crystal structure segments are found in the top, center, and bottom regions of the wire, which were previously distinguished in the spectral map. In the bottom region (Fig. 5.4b, 1), the inclusion of a large defect-free ZB-type segment is observed, as emphasised by the white solid lines. The lateral extension of this segment is about 50 nm, which is larger than the exciton Bohr radius in GaAs (~ 14 nm).

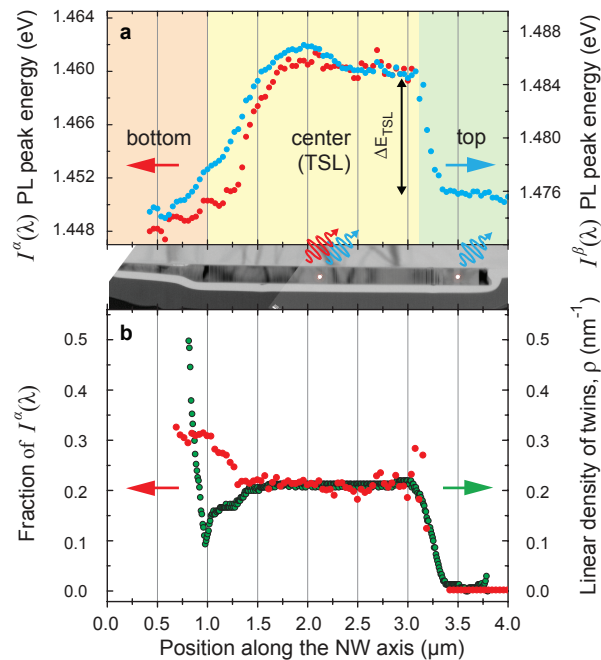


Figure 5.5: (a) Spatial variation of the peak energies of the I^α (red circles) and I^β (blue circles) emission peaks along the nanowire axis. (b) Relative fraction of the I^α emission to the total PL emission in different parts of the NW (red circles). Variation of the linear density of twin planes along the NW axis (green circles). The twin density is spatially averaged over a spatial window of 150 nm, which is comparable to the NSOM resolution.

Below the defect-free ZB-type inclusion, the conically shaped segment shows a ZB phase crystal structure with a high density of rotational twins and stacking faults. In the high-resolution lattice plane image, the twin interfaces are marked by the red colour (Fig. 5.4b, lower panel). A detailed study of the atomic stacking at the twin boundary reveals that it actually represents a single unit of the WZ structure. Moving from the upper base to the apex of this conical segment, as indicated by the red arrow in Figure 5.4b, the density of twins gradually increases. Moreover, additional larger segments of the WZ phase are formed at the bottom end of the NW. A similar formation of large WZ-type nanodomains with the increase of the twin plane density has also been reported by Heiss *et al.* [22]. The similar effect was observed in our study on undoped GaAs nanowires².

The center region of the wire, which starts above the ZB segment, is of particular interest (Fig. 5.4c). Here, we find rotationally twinned ZB segments with a virtually constant spacing between adjacent twin planes. Therefore, this center region is assigned to a twinning superlattice (TSL), which extends over a length of more than 2 μm . Using the atomic resolution STEM images, the number of lattice planes between adjacent twin planes can be counted (Fig. 5.4c, low panel). Results of quantitative analysis of TEM micrographs are shown in Figure 5.5b. The linear density of twin interfaces is plotted (green circles) as a function of the position along the NW axis and averaged at each position over a spatial window of 150 nm, which is comparable to the NSOM resolution. In the left part of the TSL region, for positions along the NW axis from 1.0 to 1.5 μm , an average size of rotationally twinned ZB

²For details the reader is referred to Chapter 4.

segments is found to be about 19 ± 3 $\{111\}$ lattice planes per a segment, which corresponds to a twin planes density of $\rho = 0.161 \text{ nm}^{-1}$. The distance between adjacent lattice planes in $[111]$ direction was defined as $a/\sqrt{3}$, where $a = 5.65 \text{ \AA}$ is the lattice constant of GaAs. In the middle part of the TSL region, the twin planes periodicity of about 15 ± 3 lattice planes is found to be virtually constant, providing the density of $\rho = 0.204 \text{ nm}^{-1}$. At the end of this long-range periodic twinning superlattice, at the position of around of $3.1 \mu\text{m}$, there is a quite abrupt transition to the top ZB region (Fig. 5.4d), which occurs within less than 20 nm. Thus, the TSL region is surrounded by two ZB segments, one at the bottom, followed by the conical segment with a high density of twin defects (Fig. 5.4b), and one at the top region of the wire (Fig. 5.4d). So far, such clear indication of a twinning superlattice formation has only been observed for this specific NW. This makes it particularly attractive for an in-depth investigation of correlations between its crystal structure and optical properties.

5.5 Be-doping induced band gap reduction

5.5.1 Photoluminescence spectra of Be-doped zinc blende GaAs

In order to define the structure-property relationships in the TSL region, the effect of the high level of beryllium dopants on local PL spectra has to be clearly resolved. The structural characterisation now allows the assignment of the local optical spectra demonstrated in Figure 5.3. Particularly, the local PL spectra resolved from regions with the virtually defect-free ZB crystal structure can be used to evaluate the impact of the beryllium incorporation on optoelectronic properties of GaAs nanowires. Therefore, the analysis is started from the top region of the wire, where the large segment of the ZB type structure with a negligibly low density of defects is observed. The emission is dominated by the I^β band (Fig. 5.3b, top). Its emission peak with a full width at half maximum (FWHM) of about 26 meV is centred at the energy of 1.476 eV, which is independent of the exact position along the ZB region (Fig. 5.5a). Such constant emission energy is in a good agreement with negligible variations of the crystal structure. Therefore, local PL spectra from the ZB region can be directly compared with published data on PL spectra of beryllium doped bulk GaAs to evaluate the carrier concentration in nanowires provided by the *in situ* doping.

The emission energy of the most intensive PL band I^β in the ZB segment is significantly red-shifted with respect to the emission energy of excitonic transitions in ZB-type undoped bulk GaAs at 10 K [70]. In addition, a weak high-energy shoulder I^γ is resolved in the spectra. It is assumed that the observed PL emission arises from the changes in the energy band structure induced by the incorporation of impurities, since this region of the wire does not exhibit the significant crystal structure variations. Indeed, the experimental PL spectra of heavily p -doped bulk ZB GaAs reported in previous studies [175, 176] are found to be similar to the near-field PL spectra selected from the ZB region of Be-doped GaAs nanowires. Thus, the observed red-shift of the I^β band can be assigned to a band gap shrinkage in heavily p -doped GaAs due to the exchange and the correlation in the hole system [175]. The qualitative comparison with optical transitions in bulk p -doped GaAs [175] allows to suggest the following recombination mechanism in ZB segments of the Be-doped GaAs nanowire. The main emission, I^β , reflects direct, \mathbf{k} -conserving optical transitions between the minimum of the conduction band and the top of the valence band. In turn, the high energy shoulder, I^γ , originates from indirect, non- \mathbf{k} -conserving transitions into holes states near the valence band [175, 176].

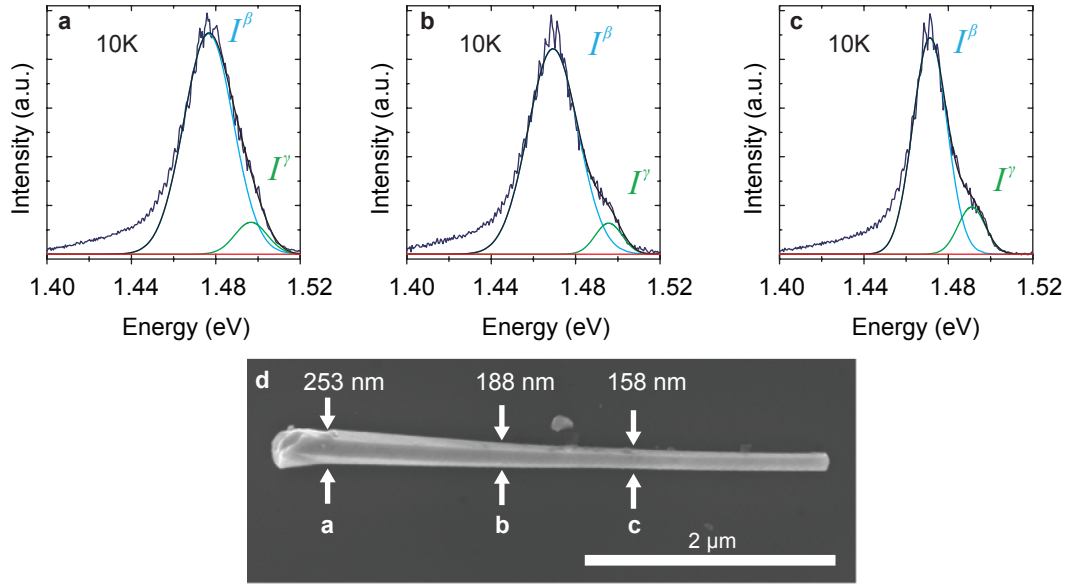


Figure 5.6: Reference beryllium doped GaAs–AlGaAs core-shell nanowire measured by the NSOM-TEM strategy, which reveals the ZB crystal structure along its entire length. (a-c) Representative normalised local near-field PL spectra selected at positions along the wire marked by arrows in the top-view scanning electron microscopy image shown in (d). Numbers indicate a diameter of the wire, which has a slightly tapered shape. The scale bar is 2 μm .

In order to verify the incorporation of Be into GaAs nanowires, an attempt to map a local beryllium doping level by means of energy-dispersive X-ray (EDX) spectroscopy and electron energy loss spectroscopy (EELS) was made. The corresponding experimental data can be found in [173] (supporting information). However, the doping level in these GaAs NWs is found to be below the sensitivity limit of these techniques. Although, large clusters with a high beryllium concentration would be resolved in these measurements. Since such precipitates were not found, it can be concluded that Be is substitutionally incorporated in selected NWs. Thus, a more detailed information about the local beryllium doping can be extracted from the near-field PL spectra. To verify that the observed PL spectra in the ZB segment of the wire are the characteristic signature of a high level of beryllium dopants in the zinc blende GaAs, an additional nanowire investigated by the NSOM-TEM approach is selected for comparison. In Figure 5.6a-c, the representative PL spectra taken from different positions along this wire are presented. All spectra reproduce the observed PL spectra in the ZB segment of the nanowire shown in Figure 5.3b(top). Structural analysis by TEM reveals its pure ZB crystal structure. Therefore, these results confirm that the corresponding I^β band resolved in the ZB segment of the first nanowire is the characteristic signature of heavily beryllium doped ZB GaAs.

5.5.2 Evaluation of the hole concentration

Now, the transformations of PL spectra in GaAs nanowires induced by beryllium doping can be quantitatively analysed. With the increase of the doping level, mainly two effects are expected for highly doped semiconductors: a band gap shrinkage and a line width broadening [175, 176]. First, a pronounced band gap shrinkage scaling with the third root of the

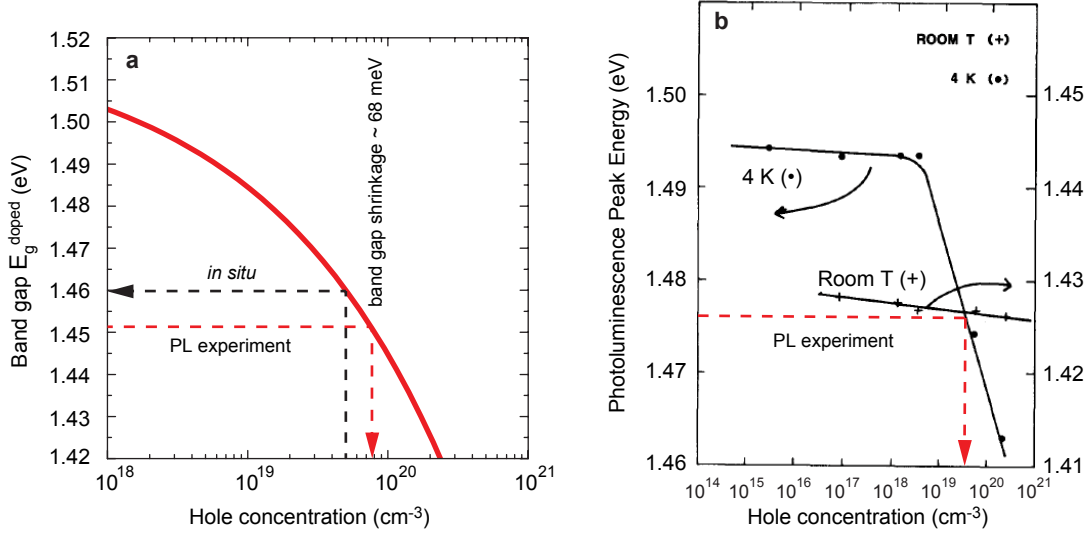


Figure 5.7: (a) The band gap shrinkage of bulk ZB GaAs as a function of the hole concentration p (red solid line, Eq. 5.5.1). The black dashed line indicates the band gap expected for the *in situ* doping level, which was set by the growth parameters. The red dashed line provides an estimation of the hole concentration deduced by extracting the band gap value from near-field PL spectra in Figure 5.3(b, top panel). (b) PL peak energy of p -type GaAs layers measured at a room temperature (crosses) and 4 K (full circles) as a function of the hole concentration (redrawn from Zhang *et al.* [178]).

hole concentration was previously reported for heavily p -type doped bulk GaAs [175]. In the work of H. C. Casey and F. Stern [177], the band gap shrinkage as a function of the hole concentration was described as

$$\Delta E_g = E_g^{\text{pure}} - E_g^{\text{doped}} = 1.6 \times 10^{-8} \cdot p^{1/3}, \quad (5.5.1)$$

where $E_g^{\text{pure}} = 1.519$ eV is taken as the band gap of undoped bulk GaAs at 10 K. This dependence is plotted in Figure 5.7a. Following [175], the band gap shrinkage of 68 meV in the ZB segment of the Be-doped GaAs nanowire was estimated from the PL spectrum in Figure 5.3b(top). This points out to a local hole concentration of 8×10^{19} cm⁻³ (Fig. 5.7a, red dashed line). In addition, the observed red-shift of the PL peak energy of NWs is compared with the results of the optical characterisation of beryllium-doped bulk GaAs samples provided by Zhang *et al.* [178]. The PL peak energy of p -type GaAs layers measured at the room and cryogenic temperatures as a function of the hole concentration is shown in Figure 5.7b. The estimation (red dashed line) based on a comparison of these data and the PL peak energy of 1.476 eV derived from the ZB segment of the beryllium doped GaAs nanowire gives a hole concentration of about 6×10^{19} cm⁻³. Importantly, the estimated carrier concentration, which is expected to induce such red-shift of PL spectra of ZB GaAs, agrees well with the chosen *in situ* doping level, which was set during the growth process to 5×10^{19} cm⁻³.

Second, an increase of the doping level will inevitably enhance the line width of the resonance [175, 179, 180]. Zhang *et al.* [180] found that the photoluminescence full width at half maximum (FWHM) δE of heavily Be-doped GaAs depends logarithmically on the hole

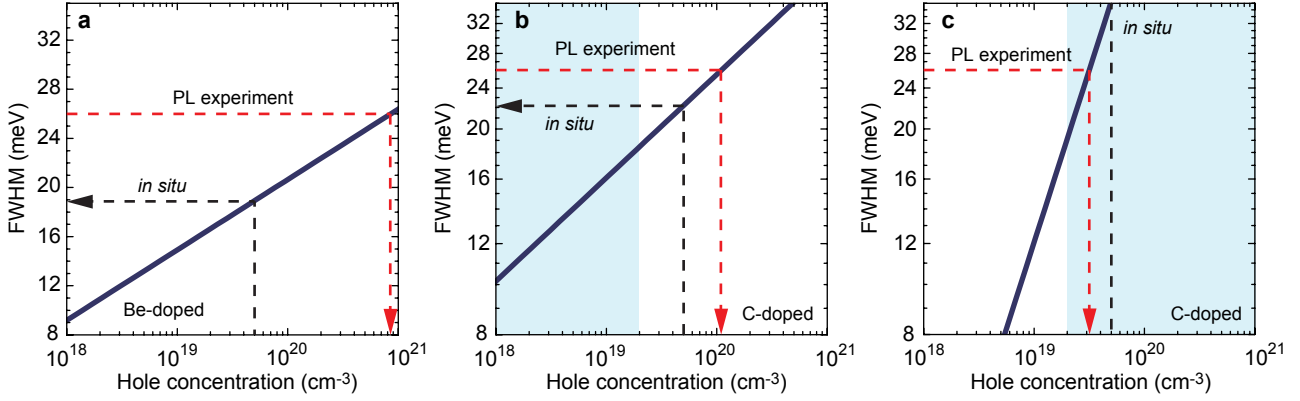


Figure 5.8: Full width at half maximum (FWHM) of the PL band as a function of hole concentration induced by impurity doping: (a) for beryllium doped planar GaAs according to Eq. 5.5.2, (b) for carbon doped planar GaAs according to Eq. 5.5.3 for the doping level $10^6 \text{ cm}^{-3} < p < 10^{19} \text{ cm}^{-3}$, (c) for carbon doped planar GaAs according to Eq. 5.5.4 for the doping level $p > 10^{19} \text{ cm}^{-3}$. The shadowed region indicates the applicability range for empirically defined relations.

concentration p :

$$\frac{\delta E}{d} = \ln \frac{p}{c} \quad (5.5.2)$$

where parameters $c = 2.5 \cdot 10^{16} \text{ cm}^{-3}$ and $d = 2.49$ are given at the temperature of 4 K and the full width at half maximum δE is measured in meV. This dependence is plotted in Figure 5.8a. Moreover, for heavily carbon doped GaAs, which also results in the p -type conductivity, Kim *et al.* [179] provided the following empirical relations between δE and the carrier concentration p :

$$\delta E = (2.55 \times 10^{-6}) \cdot p^{1/5} \text{ eV}; \quad 10^{16} < p < 10^{19} \text{ cm}^{-3}, \quad (5.5.3)$$

and

$$\delta E = (2.60 \times 10^{-15}) \cdot p^{2/3} \text{ eV}; \quad p > 10^{19} \text{ cm}^{-3}. \quad (5.5.4)$$

These dependences are plotted in Figure 5.8b,c. As it can be seen, the FWHM shows a strong dependence on the hole concentration. The FWHM of the I^β band derived from PL spectra in Figure 5.3b(top) is about 26 meV. According to Eq. 5.5.2, this would indicate an unreasonably high hole concentration of about 10^{21} cm^{-3} (Fig. 5.8a). It may be concluded that this relation is apparently not applicable to present p -doped GaAs nanowires without taking into account an additional mechanism that induces the PL band broadening. Equation 5.5.3 (Fig. 5.8b) is out of its validity range in the region of $p > 10^{19} \text{ cm}^{-3}$, where both the *in situ* hole concentration and the concentration derived from PL spectra are found. However, the Eq. 5.5.4 provides an estimation of the hole concentration of about $3 \times 10^{19} \text{ cm}^{-3}$ at a PL band width of 26 meV. This result agrees reasonably well with the conclusion drawn from the band gap shrinkage. Even though the analysis of FWHM as a function of the hole concentration provides less certain estimation of p values, the strong variation of FWHM itself along the wire length can be used as an indicator of drastic changes in the hole concentration.

In Table 5.1, the values of the hole concentration estimated from our experiments are summarised. The band gap shrinkage and the PL peak position derived from NSOM measurements are found to be in a good agreement with previously published results on heavily beryllium doped bulk GaAs. Therefore, an average doping level is estimated to be from $6 \times 10^{19} \text{ cm}^{-3}$ to $8 \times 10^{19} \text{ cm}^{-3}$ using the corresponding relations. In addition, this is generally in line with selected *in situ* doping level of $5 \times 10^{19} \text{ cm}^{-3}$, which is defined by growth parameters.

Table 5.1: Evaluation of the hole concentration of heavily beryllium doped GaAs nanowires

	NSOM experiment	Hole concentration, (cm^{-3})
Band gap, E_g (eV)	1.451	8×10^{19}
Peak energy, E_m (eV)	1.476	6×10^{19}
FWHM, δE (meV)	26	1×10^{20} (Eq. 5.5.3)
FWHM, δE (meV)	26	3×10^{19} (Eq. 5.5.4)

In summary, the PL spectra from the ZB segment of the selected NW and the reference ZB NW allow us, indeed, to proof a successful incorporation of beryllium into the structure. The attempt to quantify the hole concentration gives values that are in a good agreement with an *in situ* doping level of $5 \times 10^{19} \text{ cm}^{-3}$. Such quantification is possible by the comparison of spatially resolved local PL spectra with a ZB bulk GaAs reference pair. It is important that the main effects of the high hole concentration expected here for beryllium-doped GaAs NWs are the average shrinkage of the ZB GaAs band gap to the value of about 1.460 eV, the corresponding red-shift of the PL peak and the broadening of the emission line. In addition, the spatially homogeneous peak energy and the bandwidth in the top region of the wire (Fig. 5.3, Fig. 5.5a) are taken thus as an indication for a spatially homogeneous doping profile in this wire. This is supported by recent studies of doping incorporation paths, which conclude that the beryllium atoms, dopants with a high diffusion coefficient, are mostly incorporated from the side facets of GaAs nanowires [161]. This result suggests that the doping profile along the wire length is rather homogeneous. Moreover, it was shown that substantial changes in the growth temperature are needed to induced pronounced gradients in the doping concentration [165]. Therefore, spatial deviations of spectral characteristics from those observed in ZB regions of Be-doped GaAs NWs are considered in the next paragraphs as a function of changes of the local crystal structure.

In the map of local PL spectra (Fig. 5.3b, centre and bottom), in addition to the I^β band, a clear emergence of new optical transitions is observed. It is difficult to attribute the emergence of this additional peak, tentatively assigned as I^α , to a doping effect. Instead, this band is expected to arise from variations of the local crystal phase structure, which is discussed in the next section.

5.6 Twinning superlattice in Be-doped GaAs nanowires

The spectra recorded in the center region of the wire, at positions between 1.0 and 3.1 μm (Fig. 5.5a), are of particular interest. As it can be seen in Figure 5.3b (center), these spectra are more complex than the spectra observed in the top region. Moving from the topmost ZB-type region of the NW to the center structure, an abrupt blue-shift of the I^β peak by about

$\Delta E_{TSL} \approx 10$ meV in the region from 3.3 to 3.1 μm , in parallel with the emergence of the new low-energy I^α band, is observed (Fig. 5.5a). Structural analysis reveals the appearance of rotationally twinned ZB segments of the constant periodicity, which form the TSL structure extending over a length of more than 2 μm . Since a nearly homogeneous doping level along the NW growth direction is considered, the PL spectral behaviour in the TSL region can be described as a function of the crystal structure only. The abrupt shift of the I^β peak energy at the interface between a pure ZB-type segment (top) and a TSL structure (center) supports this approach (Fig. 5.5a).

It is found that the low-energy emission peak, I^α , is red-shifted by about 26 meV with respect to the I^β emission. This low energy emission is seen in all regions with a sufficiently high density of twin defects and hence is attributed to the presence of these defects. In particular, the I^α band is absent in the ZB reference NW with the similar doping level (Fig. 5.6). The line width of both the I^α and the I^β emission does not change much with the position along the top and center regions (Fig. 5.9). Since a significant change in line width is not observed, the local beryllium doping concentration, which is the main cause of the line broadening, is assumed to be spatially rather homogeneous along the NW. All the arguments point to an assignment of the low-energy I^α band to a spatially indirect emission between electron states in the conduction band of rotationally twinned ZB segments and a confined hole state in the WZ layer at the twin interface.

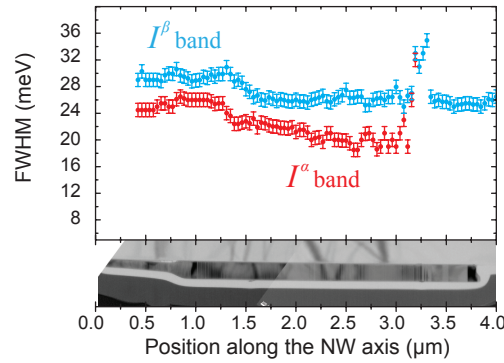


Figure 5.9: Spatial variation of the FWHM of the I^α (red circles) and I^β (blue circles) emission bands along the nanowire axis. Vertical error bars are given.

Interestingly, the emergence of the low-energy emission band I^α in the TSL region is not accompanied by the simultaneous vanishing of the high-energy I^β band due to the relaxation of carriers to the lowest energy states and the subsequent recombination. Such PL spectra behaviour was previously observed for undoped GaAs nanowires with WZ inclusions. Moreover, the I^β band is blue-shifted by about 10 meV in comparison with the top region of the wire as shown in Figure 5.5a. The observation of both I^α and I^β bands in the TSL region can be attributed to the high p -type doping level induced by the beryllium incorporation. The resulting high hole concentration can lead to the filling of the low-energy states in the valence band, which are formed due to the WZ inclusions. The excess of holes will therefore trigger band-to-band transitions (Fig. 5.10a) in rotationally twinned ZB segments even at the moderate excitation power.

The blue-shift of the I^β band is attributed to the electron states quantisation in the conduction band. Theoretical calculations suggest that the TSL structure induces electron

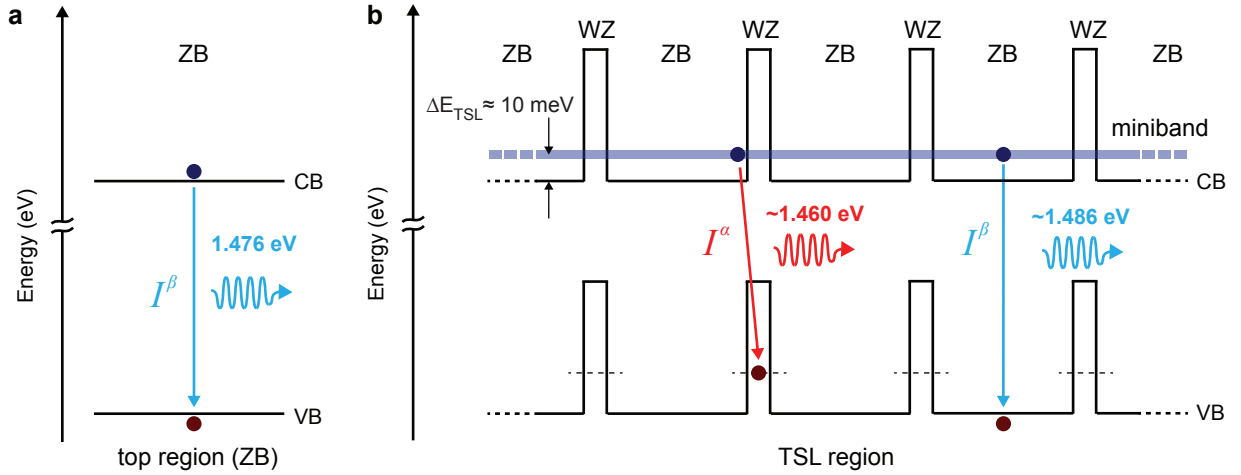


Figure 5.10: (a) Schematic of the band-to-band transition that gives rise to the I^β emission in the top region of a heavily Be-doped ZB GaAs nanowire. (b) Schematic of the origin of the I^α (red) and I^β (blue) emissions in the center TSL region of the nanowire due to the miniband formation and the hole localisation at the interface of rotationally twinned ZB segments.

quantum confinement in the ZB phase and the miniband formation, with miniband energies varying with the twin density [181]. The thin barriers in the conduction band formed by the WZ monolayers allow the efficient electron tunnelling between the adjacent ZB segments and, hence, the electron delocalisation and the superlattice formation [181]. In this TSL center region, the dominant I^β peak is then assigned to a transition between the lowest TSL conduction miniband and a valence band hole state in the ZB region as schematically shown in Figure 5.10b (blue photon). As it was mentioned above, this high-energy transition is triggered by the excess of holes in the valence band of the wire induced by the high p -type doping and the filling of all lower energy states. The I^α emission, on the other hand, reflects transitions between TSL states and heavy-hole-like bound states in WZ monolayers (Fig. 5.10b, red photon). The energy splitting between both bands is position-independent for this region. The variation in the peak energy of both the I^α and I^β peaks with the twin density tracks the spatial variation in the quantum confinement of the delocalised electron states. Here, both the structural TEM characterisation and the near-field optical data give evidence for the formation of the spatially highly homogeneous twinning superlattice region with delocalised electron states, with the wave function extending through the superlattice.

According to the proposed recombination model in the TSL region (Fig. 5.10b), the red-shift of the I^α with respect to the I^β emission of about 26 meV provides a measure of the hole confinement energy at inclusions of WZ unit cells in a ZB matrix. The magnitude of this red-shift is virtually constant along the TSL region (Fig. 5.5a). The observed shift is considerably larger than the binding energy of an exciton at a single twin defect (~ 5 meV) [48] and the red-shift of PL emission at the single twin plane discussed in the previous chapter. Thus, the short length periodicity of WZ inclusions in the TSL regions suggests to consider of WZ quantum wells as coupled that might lead to the stronger red-shift of the corresponding PL emission. Reasonable estimates of the shifts can be obtained from recently introduced superlattice models for the lowest PL transition energy [22].

In the bottom region of the NW, at positions between 0.5 and 1.0 μm , both I^α and I^β

PL bands are found to be red-shifted. The relative amplitude of the I^α is larger than the relative amplitude in the TSL region (Fig. 5.5b, red circles). The larger fraction of the I^α band in PL spectra correlates well with the increased density of crystal structure defects. This additionally confirms that it originates from the indirect transitions between electron and holes localised in ZB- and WZ-type segments, respectively. Moreover, the stronger crystal structure inhomogeneity is expected to induce the broadening of PL bands as shown in Figure 5.9, which was also observed for undoped GaAs nanowires with a mixture of ZB and WZ phases. Interestingly, the peak energy of the I^β emission is similar to that in the top region of the NW, even though the density of twin interfaces increases substantially from 1.0 to 0.5 μm (Fig. 5.5b, green circles). The red-shift of I^β band may also point to changes in the quantum confinement of electronic states possibly due to the inclusion of the 50-nm-long ZB segment (Fig. 5.4b), however, it is difficult to clearly assign the quantum confinement effects on the local optical spectra in the bottom part of the NW. In this region, it is challenging to clearly correlate structural and optical properties of the NW for a variety of reasons: (i) larger segments of WZ phase are formed, apparently red-shifting the optical spectra, (ii) the thickness of the AlGaAs shell surrounding the NW varies, affecting the optical resonance energies and emission intensities, and (iii) the crystal structure varies on a scale that is small compared to the optical resolution and the carrier diffusion length, and hence, such correlations in the bottom region may not be fully resolved in the present experiments.

However, the structurally and optically resolved twin plane superlattices in the center region and the resulting conduction miniband (Fig. 5.10) now could also explain the strong emission intensities observed at the edges of the integrated PL map of the wire in Figure 5.2a. In these outer top and bottom regions, the electron quantisation is reduced, minibands do not exist due to the lacking periodicity of ZB and WZ regions, and the electron states are more similar to those of a planar ZB region. Hence, electrons created in the high-energy conduction band states of the TSL region will drift-diffuse into the lower energy conduction band states in the outer region, acting as efficient electron traps. As it is shown in the optical spectra in Figure 5.2a, the emission intensity in the center TSL region is therefore reduced and the greatly enhanced emission intensity is observed at the very ends of the nanowire.

5.7 Summary

In summary, the low-temperature near-field scanning optical microscopy and high-resolution electron microscopy measurements have been combined to explore the correlation between the crystal structure and local optical properties of beryllium doped GaAs–AlGaAs core-shell nanowires. By resolving the local PL spectra from ZB segments of these p -type GaAs nanowires, the shrinkage of the band gap in comparison with undoped ZB GaAs is defined. This allows the estimation of the hole concentration, which results from the beryllium incorporation. The obtained value of about $8 \times 10^{19} \text{ cm}^{-3}$ is in a good agreement with the doping level selected by growth parameters. The expected homogeneous doping profile along the wire and characteristic PL spectra of p -type ZB GaAs defined by the NSOM-TEM approach allows to reveal spectral changes induced by crystal structure variations.

Indeed, the deviation of spectral characteristics of local PL spectra from those of ZB-type heavily doped GaAs nanowires correlates well with the spatial inhomogeneity of the crystal structure, as derived by NSOM-TEM analysis. Thereby, the modification of the optical band gap induced by the formation of twinning superlattices in heavily beryllium-doped GaAs nanowires is proposed. Together, TEM and NSOM experiments provide evidence

for a hole localisation in a monolayer of wurtzite type GaAs at the interface between two rotationally twinned ZB segments. More importantly, the presented data strongly suggest the electron quantum confinement in the conduction band of a periodic twinning superlattice array. Throughout a mesoscopic range of more than $1.5 \mu\text{m}$, this TSL array shows a virtually perfect periodic arrangement of the twin interfaces. The observed blue-shift of the local PL spectra is qualitatively explained in terms of the quantum confinement model suggesting the miniband formation and the electron delocalisation in the TSL conduction band.

Outlook

At present, the resulting optical spectra of the TSL structure are largely inhomogeneously broadened due to the presence of a comparatively high level of beryllium dopants. This encourages to study of TSL nanowires with reduced dopant levels in order to unveil the positive effects of the intrinsically high structural quality and the periodic arrangement of twin interfaces on their optical properties. The correlation of the PL intensity distribution with the crystal structure also suggests that it may be of a substantial interest to explore the drift-diffusive carrier transport in this class of nanowires. Such experiments are considered for future research.

Chapter 6

Conclusion

In the thesis work, local structure-property relationships and physical phenomena arising from the spatial inhomogeneity of structural and composition properties of such semiconductor nanostructures as InAs quantum dots and GaAs nanowires were addressed by means of near-field scanning optical microscopy. In order to achieve the spatial resolution of their optoelectronic properties at the nanometer length scale, a dedicated home-build near-field scanning optical microscope (NSOM) operating at cryogenic temperatures was installed and successfully applied. The experimental protocol of correlated near-field spectral imaging and structural analysis by transmission electron microscopy was developed, to provide a better insight into the structure-property relationships in crystal-phase heterostructures of GaAs nanowires. Importantly, this protocol allows to perform both measurements on one and the same nanowires. To the best of authors knowledge, such NSOM-TEM correlation on GaAs nanowires has not been demonstrated so far.

An accurate high spatially resolved map of the local charge carrier recombination, which occurs in a mixture of zinc blende and wurtzite crystal-phase nanodomains of different orders and lateral extents in individual GaAs nanowires, was demonstrated by near-field spectral imaging. The spectrally and spatially resolved information provided by NSOM allowed to identify individual photoluminescence bands and trace the spatial alternation of their spectral characteristics. As a result, electronic transitions related to well-separated emission bands were assigned to such crystal-phase heterostructures as a single zinc blende disk in a wurtzite matrix as well as a wurtzite disk in a zinc blende matrix. These crystal-phase nanodomains were characterised with the lattice-resolved accuracy using advantages of the NSOM-TEM strategy. Thus, the experimental results of this work provide exceptional quantitative parameters for the theoretical modelling of the electrons and holes confinement in crystal-phase heterostructures. This would allow thereby to derive such material parameters as the band gap and the effective electron mass of wurtzite GaAs, which has both high fundamental and practical importances. As an extension of this research, theoretical calculations using the experimental data obtained by the NSOM-TEM approach are currently being performed within a collaborative work with Dr. Pierre Corfdir from *Paul Drude Institute for Solid State Electronics*.

The incorporation of beryllium dopants during the growth process leads to the formation of *p*-type GaAs nanowires and have an effect on their optoelectronic properties as well as the crystal structure. By studying local near-field photoluminescence spectra of heavily beryllium-doped GaAs nanowires, the band gap reduction in zinc-blende segments due to the high hole concentration was found, providing evidence of an efficient incorporation of

beryllium dopants. The quantitative estimation of their concentration was performed, which was in line with growth parameters. Importantly, the formation of a twinning superlattice in such beryllium-doped GaAs nanowires was found. This finding confirms the effect of the incorporation of impurities on growth mechanisms, resulting in a periodic arrangement of twin planes. By resolving characteristic emission peaks of homogeneous zinc blende segments of heavily doped GaAs nanowires, the modification of photoluminescence spectra induced by twinning superlattice formation was revealed. This allows to suggest models of electronic transitions in such heterostructures in correspondence to the theoretically predicted miniband structure of twinning superlattices.

Thus, the results of this work provide direct and quantitative insights into the structure-property relationships in various GaAs nanowires that allow the verification of previously reported experimental and theoretical findings on their optoelectronic properties. This knowledge can be considered as a basis for future research and represents an important step forward towards the understanding of the band gap engineering in nanowires by a controlled crystal-phase formation.

In addition to the work described in this thesis, the local optical properties of III-nitride semiconductor nanostructures were thoroughly studied in the collaborative projects with Dr. Richard Nötzel and *Institute of Optoelectronic Systems and Microtechnology of Technical University of Madrid*. The project involved the investigation of near-infrared emitting In-rich $\text{In}_x\text{Ga}_{1-x}\text{N}$ layers grown directly on silicon and InN surface quantum dots by the presented in this thesis low-temperature near-field scanning optical microscope. The results of a comprehensive study of these novel and high quality materials were published in the peer-reviewed journals [iii, iv].

In summary, the experimental results of this work confirm high capabilities of the low-temperature near-field scanning optical microscope to probe local optoelectronic properties of semiconductor materials at the nanometer length scale. Importantly, this powerful experimental technique as well as its combination with transmission electron microscopy measurements can be applied to study a broad range of physical phenomena in the field of semiconductor nanostructures, which are not limited by the objectives of the present work. Being a home-build setup, NSOM allows the modification of its components, such as near-field probes, in order to meet requirements of future research projects. Such versatile tool opens up possibilities to address, for instance, nanoscale physical phenomena in magnetic nanostructures, which correspond to the current research interest of our group.

Bibliography

- [1] M. D. Kelzenberg, S. W. Boettcher, J. A. Petykiewicz, D. B. Turner–Evans, M. C. Putnam, E. L. Warren, J. M. Spurgeon, R. M. Briggs, N. S. Lewis and H. A. Atwater. *Enhanced absorption and carrier collection in Si wire arrays for photovoltaic applications*. Nat. Mater., **9**, 239 (2010).
- [2] C. Santori, D. Fattal, J. Vučković, G. S. Solomon and Y. Yamamoto. *Indistinguishable photons from a single-photon device*. Nature, **419**, 594 (2002).
- [3] S. Assefa, F. Xia and Y. A. Vlasov. *Reinventing germanium avalanche photodetector for nanophotonic on-chip optical interconnects*. Nature, **464**, 80 (2010).
- [4] S. Hu, C.-Y. Chi, K. T. Fountaine, M. Yao, H. A. Atwater, P. D. Dapkus, N. S. Lewis and C. Zhou. *Optical, electrical, and solar energy-conversion properties of gallium arsenide nanowire-array photoanodes*. Energy Environ. Sci., **6**, 1879 (2013).
- [5] M. T. Björk, B. J. Ohlsson, T. Sass, A. I. Persson, C. Thelander, M. H. Magnusson, K. Deppert, L. R. Wallenberg and L. Samuelson. *One-dimensional heterostructures in semiconductor nanowhiskers*. Appl. Phys. Lett., **80**, 1058 (2002).
- [6] T. Mårtensson, C. P. T. Svensson, B. A. Wacaser, M. W. Larsson, W. Seifert, K. Deppert, A. Gustafsson, L. R. Wallenberg and L. Samuelson. *Epitaxial III–V Nanowires on Silicon*. Nano Lett., **4**, 1987 (2004).
- [7] E. Uccelli, J. Arbiol, C. Magen, P. Krogstrup, E. Russo-Averchi, M. Heiss, G. Mugny, F. Morier-Genoud, J. Nygard, J. R. Morante and A. Fontcuberta i Morral. *Three-Dimensional Multiple-Order Twinning of Self-Catalyzed GaAs Nanowires on Si Substrates*. Nano Lett., **11**, 3827 (2011).
- [8] A. Standing, S. Assali, L. Gao, M. A. Verheijen, D. van Dam, Y. Cui, P. H. L. Notten, J. E. M. Haverkort and E. P. A. M. Bakkers. *Efficient water reduction with gallium phosphide nanowires*. Nat. Commun., **6**, 7824 (2015).
- [9] L. V. Titova, T. B. Hoang, H. E. Jackson, L. M. Smith, J. M. Yarrison–Rice, Y. Kim, H. J. Joyce, H. H. Tan and C. Jagadish. *Temperature dependence of photoluminescence from single core-shell GaAs–AlGaAs nanowires*. Appl. Phys. Lett., **89**, 173126 (2006).
- [10] W. Lu and C. M. Lieber. *Semiconductor nanowires*. J. Phys. D. Appl. Phys., **39**, R387 (2006).
- [11] H. J. Joyce, Q. Gao, H. Hoe Tan, C. Jagadish, Y. Kim, J. Zou, L. M. Smith, H. E. Jackson, J. M. Yarrison–Rice, P. Parkinson and M. B. Johnston. *III–V semiconductor*

- nanowires for optoelectronic device applications.* Prog. Quantum Electron., **35**, 23 (2011).
- [12] K. Tomioka, T. Tanaka, S. Hara, K. Hiruma and T. Fukui. *III–V Nanowires on Si Substrate: Selective-Area Growth and Device Applications.* IEEE J. Sel. Top. Quantum Electron., **17**, 1112 (2011).
- [13] N. P. Dasgupta, J. Sun, C. Liu, S. Brittman, S. C. Andrews, J. Lim, H. Gao, R. Yan and P. Yang. *25th Anniversary Article: Semiconductor Nanowires — Synthesis, Characterization, and Applications.* Adv. Mater., **26**, 2137 (2014).
- [14] G. Koblmüller and G. Abstreiter. *Growth and properties of InGaAs nanowires on silicon.* Phys. Status Solidi RRL **8**, 11–30 (2014).
- [15] K. Tomioka, J. Motohisa, S. Hara, K. Hiruma and T. Fukui. *GaAs/AlGaAs core multishell nanowire-based light-emitting diodes on Si.* Nano Lett., **10**, 1639 (2010).
- [16] K. Tomioka, M. Yoshimura and T. Fukui. *A III–V nanowire channel on silicon for high-performance vertical transistors.* Nature, **488**, 189 (2012).
- [17] Z. Wang, B. Tian, M. Paladugu, M. Pantouvaki, N. Le Thomas, C. Merckling, W. Guo, J. Dekoster, J. Van Campenhout, P. Absil and D. Van Thourhout. *Polytypic InP Nanolaser Monolithically Integrated on (001) Silicon.* Nano Lett., **13**, 5063 (2013).
- [18] A. Mazid Munshi and H. Weman. *Advances in semiconductor nanowire growth on graphene.* Phys. Status Solidi RRL, **7**, 713–726 (2013).
- [19] M. Murayama and T. Nakayama. *Chemical trend of band offsets at wurtzite/zinc-blende heterocrystalline semiconductor interfaces.* Phys. Rev. B, **49**, 4710 (1994).
- [20] T. B. Hoang, A. F. Moses, H. L. Zhou, D. L. Dheeraj, B. O. Fimland and H. Weman. *Observation of free exciton photoluminescence emission from single wurtzite GaAs nanowires.* Appl. Phys. Lett., **94**, 133105 (2009).
- [21] A. De and C. E. Pryor. *Predicted band structures of III–V semiconductors in the wurtzite phase.* Phys. Rev. B, **81**, 155210 (2010).
- [22] M. Heiss, S. Conesa–Boj, J. Ren, H.-H. Tseng, A. Gali, A. Rudolph, E. Uccelli, F. Peiró, J. R. Morante, D. Schuh, E. Reiger, E. Kaxiras, J. Arbiol and A. Fontcuberta i Morral. *Direct correlation of crystal structure and optical properties in wurtzite/zinc-blende GaAs nanowire heterostructures.* Phys. Rev. B, **83**, 045303 (2011).
- [23] B. Ketterer, M. Heiss, M. J. Livrozet, A. Rudolph, E. Reiger and A. Fontcuberta i Morral. *Determination of the band gap and the split-off band in wurtzite GaAs using Raman and photoluminescence excitation spectroscopy.* Phys. Rev. B, **83**, 125307 (2011).
- [24] D. Spirkoska, A. L. Efros, W. R. L. Lambrecht, T. Cheiwchanchamnangij, A. Fontcuberta i Morral and G. Abstreiter. *Valence band structure of polytypic zinc-blende/wurtzite GaAs nanowires probed by polarization-dependent photoluminescence.* Phys. Rev. B, **85**, 045309 (2012).

- [25] U. Jahn, J. Lähnemann, C. Pfüller, O. Brandt, S. Breuer, B. Jenichen, M. Ramsteiner, L. Geelhaar and H. Riechert. *Luminescence of GaAs nanowires consisting of wurtzite and zinc-blende segments*. Phys. Rev. B, **85**, 045323 (2012).
- [26] M. Grundmann. *The Physics of Semiconductors*. Graduate Texts in Physics. Springer Berlin Heidelberg, Berlin, Heidelberg (2010).
- [27] J. H. Davies. *The Physics of Low-Dimensional Semiconductors*. Cambridge University Press, Cambridge (1997).
- [28] S. Sze and K. K. Ng. *Physics of Semiconductor Devices*. John Wiley & Sons, Inc., Hoboken, NJ, USA (2006).
- [29] L. C. Allen. *Interpolation Scheme for Energy Bands in Solids*. Phys. Rev., **98**, 993 (1955).
- [30] J. C. Phillips. *Energy-Band Interpolation Scheme Based on a Pseudopotential*. Phys. Rev., **112**, 685 (1958).
- [31] R. A. Smith. *Semiconductors*, second edition. Cambridge University Press, London (1978).
- [32] M. L. Cohen and J. R. Chelikowsky. *Electronic Structure and Optical Properties of Semiconductors*, vol. 75 of *Springer Series in Solid-State Sciences*. Springer Berlin Heidelberg, Berlin, Heidelberg (1988).
- [33] Y. Varshni. *Temperature dependence of the energy gap in semiconductors*. Physica, **34**, 149 (1967).
- [34] M. L. Cohen and J. R. Chelikowsky. *Electronic Structure and Optical Properties of Semiconductors*, vol. 75 of *Springer Series in Solid-State Sciences*. Springer Berlin Heidelberg, Berlin, Heidelberg (1989).
- [35] P. Y. Yu and M. Cardona. *Fundamentals of Semiconductors*. Graduate Texts in Physics. Springer Berlin Heidelberg, Berlin, Heidelberg (2010).
- [36] Y. Xia, P. Yang, Y. Sun, Y. Wu, B. Mayers, B. Gates, Y. Yin, F. Kim and H. Yan. *One-Dimensional Nanostructures: Synthesis, Characterization, and Applications*. Adv. Mater., **15**, 353 (2003).
- [37] R. G. Hobbs, N. Petkov and J. D. Holmes. *Semiconductor Nanowire Fabrication by Bottom-Up and Top-Down Paradigms*. Chem. Mater., **24**, 1975 (2012).
- [38] R. S. Wagner and W. C. Ellis. *Vapor-Liquid-Solid Mechanism of Single Crystal Growth*. Appl. Phys. Lett., **4**, 89 (1964).
- [39] K. Hiruma, M. Yazawa, K. Haraguchi, K. Ogawa, T. Katsuyama, M. Koguchi and H. Kakibayashi. *GaAs free-standing quantum-size wires*. J. Appl. Phys., **74**, 3162 (1993).
- [40] V. G. Dubrovskii. *Nucleation Theory and Growth of Nanostructures*. NanoScience and Technology. Springer Berlin Heidelberg, Berlin, Heidelberg (2014).

- [41] C. Colombo, D. Spirkoska, M. Frimmer, G. Abstreiter and A. Fontcuberta i Morral. *Ga-assisted catalyst-free growth mechanism of GaAs nanowires by molecular beam epitaxy*. Phys. Rev. B, **77**, 155326 (2008).
- [42] J. Harmand, M. Tchernycheva, G. Patriarche, L. Travers, F. Glas and G. Cirlin. *GaAs nanowires formed by Au-assisted molecular beam epitaxy: Effect of growth temperature*. J. Cryst. Growth, **301-302**, 853 (2007).
- [43] W. Seifert, M. Borgström, K. Deppert, K. A. Dick, J. Johansson, M. W. Larsson, T. Mårtensson, N. Sköld, C. Patrik T. Svensson, B. A. Wacaser, L. Reine Wallenberg and L. Samuelson. *Growth of one-dimensional nanostructures in MOVPE*. J. Cryst. Growth, **272**, 211 (2004).
- [44] F. Glas, M. R. Ramdani, G. Patriarche and J.-C. Harmand. *Predictive modeling of self-catalyzed III-V nanowire growth*. Phys. Rev. B, **88**, 195304 (2013).
- [45] F. Glas, J.-C. Harmand and G. Patriarche. *Why Does Wurtzite Form in Nanowires of III-V Zinc Blende Semiconductors?* Phys. Rev. Lett., **99**, 146101 (2007).
- [46] H. J. Joyce, Q. Gao, H. H. Tan, C. Jagadish, Y. Kim, M. A. Fickenscher, S. Perera, T. B. Hoang, L. M. Smith, H. E. Jackson, J. M. Yarrison-Rice, X. Zhang and J. Zou. *High Purity GaAs Nanowires Free of Planar Defects: Growth and Characterization*. Adv. Funct. Mater., **18**, 3794 (2008).
- [47] P. Caroff, K. A. Dick, J. Johansson, M. E. Messing, K. Deppert and L. Samuelson. *Controlled polytypic and twin-plane superlattices in III-V nanowires*. Nature Nanotechnol., **4**, 50–55 (2009).
- [48] D. Rudolph, L. Schweickert, S. Morkötter, L. Hanschke, S. Hertenberger, M. Bichler, G. Koblmüller, G. Abstreiter and J. J. Finley. *Probing the trapping and thermal activation dynamics of excitons at single twin defects in GaAs-AlGaAs core-shell nanowires*. New J. Phys., **15**, 113032 (2013).
- [49] M. Koguchi, H. Kakibayashi, M. Yazawa, K. Hiruma and T. Katsuyama. *Crystal Structure Change of GaAs and InAs Whiskers from Zinc-Blende to Wurtzite Type*. Jpn. J. Appl. Phys., **31**, 2061 (1992).
- [50] D. L. Dheeraj, A. M. Munshi, M. Scheffler, A. T. J. van Helvoort, H. Weman and B. O. Fimland. *Controlling crystal phases in GaAs nanowires grown by Au-assisted molecular beam epitaxy*. Nanotechnology, **24**, 015601 (2013).
- [51] R. E. Algra, M. A. Verheijen, M. T. Borgström, L.-F. Feiner, G. Immink, W. J. P. van Enkevort, E. Vlieg and E. P. A. M. Bakkers. *Twinning superlattices in indium phosphide nanowires*. Nature, **456**, 369 (2008).
- [52] T. Rieger, M. I. Lepsa, T. Schäpers and D. Grützmacher. *Controlled wurtzite inclusions in self-catalyzed zinc blende III-V semiconductor nanowires*. J. Cryst. Growth, **378**, 506 (2013).
- [53] K. A. Dick, C. Thelander, L. Samuelson and P. Caroff. *Crystal phase engineering in single InAs nanowires*. Nano Lett., **10**, 3494 (2010).

- [54] A. M. Munshi, D. L. Dheeraj, J. Todorovic, A. T. van Helvoort, H. Weman and B.-O. Fimland. *Crystal phase engineering in self-catalyzed GaAs and GaAs/GaAsSb nanowires grown on Si(111)*. J. Cryst. Growth, **372**, 163 (2013).
- [55] T. Burgess, S. Breuer, P. Caroff, J. Wong-Leung, Q. Gao, H. Hoe Tan and C. Jagadish. *Twinning Superlattice Formation in GaAs Nanowires*. ACS Nano, **7**, 8105 (2013).
- [56] Z. Ikonc, G. Srivastava and J. Inkson. *Optical properties of twinning superlattices in diamond-type and zinc-blende-type semiconductors*. Phys. Rev. B, **52**, 14078 (1995).
- [57] R. Dowdy, P. Mohseni, S. A. Fortuna, J. Wen and X. Li. *Twinning Superlattice in VLS Grown Planar GaAs Nanowires Induced by Impurity Doping*. In *2012 IEEE Photonics Conf.*, pp. 693 – 694. IEEE, New York (2012).
- [58] H. Shtrikman, R. Popovitz-Biro, A. Kretinin and M. Heiblum. *Stacking-faults-free zinc blende GaAs nanowires*. Nano Lett., **9**, 215 (2009).
- [59] B. Ketterer, M. Heiss, E. Uccelli, J. Arbiol and A. F. i Morral. *Untangling the electronic band structure of wurtzite GaAs nanowires by resonant Raman spectroscopy*. ACS Nano, **5**, 7585 (2011).
- [60] L. Ahtapodov, J. Todorovic, P. Olk, T. Mjåland, P. Slåttnes, D. L. Dheeraj, A. T. J. van Helvoort, B.-O. Fimland and H. Weman. *A story told by a single nanowire: optical properties of wurtzite GaAs*. Nano Lett., **12**, 6090 (2012).
- [61] P. Corfdir, B. Van Hattem, E. Uccelli, S. Conesa-Boj, P. Lefebvre, A. Fontcuberta i Morral and R. T. Phillips. *Three-Dimensional Magneto-Photoluminescence as a Probe of the Electronic Properties of Crystal-Phase Quantum Disks in GaAs Nanowires*. Nano Lett., **13**, 5303 (2013).
- [62] L. C. Chuang, M. Moewe, K. W. Ng, T.-T. D. Tran, S. Crankshaw, R. Chen, W. S. Ko and C. Chang-Hasnain. *GaAs nanoneedles grown on sapphire*. Appl. Phys. Lett., **98**, 123101 (2011).
- [63] N. Akopian, G. Patriarche, L. Liu, J.-C. Harmand and V. Zwiller. *Crystal phase quantum dots*. Nano Lett., **10**, 1198 (2010).
- [64] D. Spirkoska, J. Arbiol, A. Gustafsson, S. Conesa-Boj, F. Glas, I. Zardo, M. Heigoldt, M. H. Gass, A. L. Bleloch, S. Estrade, M. Kaniber, J. Rossler, F. Peiro, J. R. Morante, G. Abstreiter, L. Samuelson and A. Fontcuberta i Morral. *Structural and optical properties of high quality zinc-blende/wurtzite GaAs nanowire heterostructures*. Phys. Rev. B, **80**, 245325 (2009).
- [65] E. D. Minot, F. Kelkensberg, M. van Kouwen, J. A. van Dam, L. P. Kouwenhoven, V. Zwiller, M. T. Borgström, O. Wunnicke, M. A. Verheijen and E. P. A. M. Bakkers. *Single Quantum Dot Nanowire LEDs*. Nano Lett., **7**, 367 (2007).
- [66] T. J. Kempa, B. Tian, D. R. Kim, J. Hu, X. Zheng and C. M. Lieber. *Single and tandem axial p-i-n nanowire photovoltaic devices*. Nano Lett., **8**, 3456 (2008).
- [67] J. Wallentin and M. T. Borgström. *Doping of semiconductor nanowires*. J. Mater. Res., **26**, 2142 (2011).

- [68] C. F. Klingshirn. *Semiconductor Optics*. Graduate Texts in Physics. Springer Berlin Heidelberg, Berlin, Heidelberg (2012).
- [69] T. Elsaesser, J. Shah, L. Rota and P. Lugli. *Initial thermalization of photoexcited carriers in GaAs studied by femtosecond luminescence spectroscopy*. Phys. Rev. Lett., **66**, 1757 (1991).
- [70] E. H. Bogardus and H. B. Bebb. *Bound-Exciton, Free-Exciton, Band-Acceptor, Donor-Acceptor, and Auger Recombination in GaAs*. Phys. Rev., **176**, 993 (1968).
- [71] I. Pelant and J. Valenta. *Luminescence Spectroscopy of Semiconductors*. Oxford University Press (2012).
- [72] L. Rayleigh. *On the Theory of Optical Images, with special reference to the Microscope*. J. R. Microsc. Soc., **23**, 474 (1903).
- [73] L. Novotny and B. Hecht. *Principles of Nano-Optics*. Cambridge University Press, Cambridge (2006).
- [74] E. Synge. *XXXVIII. A suggested method for extending microscopic resolution into the ultra-microscopic region*. London, Edinburgh, Dublin Philos. Mag. J. Sci., **6**, 356 (1928).
- [75] E. A. Ash and G. Nicholls. *Super-resolution Aperture Scanning Microscope*. Nature, **237**, 510 (1972).
- [76] D. W. Pohl, W. Denk and M. Lanz. *Optical stethoscopy: Image recording with resolution $\lambda/20$* . Appl. Phys. Lett., **44**, 651 (1984).
- [77] A. Lewis, M. Isaacson, A. Harootunian and A. Muray. *Development of a 500 angstrom spatial resolution light microscope*. Ultramicroscopy, **13**, 227 (1984).
- [78] P. Kramper, M. Kafesaki, C. M. Soukoulis, A. Birner, F. Müller, U. Gösele, R. B. Wehrspohn, J. Mlynek and V. Sandoghdar. *Near-field visualization of light confinement in a photonic crystal microresonator*. Opt. Lett., **29**, 174 (2004).
- [79] K. Bittkau, R. Carius, A. Bielawny and R. B. Wehrspohn. *Influence of defects in opal photonic crystals on the optical transmission imaged by near-field scanning optical microscopy*. J. Mater. Sci. Mater. Electron., **19**, 203 (2008).
- [80] R. Pomraenke, C. Lienau, Y. Mazur, Z. Wang, B. Liang, G. Tarasov and G. Salamo. *Near-field optical spectroscopy of GaAs/Al_yGa_{1-y}As quantum dot pairs grown by high-temperature droplet epitaxy*. Phys. Rev. B, **77** (2008).
- [81] R. D. Grober, T. D. Harris, J. K. Trautman and E. Betzig. *Design and implementation of a low temperature near-field scanning optical microscope*. Rev. Sci. Instrum., **65**, 626 (1994).
- [82] M. J. Gregor, S. Grosse, P. G. Blome and R. G. Ulbrich. *Design of a Scanning Near Field Optical Microscope for Low Temperature Applications*. In O. Marti and R. Möller (Eds.), *Photons and Local Probes*, vol. 300, pp. 133–138. Springer Netherlands, Dordrecht (1995).

- [83] H. Ghaemi, C. Cates and B. Goldberg. *Low temperature near field spectroscopy and microscopy*. Ultramicroscopy, **57**, 165 (1995).
- [84] G. Behme, A. Richter, M. Suptitz and C. Lienau. *Vacuum near-field scanning optical microscope for variable cryogenic temperatures*. Rev. Sci. Instrum., **68**, 3458 (1997).
- [85] F. Intonti, V. Emiliani, C. Lienau, T. Elsaesser, R. Nötzel and K. Ploog. *Near-field optical spectroscopy of localized and delocalized excitons in a single GaAs quantum wire*. Phys. Rev. B, **63**, 075313 (2001).
- [86] G. A. Valaskovic, M. Holton and G. H. Morrison. *Parameter control, characterization, and optimization in the fabrication of optical fiber near-field probes*. Appl. Opt., **34**, 1215 (1995).
- [87] D. R. Turner. *Etch procedure for optical fibers* (1984).
- [88] K. M. Takahashi. *Meniscus shapes on small diameter fibers*. J. Colloid Interface Sci., **134**, 181 (1990).
- [89] R. Stockle, C. Fokas, V. Deckert, R. Zenobi, B. Sick, B. Hecht and U. P. Wild. *High-quality near-field optical probes by tube etching*. Appl. Phys. Lett., **75**, 160 (1999).
- [90] P. Lambelet, A. Sayah, M. Pfeffer, C. Philipona and F. Marquis-Weible. *Chemically Etched Fiber Tips for Near-Field Optical Microscopy: A Process for Smoother Tips*. Appl. Opt., **37**, 7289 (1998).
- [91] T. Pangaribuan, K. Yamada, S. Jiang, H. Ohsawa and M. Ohtsu. *Reproducible Fabrication Technique of Nanometric Tip Diameter Fiber Probe for Photon Scanning Tunneling Microscope*. Jpn. J. Appl. Phys., **31**, L1302 (1992).
- [92] S. Mononobe, M. Naya, T. Saiki and M. Ohtsu. *Reproducible fabrication of a fiber probe with a nanometric protrusion for near-field optics*. Appl. Opt., **36**, 1496 (1997).
- [93] M. Ohtsu. *Probe Fabrication*. In M. Ohtsu (Ed.), *Near-field Nano/Atom Optics Technology*, chap. 3. Springer Japan, Tokyo (1998).
- [94] B. Hecht, H. Bielefeldt, Y. Inouye, D. W. Pohl and L. Novotny. *Facts and artifacts in near-field optical microscopy*. J. Appl. Phys., **81**, 2492 (1997).
- [95] K. Karrai and R. D. Grober. *Piezoelectric tip-sample distance control for near field optical microscopes*. Appl. Phys. Lett., **66**, 1842 (1995).
- [96] C. A. J. Putman, B. G. De Grooth, N. F. Van Hulst and J. Greve. *A detailed analysis of the optical beam deflection technique for use in atomic force microscopy*. J. Appl. Phys., **72**, 6 (1992).
- [97] Y.-Y. Hu. *Site control and optical characterization of InAs quantum dots grown in GaAs nanoholes*. Dissertation, Ruhr-Universität Bochum (2013).
- [98] D. Bimberg, M. Grundmann and N. N. Ledentsov (Eds.). *Quantum Dot Heterostructures*. Wiley (1998).

- [99] N. N. Ledentsov, V. M. Ustinov, V. A. Shchukin, P. S. Kopev, Z. I. Alferov and D. Bimberg. *Quantum dot heterostructures: Fabrication, properties, lasers (Review)*. Semiconductors, **32**, 343 (1998).
- [100] P. Michler (Ed.). *Single Semiconductor Quantum Dots*. Springer (2009).
- [101] O. Gywat, H. J. Krenner and J. Berezovsky (Eds.). *Spins in Optically Active Quantum Dots: Concepts and Methods*. Wiley (2009).
- [102] R. M. Stevenson, R. J. Young, P. Atkinson, K. Cooper, D. A. Ritchie and A. J. Shields. *A semiconductor source of triggered entangled photon pairs*. Nature, **439**, 179 (2006).
- [103] C.-D. Lee, C. Park, H. J. Lee, K.-S. Lee, S.-J. Park, C. G. Park, S. K. Noh and Nobuyuki Koguchi. *Fabrication of Self-Assembled GaAs/AlGaAs Quantum Dots by Low-Temperature Droplet Epitaxy*. Jpn. J. Appl. Phys., **37**, 7158 (1998).
- [104] K. Watanabe, N. Koguchi and Y. Gotoh. *Fabrication of GaAs Quantum Dots by Modified Droplet Epitaxy*. Jpn. J. Appl. Phys., **39**, L79 (2000).
- [105] R. Nötzel. *Self-organized growth of quantum-dot structures*. Semicond. Sci. Technol., **11**, 1365 (1996).
- [106] Z. M. Wang, B. L. Liang, K. A. Sablon and G. J. Salamo. *Nanoholes fabricated by self-assembled gallium nanodrill on GaAs(100)*. Appl. Phys. Lett., **90**, 113120 (2007).
- [107] J. H. Lee, Z. M. Wang, E. S. Kim, N. Y. Kim, S. H. Park and G. J. Salamo. *Various Quantum- and Nano-Structures by III-V Droplet Epitaxy on GaAs Substrates*. Nanoscale Res. Lett., **5**, 308 (2010).
- [108] A. Rastelli, S. Stuffer, A. Schliwa, R. Songmuang, C. Manzano, G. Costantini, K. Kern, A. Zrenner, D. Bimberg and O. G. Schmidt. *Hierarchical self-assembly of GaAs/AlGaAs quantum dots*. Phys. Rev. Lett., **92**, 166104 (2004).
- [109] C. Heyn, A. Stemmann, T. Köppen, C. Strelow, T. Kipp, M. Grave, S. Mendach and W. Hansen. *Highly uniform and strain-free GaAs quantum dots fabricated by filling of self-assembled nanoholes*. Appl. Phys. Lett., **94**, 183113 (2009).
- [110] C. Heyn, A. Stemmann, T. Köppen, C. Strelow, T. Kipp, M. Grave, S. Mendach and W. Hansen. *Optical Properties of GaAs Quantum Dots Fabricated by Filling of Self-Assembled Nanoholes*. Nanoscale Res. Lett., **5**, 576 (2009).
- [111] J. Bao, D. C. Bell, F. Capasso, J. B. Wagner, T. Mårtensson, J. Trägårdh and L. Samuelson. *Optical properties of rotationally twinned InP nanowire heterostructures*. Nano Lett., **8**, 836 (2008).
- [112] J. Todorovic, A. F. Moses, T. Karlberg, P. Olk, D. L. Dheeraj, B. O. Fimland, H. Weiman and A. T. J. van Helvoort. *Correlated micro-photoluminescence and electron microscopy studies of the same individual heterostructured semiconductor nanowires*. Nanotechnology, **22**, 325707 (2011).

- [113] L. F. Zagonel, S. Mazzucco, M. Tencé, K. March, R. Bernard, B. Laslier, G. Jacopin, M. Tchernycheva, L. Rigutti, F. H. Julien, R. Songmuang and M. Kociak. *Nanometer scale spectral imaging of quantum emitters in nanowires and its correlation to their atomically resolved structure*. Nano Lett., **11**, 568 (2011).
- [114] J. Bolinsson, M. Ek, J. Trägårdh, K. Mergenthaler, D. Jacobsson, M.-E. Pistol, L. Samuelson and A. Gustafsson. *GaAs/AlGaAs heterostructure nanowires studied by cathodoluminescence*. Nano Res., **7**, 473–490 (2014).
- [115] N. Han, F. Wang, J. J. Hou, S. Yip, H. Lin, M. Fang, F. Xiu, X. Shi, T. Hung and J. C. Ho. *Manipulated Growth of GaAs Nanowires: Controllable Crystal Quality and Growth Orientations via a Supersaturation-Controlled Engineering Process*. Cryst. Growth Des., **12**, 6243 (2012).
- [116] A. D. Schricker, F. M. Davidson, R. J. Wiacek and B. A. Korgel. *Space charge limited currents and trap concentrations in GaAs nanowires*. Nanotechnology, **17**, 2681 (2006).
- [117] D. Saxena, S. Mokkaapati, P. Parkinson, N. Jiang, Q. Gao, H. H. Tan and C. Jagadish. *Optically pumped room-temperature GaAs nanowire lasers*. Nat. Photonics, **7**, 963 (2013).
- [118] J. Ayache, L. Beaunier, J. Boumendil, G. Ehret and D. Laub. *Sample Preparation Handbook for Transmission Electron Microscopy*. Springer New York, New York, NY, 1 edn. (2010).
- [119] H. Blumtritt, D. Isheim, S. Senz, D. N. Seidman and O. Moutanabbir. *Preparation of nanowire specimens for laser-assisted atom probe tomography*. Nanotechnology, **25**, 435704 (2014).
- [120] D. B. Williams and C. B. Carter. *Transmission Electron Microscopy*. Springer US, Boston, MA (2009).
- [121] H. Bethge and J. Heydenreich. *Electron microscopy in solid state physics*. Elsevier, Amsterdam (1987).
- [122] H. Kohl and L. Reimer. *Transmission Electron Microscopy*, vol. 36 of *Springer Series in Optical Sciences*. Springer New York, New York, NY (2008).
- [123] S. J. Pennycook and P. D. Nellist (Eds.). *Scanning Transmission Electron Microscopy*. Springer New York, New York, NY (2011).
- [124] S. Pennycook and D. Jesson. *High-resolution Z-contrast imaging of crystals*. Ultramicroscopy, **37**, 14 (1991).
- [125] MathWorks. *MATLAB — The Language of Technical Computing*, www.mathworks.com.
- [126] OriginLab. *Origin and OriginPro — Data Analysis and Graphing Software*, www.originlab.com.
- [127] Gatan. *DigitalMicrograph*, www.gatan.com.

- [128] W. Bao, M. Melli, N. Caselli, F. Riboli, D. S. Wiersma, M. Staffaroni, H. Choo, D. F. Ogletree, S. Aloni, J. Bokor, S. Cabrini, F. Intonti, M. B. Salmeron, E. Yablonovitch, P. J. Schuck and A. Weber-Bargioni. *Mapping local charge recombination heterogeneity by multidimensional nanospectroscopic imaging*. *Science*, **338**, 1317 (2012).
- [129] S. Schmidt, B. Piglosiewicz, D. Sadiq, J. Shirdel, J. S. Lee, P. Vasa, N. Park, D.-S. Kim and C. Lienau. *Adiabatic nanofocusing on ultrasmooth single-crystalline gold tapers creates a 10-nm-sized light source with few-cycle time resolution*. *ACS Nano*, **6**, 6040 (2012).
- [130] J. Wallentin, N. Anttu, D. Asoli, M. Huffman, I. Aberg, M. H. Magnusson, G. Siefer, P. Fuss-Kailuweit, F. Dimroth, B. Witzigmann, H. Q. Xu, L. Samuelson, K. Deppert and M. T. Borgström. *InP nanowire array solar cells achieving 13.8% efficiency by exceeding the ray optics limit*. *Science*, **339**, 1057 (2013).
- [131] V. Jain, A. Nowzari, J. Wallentin, M. T. Borgström, M. E. Messing, D. Asoli, M. Graczyk, B. Witzigmann, F. Capasso, L. Samuelson and H. Pettersson. *Study of photocurrent generation in InP nanowire-based $p^+ - i - n^+$ photodetectors*. *Nano Res.*, **7**, 544–552 (2014).
- [132] B. Mayer, D. Rudolph, J. Schnell, S. Morkötter, J. Winnerl, J. Treu, K. Müller, G. Bracher, G. Abstreiter, G. Koblmüller and J. J. Finley. *Lasing from individual GaAs–AlGaAs core-shell nanowires up to room temperature*. *Nat. Commun.*, **4**, 2931 (2013).
- [133] M. N. Makhonin, A. P. Foster, A. B. Krysa, P. W. Fry, D. G. Davies, T. Grange, T. Walther, M. S. Skolnick and L. R. Wilson. *Homogeneous array of nanowire-embedded quantum light emitters*. *Nano Lett.*, **13**, 861 (2013).
- [134] J. Svensson, A. W. Dey, D. Jacobsson and L.-E. Wernersson. *III–V Nanowire Complementary Metal-Oxide Semiconductor Transistors Monolithically Integrated on Si*. *Nano Lett.*, **15**, 7898 (2015).
- [135] K. Tomioka, Y. Kobayashi, J. Motohisa, S. Hara and T. Fukui. *Selective-area growth of vertically aligned GaAs and GaAs/AlGaAs core-shell nanowires on Si(111) substrate*. *Nanotechnology*, **20**, 145302 (2009).
- [136] C. Durand, C. Bougerol, J.-F. Carlin, G. Rossbach, F. Godel, J. Eymery, P.-H. Jouneau, A. Mukhtarova, R. Butté and N. Grandjean. *M-Plane GaN/InAlN Multiple Quantum Wells in Core-Shell Wire Structure for UV Emission*. *ACS Photonics*, **1**, 38 (2014).
- [137] E. Dimakis, U. Jahn, M. Ramsteiner, A. Tahraoui, J. Grandal, X. Kong, O. Marquardt, A. Trampert, H. Riechert and L. Geelhaar. *Coaxial multishell (In,Ga)As/GaAs nanowires for near-infrared emission on Si substrates*. *Nano Lett.*, **14**, 2604 (2014).
- [138] K. Hiruma, M. Yazawa, T. Katsuyama, K. Ogawa, K. Haraguchi, M. Koguchi and H. Kakibayashi. *Growth and optical properties of nanometer-scale GaAs and InAs whiskers*. *J. Appl. Phys.*, **77**, 447 (1995).

- [139] G. Priante, J.-C. Harmand, G. Patriarche and F. Glas. *Random stacking sequences in III–V nanowires are correlated*. Phys. Rev. B, **89**, 241301 (2014).
- [140] J. Shah, R. C. C. Leite and R. E. Nahory. *Photoluminescence and Photoconductivity in Undoped Epitaxial GaAs*. Phys. Rev., **184**, 811 (1969).
- [141] M. Ozeki, K. Nakai, K. Dazai and O. Ryuzan. *Photoluminescence Study of Carbon Doped Gallium Arsenide*. Jpn. J. Appl. Phys., **13**, 1121 (1974).
- [142] D. Ashen, P. Dean, D. Hurle, J. Mullin, A. White and P. Greene. *The incorporation and characterisation of acceptors in epitaxial GaAs*. J. Phys. Chem. Solids, **36**, 1041 (1975).
- [143] A. Gustafsson, J. Bolinsson, N. Sköld and L. Samuelson. *Determination of diffusion lengths in nanowires using cathodoluminescence*. Appl. Phys. Lett., **97**, 072114 (2010).
- [144] D. Rudolph, S. Funk, M. Döblinger, S. Morkötter, S. Hertenberger, L. Schweickert, J. Becker, S. Matich, M. Bichler, D. Spirkoska, I. Zardo, J. J. Finley, G. Abstreiter and G. Koblmüller. *Spontaneous alloy composition ordering in GaAs–AlGaAs core-shell nanowires*. Nano Lett., **13**, 1522 (2013).
- [145] M. Heiss, Y. Fontana, A. Gustafsson, G. Wüst, C. Magen, D. D. O’Regan, J. W. Luo, B. Ketterer, S. Conesa-Boj, A. V. Kuhlmann, J. Houel, E. Russo-Averchi, J. R. Morante, M. Cantoni, N. Marzari, J. Arbiol, A. Zunger, R. J. Warburton and A. Fontcuberta i Morral. *Self-assembled quantum dots in a nanowire system for quantum photonics*. Nat. Mater., **12**, 439 (2013).
- [146] Z. Zanolli, F. Fuchs, J. Furthmüller, U. von Barth and F. Bechstedt. *Model GW band structure of InAs and GaAs in the wurtzite phase*. Phys. Rev. B, **75**, 245121 (2007).
- [147] P. Kusch, S. Breuer, M. Ramsteiner, L. Geelhaar, H. Riechert and S. Reich. *Band gap of wurtzite GaAs: A resonant Raman study*. Phys. Rev. B, **86**, 075317 (2012).
- [148] P. Kusch, E. Grelich, C. Somaschini, E. Luna, M. Ramsteiner, L. Geelhaar, H. Riechert and S. Reich. *Type-II band alignment of zinc-blende and wurtzite segments in GaAs nanowires: A combined photoluminescence and resonant Raman scattering study*. Phys. Rev. B, **89**, 045310 (2014).
- [149] H. J. Lee, L. Y. Juravel, J. C. Woolley and A. J. S. Thorpe. *Electron transport and band structure of Ga_{1-x}Al_xAs alloys*. Phys. Rev. B, **21**, 659 (1980).
- [150] G. Signorello, S. Karg, M. T. Björk, B. Gotsmann and H. Riel. *Tuning the light emission from GaAs nanowires over 290 meV with uniaxial strain*. Nano Lett., **13**, 917 (2013).
- [151] G. Signorello, E. Lörtscher, P. A. Khomyakov, S. Karg, D. L. Dheeraj, B. Gotsmann, H. Weman and H. Riel. *Inducing a direct-to-pseudodirect bandgap transition in wurtzite GaAs nanowires with uniaxial stress*. Nat. Commun., **5**, 3655 (2014).
- [152] C.-Y. Yeh, Z. W. Lu, S. Froyen and A. Zunger. *Zinc-blende – wurtzite polytypism in semiconductors*. Phys. Rev. B, **46**, 10086 (1992).

- [153] I. Zardo, S. Conesa–Boj, F. Peiro, J. R. Morante, J. Arbiol, E. Uccelli, G. Abstreiter and A. Fontcuberta i Morral. *Raman spectroscopy of wurtzite and zinc-blende GaAs nanowires: Polarization dependence, selection rules, and strain effects*. Phys. Rev. B, **80**, 245324 (2009).
- [154] P. Corfdir, F. Feix, J. K. Zettler, S. Fernández-Garrido and O. Brandt. *Importance of the dielectric contrast for the polarization of excitonic transitions in single GaN nanowires*. New J. Phys., **17**, 033040 (2015).
- [155] C. M. N. Mateo, A. T. Garcia, F. R. M. Ramos, K. I. Manibog and A. A. Salvador. *Strain-induced splitting of the valence band in epitaxially lifted-off GaAs films*. J. Appl. Phys., **101**, 073519 (2007).
- [156] C. M. N. Mateo, J. J. Ibanez, J. G. Fernando, J. C. Garcia, K. Omambac, R. B. Jaculbia, M. Defensor and A. A. Salvador. *Transitions of epitaxially lifted-off bulk GaAs and GaAs/AlGaAs quantum well under thermal-induced compressive and tensile strain*. J. Appl. Phys., **104**, 103537 (2008).
- [157] S. V. Morozov, D. I. Kryzhkov, A. N. Yablonsky, A. V. Antonov, D. I. Kuritsin, D. M. Gaponova, Y. G. Sadofyev, N. Samal, V. I. Gavrilenko and Z. F. Krasilnik. *Type-II–type-I conversion of GaAs/GaAsSb heterostructure energy spectrum under optical pumping*. J. Appl. Phys., **113**, 163107 (2013).
- [158] K. Tomioka, M. Yoshimura and T. Fukui. *A III–V nanowire channel on silicon for high-performance vertical transistors*. Nature, **488**, 189 (2012).
- [159] C. Thelander, P. Agarwal, S. Brongersma, J. Eymery, L. Feiner, A. Forchel, M. Scheffler, W. Riess, B. Ohlsson, U. Gösele and L. Samuelson. *Nanowire-based one-dimensional electronics*. Mater. Today, **9**, 28 (2006).
- [160] M. Hilse, M. Ramsteiner, S. Breuer, L. Geelhaar and H. Riechert. *Incorporation of the dopants Si and Be into GaAs nanowires*. Appl. Phys. Lett., **96**, 193104 (2010).
- [161] A. Casadei, P. Krogstrup, M. Heiss, J. A. Rohr, C. Colombo, T. Ruelle, S. Upadhyay, C. B. Sorensen, J. Nygard and A. Fontcuberta i Morral. *Doping incorporation paths in catalyst-free Be-doped GaAs nanowires*. Appl. Phys. Lett., **102**, 013117 (2013).
- [162] R. J. Yee, S. J. Gibson, V. G. Dubrovskii and R. R. LaPierre. *Effects of Be doping on InP nanowire growth mechanisms*. Appl. Phys. Lett., **101**, 263106 (2012).
- [163] S.-G. Ihn, M.-Y. Ryu and J.-I. Song. *Optical properties of undoped, Be-doped, and Si-doped wurtzite-rich GaAs nanowires grown on Si substrates by molecular beam epitaxy*. Solid State Commun., **150**, 729 (2010).
- [164] A. Lysov, M. Offer, C. Gutsche, I. Regolin, S. Topaloglu, M. Geller, W. Prost and F.-J. Tegude. *Optical properties of heavily doped GaAs nanowires and electroluminescent nanowire structures*. Nanotechnology, **22**, 085702 (2011).
- [165] S. Korte, M. Steidl, W. Prost, V. Cherepanov, B. Voigtlander, W. Zhao, P. Klein-schmidt and T. Hannappel. *Resistance and dopant profiling along freestanding GaAs nanowires*. Appl. Phys. Lett., **103**, 143104 (2013).

- [166] B. A. Wacaser, K. A. Dick, J. Johansson, M. T. Borgström, K. Deppert and L. Samuelson. *Preferential Interface Nucleation: An Expansion of the VLS Growth Mechanism for Nanowires*. *Adv. Mater.*, **21**, 153 (2009).
- [167] D. Dheeraj, A. Munshi, O. Christoffersen, D. Kim, G. Signorello, H. Riel, A. van Helvoort, H. Weman and B. Fimland. *Comparison of Be-doped GaAs nanowires grown by Au- and Ga-assisted molecular beam epitaxy*. *J. Cryst. Growth*, **378**, 532 (2013).
- [168] J. Dufouleur, C. Colombo, T. Garma, B. Ketterer, E. Uccelli, M. Nicotra and A. Fontcuberta i Morral. *P-doping mechanisms in catalyst-free gallium arsenide nanowires*. *Nano Lett.*, **10**, 1734 (2010).
- [169] O. Moutanabbir, D. Isheim, H. Blumtritt, S. Senz, E. Pippel and D. N. Seidman. *Colossal injection of catalyst atoms into silicon nanowires*. *Nature*, **496**, 78 (2013).
- [170] S. Du, T. Burgess, B. Gault, Q. Gao, P. Bao, L. Li, X. Cui, W. Kong Yeoh, H. Liu, L. Yao, A. V. Ceguerra, H. Hoe Tan, C. Jagadish, S. P. Ringer and R. Zheng. *Quantitative dopant distributions in GaAs nanowires using atom probe tomography*. *Ultra-microscopy*, **132**, 186 (2013).
- [171] A. Suzuki, A. Fukuyama, H. Suzuki, K. Sakai, J.-H. Paek, M. Yamaguchi and T. Ikari. *Optical properties of Be-doped GaAs nanowires on Si substrate grown by a catalyst-free molecular beam epitaxy vapor-liquid-solid method*. *Jpn. J. Appl. Phys.*, **53**, 05FV03 (2014).
- [172] J. M. Stiegler, A. J. Huber, S. L. Diedenhofen, J. G. Rivas, R. E. Algra, E. P. A. M. Bakkers and R. Hillenbrand. *Nanoscale free-carrier profiling of individual semiconductor nanowires by infrared near-field nanoscopy*. *Nano Lett.*, **10**, 1387 (2010).
- [173] A. V. Senichev, V. G. Talalaev, I. V. Shtrom, H. Blumtritt, G. E. Cirlin, J. Schilling, C. Lienau and P. Werner. *Nanospectroscopic Imaging of Twinning Superlattices in an Individual GaAs-AlGaAs Core-Shell Nanowire*. *ACS Photonics*, **1**, 1099 (2014).
- [174] K. Ploog. *The Use of Si and Be Impurities for Novel Periodic Doping Structures in GaAs Grown by Molecular Beam Epitaxy*. *J. Electrochem. Soc.*, **128**, 400 (1981).
- [175] D. Olego and M. Cardona. *Photoluminescence in heavily doped GaAs. I. Temperature and hole-concentration dependence*. *Phys. Rev. B*, **22**, 886 (1980).
- [176] J. Nagle, R. Malik and D. Gershoni. *A comparison of atomic carbon versus beryllium acceptor doping in GaAs grown by molecular beam epitaxy*. *J. Cryst. Growth*, **111**, 264 (1991).
- [177] H. C. Casey. *Concentration-dependent absorption and spontaneous emission of heavily doped GaAs*. *J. Appl. Phys.*, **47**, 631 (1976).
- [178] D. Zhang, K. Radhakrishnan, S. Yoon and Z. Han. *Photoluminescence in degenerate p-type GaAs layers grown by molecular beam epitaxy*. *Mater. Sci. Eng. B*, **35**, 449 (1995).

-
- [179] S.-I. Kim, M.-S. Kim, Y. Kim, K. S. Eom, S.-K. Min and C. Lee. *Low temperature photoluminescence characteristics of carbon doped GaAs*. J. Appl. Phys., **73**, 4703 (1993).
- [180] D. Zhang, K. Radhakrishnan and S. Yoon. *Characterization of beryllium-doped molecular beam epitaxial grown GaAs by photoluminescence*. J. Cryst. Growth, **148**, 35 (1995).
- [181] Z. Ikonić, G. Srivastava and J. Inkson. *Electronic properties of twin boundaries and twinning superlattices in diamond-type and zinc-blende-type semiconductors*. Phys. Rev. B, **48**, 17181 (1993).

Erklärung

Ich versichere hiermit, die vorliegende Dissertation

Near-field Spectral Imaging of Crystal-phase Heterostructures in GaAs Nanowires

selbständig und ohne fremde Hilfe verfasst und keine anderen als die von mir angegebenen Quellen und Hilfsmittel verwendet zu haben. Den benutzten Werken wörtlich oder inhaltlich entnommene Stellen sind als solche gekennzeichnet.

Ich versichere hiermit, dass ich mich an keiner wissenschaftlichen Hochschule im Geltungsbereich des deutschen Grundgesetzes bereits früher um den Doktorgrad beworben habe.

Halle (Saale), 09 March 2016

Alexander Senichev

ALEXANDER SENICHEV

Weinberg 1 · 06120 Halle (Saale) · Germany
+49-345-5582-691 · senichev@mpi-halle.mpg.de

PERSONAL INFORMATION

Date of Birth 04 January 1986
Place of Birth Kirovsk, Murmansk region, Russia
Citizenship Russian
Marital Status Married since 2013

EDUCATION

Max Planck Institute of Microstructure Physics, Halle, Germany 04/2015 – Present
Department: Nano-systems from Ions, Spins and Electrons (NISE)
Research Associate

Max Planck Institute of Microstructure Physics, Halle, Germany 03/2011 – 03/2015
International Max Planck Research School (IMPRS)
for Science and Technology of Nanostructures
PhD Research Student
Thesis: *Near-field Spectral Imaging of Crystal-phase Heterostructures in GaAs Nanowires*
Supervisors: Dr. Peter Werner and Jun.-Prof. Dr. Jörg Schilling

Saint-Petersburg State University, St. Petersburg, Russia 09/2007 – 06/2009
Department of Solid State Physics
Master of applied mathematics and physics
Supervisor: Prof. Dr. Boris V. Novikov

Technical University of Munich, Germany 04/2008 – 07/2008
Department of Physics
Walter Schottky Institute
DAAD Scholarship Student, TUMexchange

Saint-Petersburg State University, St. Petersburg, Russia 09/2003 – 06/2007
Department of Solid State Physics
Bachelor of physics
Supervisor: Prof. Dr. Boris V. Novikov

Kirovsk High School №5 09/1993 – 06/2003
Graduated with honors: Silver Medal

RESEARCH EXPERIENCE

Saint-Petersburg State University, St. Petersburg, Russia 06/2009 – 02/2011
Department of Solid State Physics
Engineer, Research Assistant

Max Born Institute for Nonlinear Optics and Short Pulse Spectroscopy, Berlin, Germany 10/2008 – 04/2010
Division C: Nonlinear Processes in Condensed Matter
Visiting Researcher. Mentor: Dr. Jens W. Tomm

SCHOLARSHIPS

- Scholarship of the International Max Planck Research School for Science and Technology of Nanostructures** 03/2011 – 03/2014
Max Planck Institute of Microstructure Physics
Halle, Germany
- German Academic Exchange Service (DAAD) Scholarship** 04/2008 – 07/2008
Summer semester scholarship at Technical University of Munich, Germany
Exchange program with partner St. Petersburg State University, Russia

ACADEMIC AWARDS

- Best Poster Award** May 2013
Correlated Optical and Structural Analysis of Individual p-GaAs-AlGaAs Core-Shell Nanowires
European Material Research Society Spring Meeting
Strasbourg, France
- Best Poster Award** August 2013
Correlated Optical and Structural Analysis of Individual p-GaAs-AlGaAs Core-Shell Nanowires
Workshop “Light at the Nanotip: Scanning Near-field Optical Microscopy and Spectroscopy”
538. WE-Heraeus-Seminar, Bad Honnef, Germany

TEACHING EXPERIENCE

- Martin Luther University Halle-Wittenberg, Halle, Germany** Winter semester 2015/16
Faculty of Natural Sciences II — Chemistry, Physics and Mathematics
Teaching assistant
Course: *Structure of Matter (Struktur der Materie)* by Jun.-Prof. Dr. Jörg Schilling
Assisted in the course. Prepared and co-taught seminars. Evaluated student’s assignments.

PROFESSIONAL MEMBERSHIPS

- German Physical Society (DPG) Since 2012
Material Research Society Since 2012

Halle (Saale), 09 March 2016

Alexander Senichev